

**Electrically Conductive Polymer Nanocomposite Platforms for Routing: Modeling,
Fabrication and Verification**

Saber Haghgooye Shafagh

A Thesis

In the Department of
Mechanical, Industrial and Aerospace Engineering

Presented in Partial Fulfillment of the Requirements
For the Degree of
Master of Science (Mechanical Engineering)

at Concordia University
Montréal, Québec, Canada

March 2023

© Saber Haghgooye Shafagh, 2023

CONCORDIA UNIVERSITY
School of Graduate Studies

This is to certify that the thesis prepared

By: **Saber Haghgooye Shafagh**

Entitled: **Electrically Conductive Polymer Nanocomposite Platforms for Routing:
Modeling, Fabrication and Verification**

and submitted in partial fulfillment of the requirements for the degree of

Master of Science (Mechanical Engineering)

complies with the regulations of the University and meets the accepted standards with respect to originality and quality.

Signed by the final examining committee:

Dr. Sivakumar Narayanswamy	Chair
Dr. Behrooz Yousefzadeh	External Examiner
Dr. Sivakumar Narayanswamy	Examiner
Dr. Muthukumaran Packirisamy	Supervisor

Approved by

Martin D. Pugh, Chair
Department of Mechanical and Industrial Engineering

March 23, 2023

Mourad Debbabi, Dean
Faculty of Engineering and Computer Science

Abstract for Masters

Electrically Conductive Polymer Nanocomposite Platforms for Routing: Modeling, Fabrication, and Verification

Saber Haghgooye Shafagh

Creating an electrically conductive composite that can be used in a wide variety of circumstances is getting much attention. Making a flexible, easy to manufacture, and cost-effective electrical route is the challenge the research. Electrically conductive polymer composites have a wide range of applications in electronics and nanotechnology industries. They have unique features that allow them to be employed as smart materials in applications such as sensors, wearable devices, optoelectronics, and printed electronics. Thermal and electrical characterization was performed for two polymer nanocomposites to investigate their properties. Several fillers can be added to the host polymer to make a conductive nanocomposite. The filler used in this study is multi-wall carbon nanotube (MWCNT) which also attracted attention in the literature. Moreover, silver nanoparticles were also used to compare the effect of multiple fillers on conductivity. Polydimethylsiloxane (PDMS) and poly(3,4-ethylene dioxythiophene): poly(4-styrene-sulfonate), (PEDOT:PSS) were the two different host polymers that have been used to see the effect of the base polymer on conductivity. PDMS is a non-conductive polymer but more flexible while on the other hand PEDOT:PSS is a highly conductive polymer but less flexible.

Results show that using conductive polymer (PEDOT:PSS) as the host could increase the conductivity up to 378.97 S/m. The nanocomposite investigated was found to have excellent flexibility and well adhesion to the PDMS substrate. Also, based on the experiments, these conductive lines are sensitive to temperature, which is an attractive feature.

Acknowledgment

I would like to express my deepest gratitude to my advisor Professor Muthukumaran Packirisamy for accepting me as a part of his Optical-Bio Microsystems group. Through his mentorship, I learned that there are always new things to explore and new ways to push the boundaries of research. His guidance, novel ideas, and support directed me through the greatest obstacles in my research and helped me to deepen my knowledge and be creative through this path.

I would like to thank Dr. Simona Badilescu and Dr. Mohsen Habibi. They always kindly guide me through this journey.

I would like to thank Shervin Foroughi, Mahdi Derayatifar, Imran Deen, and other members of the Optical-Bio Microsystems group, it was a great pleasure to spend three years of my life besides you.

In the end, I would like to thank my lovely parent and my beloved brother for their unconditional support, patience, and advice throughout my study.

To my beloved parents and my lovely brother.

Table of Contents

List of Figures	x
List of Tables	xii
List of Symbols and Abbreviations	xiii
Chapter 1. General Introduction	1
1.1. Introduction to Nanotechnology	1
1.2. Technological Revolutions	1
1.3. The Nanotechnology Revolution	3
1.4. Applications of Nanotechnology	5
1.5. Innovation in Carbon-Based Nanotechnology.....	7
1.6. Future of Nanotechnology	8
1.7. Background Research	9
1.7.1. <i>Fabrication of Nanomaterials</i>	9
1.7.2. <i>CNT/PDMS Applications</i>	13
Chapter 2. PDMS/CNT Composites	16
2.1. Polydimethylsiloxane.....	16
2.2. Carbon Nanotubes.....	19
2.3. Methodology.....	22
2.3.1. <i>Materials</i>	22
2.3.2. <i>PDMS/MWCNT fabrication</i>	22

2.3.3.	<i>Electrical Measurements</i>	26
2.3.4.	<i>Thermal Measurements</i>	26
2.4.	Results and discussion	28
2.4.1.	<i>Electrical Properties of MWCNT/PDMS composites</i>	28
2.4.2.	<i>Thermal Characterization (Joule heating study)</i>	32
2.5.	Conclusion and Future Research	33
Chapter 3. Integration of Silver Nanoparticles into MWCNT/PDMS Composites for Improved Electrical Properties		35
3.1.	Introduction.....	35
3.2.	Methodology	37
3.2.1.	<i>Materials</i>	37
3.2.2.	<i>Fabrication</i>	37
3.3.	Results.....	38
3.3.1.	<i>Scanning Electron Microscopy</i>	41
3.3.2.	<i>Thermal Characterization (Joule heating study)</i>	43
3.4.	Conclusion and Future Research	44
Chapter 4. Development and Electrical Characterization of PEDOT:PSS		46
4.1.	PEDOT:PSS.....	46
4.1.	Methodology	51
4.1.1.	<i>Materials</i>	51
4.1.2.	<i>Mold Patterns</i>	51

4.1.3. <i>Fabrication of PEDOT:PSS/MWCNT Composites</i>	52
4.1.4. <i>Thermocouple calibration</i>	53
4.1.5. <i>Temperature tests</i>	55
4.2. Results and Discussion	56
4.2.1. <i>Morphological Characterization</i>	57
4.2.2. <i>Impedance Analysis</i>	59
4.3.3. <i>Temperature Profiles</i>	60
4.3.4. <i>Simulation of Temperature Profiles of Composite filament</i>	64
4.3. Conclusion and Future Research	67
Chapter 5. Routing for Energy Harvester	69
5.1. Introduction.....	69
5.2. Methodology	71
5.2.1. <i>Materials</i>	71
5.2.2. <i>PDMS molds</i>	71
5.2.3. <i>CNT-PEDOT:PSS Composites</i>	71
5.3. Experimental set-up	72
5.4. Electrical measurements	76
5.4.1. <i>Cascading Efficiency</i>	76
5.5. Results and Discussion	79
5.6. Conclusion and Future Research	86
Chapter 6. Conclusion and Future work	88

References 90

List of Figures

Figure 1.1: S-shape trajectory of technology revolution [4].....	3
Figure 1.2: Increasing Nanotechnology demand over 20 years [5].....	5
Figure 1.3: Nanoparticle applications in different scientific and engineering fields [9].	6
Figure 1.4: Technology breakdown of nanotechnology patent literature [5].	7
Figure 1.5: Structure of different carbon structures [9].	8
Figure 2.1: Chemical structure of PDMS [33].	17
Figure 2.2: Structure of Graphene sheet, SWCNT and MWCNT [40].	20
Figure 2.3: Schematics od CNT/PDMS composite fabrication. (a-c) dispersion of aggregated [12].	24
Figure 2.4: Mixture preparation following with pouring method.....	25
Figure 2.5: Step-by-step fabrication process	25
Figure 2.6: Setup configuration for temperature test.	27
Figure 2.7: Schematic of setup configuration for temperature test.....	27
Figure 2.8: Resistance variation by MWCNTs percentage (CNT30 and CNT15) (error bar indicates range, n=10).	29
Figure 2.9: SUEM image of a cross-section of a micro conductive line.	30
Figure 2.10: Conductivity of the CNT30 and CNT15 in different wt.% (error bar indicates range, n=10).	31
Figure 2.11: Temperature variation by time by applying voltage for PDMS + MWCNTs 30 wt.% and PDMS + MWCNTs 50 wt.%.....	33
Figure 3.1: Resistance variation in different MWCNT/AgNP ratios, mixed with ultra-sonication and shear force (error bar indicates range, n=3).	39
Figure 3.2: Conductivity variation in different MWCNT/AgNP ratios, mixed with ultra-sonication and shear mixing (error bar indicates range, n=3).	40
Figure 3.3: SEM image of C45S05. (Area A refers to zone of large AgNP, Area B refers to small AgNP, and Area C refers to PDMS mold.).....	41
Figure 3.4: Chemical analysis of PDMS, MWCNT and AgNP	42
Figure 3.5: Temperature variation by time by applying voltage for C45S05 and C35S15.	44
Figure 4.1: Chemical structure of PEDOT:PSS [59].	47
Figure 4.2: (a) Chemical structure of PEDOT:PSS, (b) Schematic structure of PEDOT:PSS, and (c) Schematic representation of MWCNT polymer composite [62].....	48
Figure 4.3: dimensions of the A) straight B) serpentine and C) zigzag channel (mm)	52
Figure 4.4: Schematic setup for the thermocouple calibration.	54

Figure 4.5: Comparison between Thermocouple and Thermometer (n=3)	54
Figure 4.6: A) Schematic set-up for measuring resistance in different temperature on hot plate and B) Serpentine channel with sensor tip implanted.....	55
Figure 4.7: A) Schematic set-up for electro thermal test with DC power applied to line and B) Serpentine channel with sensor tip implanted.....	56
Figure 4.8: SEM image of the PEDOT:PSS and MWCNT composite.....	58
Figure 4.9: SEM image of the PEDOT:PSS and MWCNT composite along with the diameter of the MWCNTs.....	59
Figure 4.10: Top view of A) straight, B) serpentine and C) zigzag channels filled with PEDOT:PSS and MWCNT, with copper foils as electrodes.....	61
Figure 4.11: Change in resistance versus temperature of the straight, serpentine, and zigzag channels (error bar indicates range, n=3).....	62
Figure 4.12: Temperature variation over time for straight, serpentine, and zigzag channels (n = 3)	63
Figure 4.13: Schematic of the modeling in COMSOL Multiphysics.	64
Figure 4.14: Experimental Vs Simulation of temperature change by applying voltage.	67
Figure 5.1: Lead-Zirconium-Titanate piezoelectric transducer	72
Figure 5.2: Equivalent circuit of energy harvesting set up from piezoelectric transducer	73
Figure 5.3: Schematic set-up for measuring force and voltage.	74
Figure 5.4: Schematic set-up for measuring current and voltage.	74
Figure 5.5: Diagram of a piezoelectric actuator in cantilever beam set-up. Actuator is A) at rest and B) in motion and producing an AC voltage	75
Figure 5.6: Waveform of voltage from A) a piezoelectric actuator and B) a full-bridge rectifier and smoothing action of a reservoir capacitor	75
Figure 5.7: Schematic circuit showing where power between components was measured.....	77
Figure 5.8: Measured electrical parameters between components.	77
Figure 5.9: Peak to peak voltage of piezoelectric transducer, from 60 to 190 Hz.....	79
Figure 5.10: Peak to peak voltage produced from piezoelectric actuator during “flick test”	80
Figure 5.11: Maximum voltage after smoothing recorded from piezoelectric transducer and from PEDOT:PSS components.....	81
Figure 5.12: A)Force and B)voltage before and after adding weight of 1.15, 2.40 and 3.05 g... 82	82
Figure 5.13: Voltage before and after adding a 1.15 g load, recorded from the piezoelectric transducer and from PEDOT:PSS components.	83
Figure 5.14: Real-time A) voltage and B) current recorded from the battery during charging from the piezoelectric transducer and from PEDOT:PSS components	86

List of Tables

Table 1.1: Distribution of Nanotechnology inventions by region	5
Table 2.1: Measured resistance for PDMS/MWCNT composite with varying wt.% of cnt30 and CNT15	29
Table 2.2: Electrical properties of PDMS/MWCNT composites with CNT30 and CNT15.	31
Table 3.1: Composition of different samples with varying MWCNT and silver content.....	37
Table 3.2: Measured resistance for PDMS/MWCNT/AgNP composites, blended with ultrasonication and shear mixing(n=3).....	40
Table 3.3: Electrical properties for MWCNT/AgNP, blended with ultrasonication and shear mixing (n=3).....	41
Table 3.4: Analytical data of the PDMS, MWCNT and AgNP.	42
Table 4.1: Electrical properties of PEDOT:PSS in addition to MWCNT, Glycerol, and PEG (n = 10)	57
Table 4.2: Electrical properties of PEDOT:PSS/MWCNT mixture in different lengths (n = 3)..	60
Table 4.3: Electrical properties of PEDOT:PSS/MWCNT mixture in different widths (n = 3)...	60
Table 5.1: Maximum recorded force and voltage after weight added to piezoelectric actuator...	82
Table 5.2: Measure RMS voltage and current after components, without any PEDOT:PSS component.....	84
Table 5.3: Measure RMS voltage and current after components, with zigzag PEDOT:PSS component included.	84
Table 5.4: Measure RMS voltage and current after components, with serpentine PEDOT:PSS component included.	85
Table 5.5: Cascading efficiency between components	85

List of Symbols and Abbreviations

Abbreviations

AgNW	silver nanowire
CNT	Carbon Nanotube
DMSO	Dimethyl sulfoxide
DMF	N, N-dimethyl formamide
DMF	N, N-dimethylformamide
EG	ethylene glycol
GO	graphene oxide
LED	light-emitting diode
MWCNT	Multi-Wall Carbon Nanotube
PDMS	Polydimethylsiloxane
PUA	polyurethane acrylate
PEG	polyethylene glycol
PEDT : PSS	poly(3,4-ethylene dioxythiophene):poly(4-styrene-sulfonate)
SWCNT	single-wall carbon nanotube
THF	Tetrahydrofuran
TCE	transparent conductive electrode
UV	Ultraviolet
UPS	Photoelectron Spectroscopy
XPS	X-ray Photoelectron Spectroscopy

Symbols

σ	Conductivity (S/m)
ρ	Resistivity (Ω .m)
η	Efficiency

Chapter 1. General Introduction

1.1. Introduction to Nanotechnology

Nanotechnology is the study and control of materials at a length scale of below 100 nm, and it is considered to have a significant effect on human life [1]. For comparison, human hair is about 100,000 nm thick. At the nanoscale, the major characteristics of materials vary drastically [2]. In 1959 Feynman, R.P et al. [3] launched the birth of nanotechnology when he talked about the problem of manipulating and controlling things on a small scale. As he said, the behavior of atoms on a small cell will be different than large scale, in order to satisfy the laws of quantum mechanics. So different laws, atoms' behavior, and manufacturing strategy will be expected down there [3].

Nanomaterials have two major features: enhanced relative surface area and quantum effects. By these two elements, other attributes of material such as reactivity, mechanical strength, and magnetic, and electrical properties can easily alter or improve [1]. When the particle size is decreased, more atoms are detected on the surface than those inside the particle. For instance, when a particle size is 30 nm, 5% of its atoms are on its surface, while a 10 nm particle has 20 % of total atoms on the surface and this number for a 3 nm particle is 50% [1]. As a result, compared to bigger nano or micron-sized particles, smaller nanoparticles have a higher surface area per unit mass. Therefore, a given amount of material in the nano domain will be significantly more reactive than a similar mass of material composed of bigger particles.

1.2. Technological Revolutions

From gestation through exploration, technology revolutions often follow an S-shaped trajectory distinguished by core innovations (Figure 1.1) [4]. As the next technological revolution reaches

the exploration phase, the exploration phase progresses to evolution and eventually, maturity as the technology's innovation potential is discovered and acknowledged [5]. The modern history of technologies may be split into numerous phases of the technical revolution that occurred in various parts of the world and, curiously, corresponding to the regions of global dominance at the time [5]. The steam engine, the textile industry, and mechanical engineering were all born in the United Kingdom between 1780 and 1840, but between around 1840 and 1900, England, Germany, and the United States began to develop railways, electricity, and their steel industry. The third technological revolution, which lasted roughly from 1900 to 1950 and was mostly centered in the United States, delivered electrical engines, heavy chemicals, vehicles, and mass manufacture of consumer durables. Eventually, the Pacific Region, , and the United States (particularly the state of California) have been the heart of the fourth technology revolution, which has involved synthetics, organic compounds, and computers, from around 1950 to the present day [6].

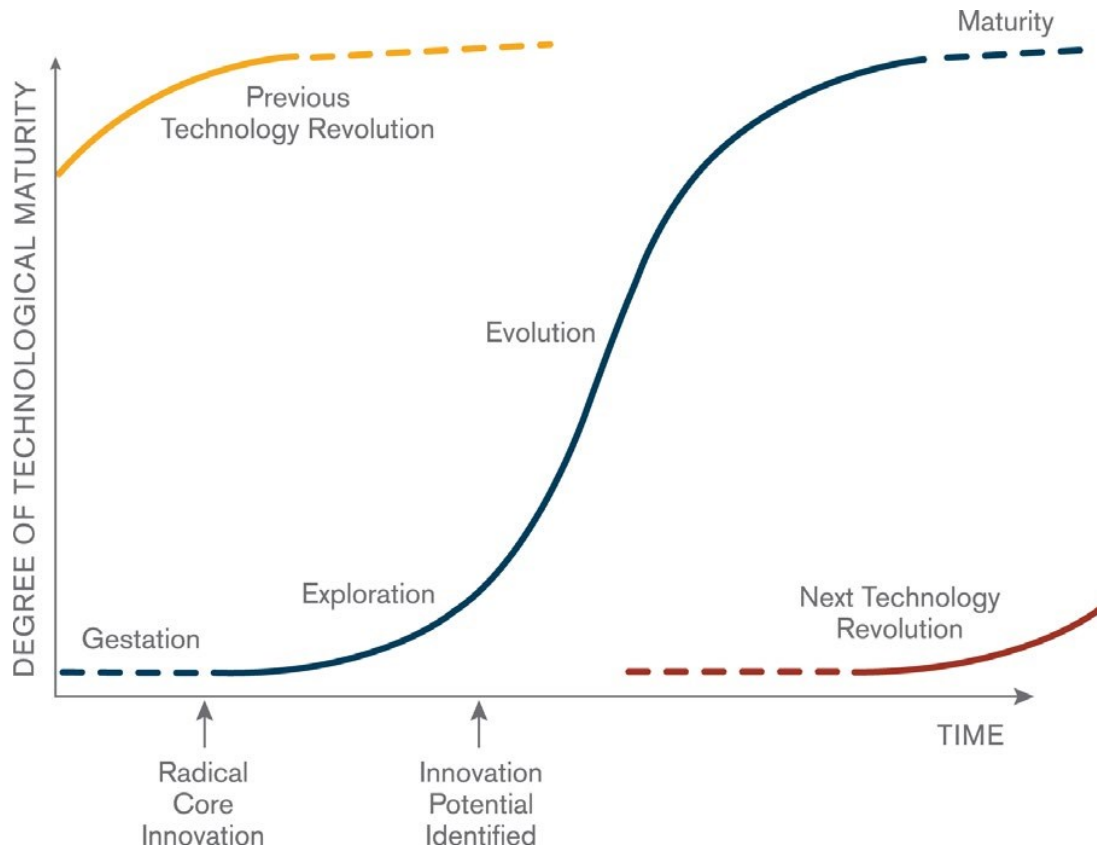


Figure 1.1: S-shape trajectory of technology revolution [4].

1.3. The Nanotechnology Revolution

Nanotechnology, like computers, is both an enabling technology (an invention or innovation that can be applied to drive radical change in the capabilities of a user or culture) and a technological field in its own right [5]. Nanotechnology is being used in practically every economic area for research and development, from aviation to medicine to energy. Moreover, nanomaterials and nanotechnology concepts are used in numerous commercial goods. Introducing silver nanoparticles into wound dressings, for instance, gives the dressing antimicrobial properties [5]. Nanomaterials have already advanced several products of engineering due to new qualities connected with them, such as self-cleaning windows, high-efficiency solar cells, energy-efficient light-emitting diodes (LED), clean tech, and super-hydrophobic nanomaterials resistant to ice formation [1]. Nanoparticles also can be used by sports equipment and automotive manufacturers

to reduce the weight and boost the durability of their goods. Nanoparticles are frequently used in paints to improve color, decrease or remove volatile chemical compounds, and prevent bacterial or fungal development, which is very valuable in hospitals and clinical settings [5]. There is significant effort being directed into the ability to manipulate nanoscale structures using novel synthetic techniques such as chemical vapor deposition (CVD) [7] and to study the properties of nanocomposite material.

To understand nanomaterials, two factors must be evaluated, their base attributes and their morphology and interfacial features, which come from mixing properties from the parent constituents into a single material, leading to the possibility of new properties not found in the parent constituent materials [8].

The “growth spurt” of nanotechnology began at the beginning of the 21st century. Nanotechnology patents have grown at an exponential rate shortly after 2000 (Figure 1.2) [5]. North America is by far the pioneer in nanotechnology, with around 54% of the nanotechnology research has taken place in the United States. East Asia is the next biggest contributor to nanotechnology research, accounting for around 28% of the total, followed by European nations, which account for around 20% of all assignees (Table 1.1) [5].

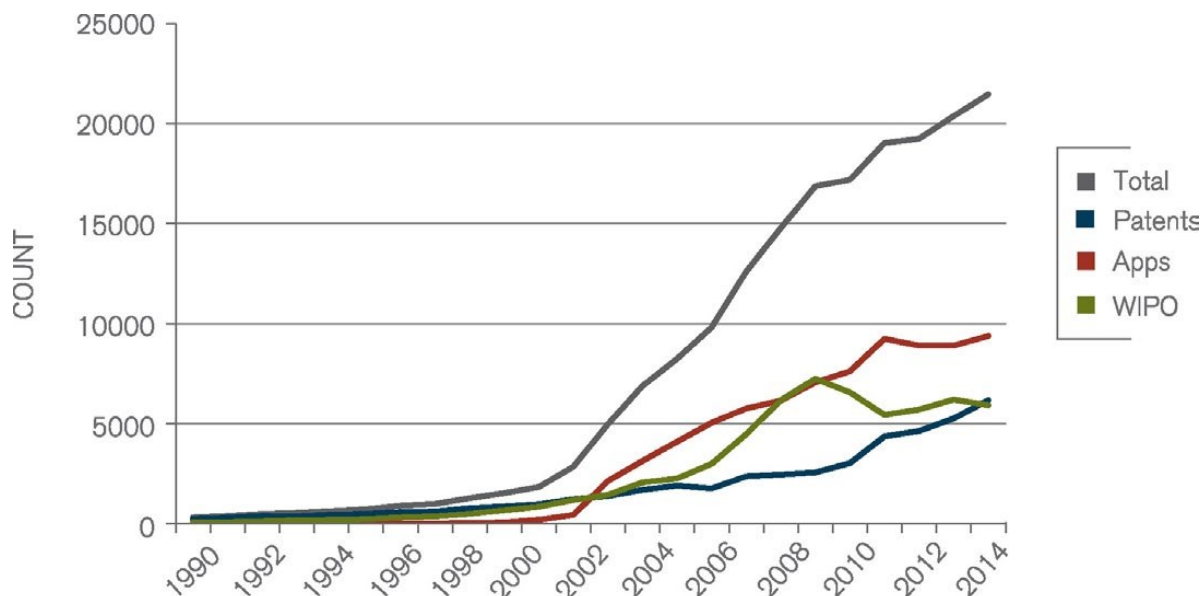


Figure 1.2: Increasing Nanotechnology demand over 20 years [5].

Table 1.1: Distribution of Nanotechnology inventions by region

North America	56.5%	Europe	19.5%
United States	54.2%	Germany	5.8%
Canada	2.3%	France	4.0%
East Asia	27.8%	United Kingdom	2.8%
South Korea	8.3%	Netherlands	1.7%
Japan	8.0%	Switzerland	1.5%
China	5.3%	Italy	1.1%
Taiwan	5.1%	Belgium	0.9%
Singapore	1.1%	Sweden	0.9%
		Spain	0.8%

1.4. Applications of Nanotechnology

One of the most attractive areas of nanoscience is the development of nanoparticle (NP) doped functional polymers to be used in the space and the aviation industry as well as smart textiles, wearable electronics-health monitoring systems, sensors, microfluidics and micro-

all types and classes of nanocomposite materials result in new and better properties when compared to their macro composite counterparts [1].

Nanocomposites hold the promise of new applications in a variety of domains, including nonlinear optics, nanowires, sensors, mechanically reinforced lightweight components, battery cathodes, ionics, and other systems. Each of these applications has shown considerable expansion during the early 2000s, comparable to the overall trends in nanotechnology research. In particular, nanoscale semiconductors used in transistors have seen significant development. As computers keep reducing in size and switch from traditional top-down technologies to nanotechnological bottom-up technologies, the computer and electronics industry has placed more and more importance on nanomaterials research (Figure 1.4) [5].

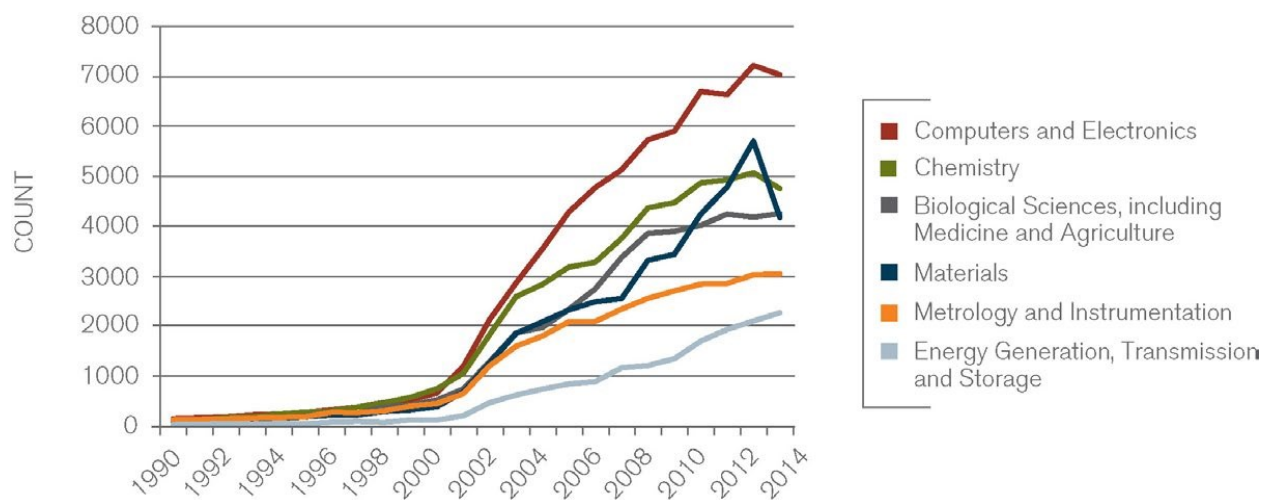


Figure 1.4: Technology breakdown of nanotechnology patent literature [5].

1.5. Innovation in Carbon-Based Nanotechnology

Since the discovery of fullerenes in 1985 and carbon nanotubes in 1991, carbon-based nanoparticles have attracted the attention of the nanotechnology industry [5]. The discovery of graphene in 2004 sparked interest in graphitic carbon-based nanotechnology. This is a distinct type

of nanomaterial in that it contains fullerene, nanotube, and graphene, or 0-dimensional, 1-dimensional, and 2-dimensional structures (Figure 1.5), that have no mass equivalent. These unique structures led to various electrical, thermal, and mechanical characteristics, enabling applications in a wide range of fields. Carbon nanotubes and graphene, for instance, are being developed in the Computers and Electronics industry for flexible displays and small transistors. Lithium-ion batteries are a hot issue in the energy market since graphene applied to the electrodes has been demonstrated to boost lithium storage capacity [5].

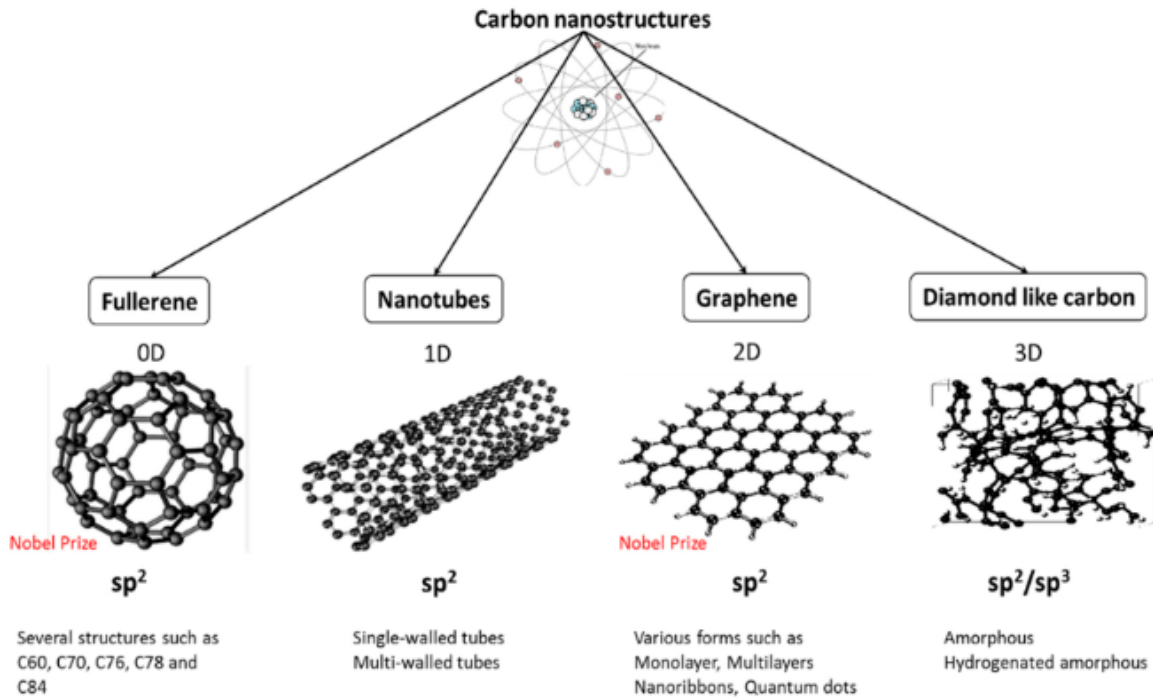


Figure 1.5: Structure of different carbon structures [9].

1.6. Future of Nanotechnology

Since the nanotechnology movement progresses, patterns in intellectual property are beginning to emerge that may indicate industrialization. The United States and Eastern Asia are emerging as innovation leaders, which might suggest where the largest economic consequences would occur.

Moreover, technology fields where intellectual property protection is slowing i.e. Computers and Electronics, Chemistry, and the Photovoltaics section of Energy may imply that sections of the current technologies are shifting from the research phase to manufacture and marketing. As a result, significant nanotechnology applications and products might emerge in these industries. On the other hand, industries like energy, particularly energy storage, where the pace of patenting is still high, might see further commercialization in the future.

However, It is not a novel idea to create silicone-based elastomers that are electrically or magnetic conductive, and both in nature [10, 11]. Nevertheless, the fabrication and stability of the final sample are always an issue, which is the major focus of this thesis. This thesis significantly contributes to the development, characterization, and fabrication process of flexible conductive polymer materials.

1.7. Background Research

1.7.1. Fabrication of Nanomaterials

A wide variety of methods have been used to fabricate conductive polymers. Kim et al. [12] developed a simple method of mixing Carbon Nanotubes (CNT) and (Polydimethylsiloxane) PDMS in association with isopropyl alcohol (IPA) and methyl-terminated PDMS. Ultrasonication was used to obtain a uniform dispersion of CNTs inside the PDMS. They achieved high conductivity with sheet resistances $<20 \Omega/\text{sq}$, high flexibility (more than 90°) and elasticity (more than 45% yield strain), the excellent tensile stress of $\sim 3.65 \text{ MPa}$, good strain sensitivity and stability (gauge factor reaching 10,000 cycles). The fabrication method that they provided was low cost, simple, and rapid and also has many advantages in the fields such as wearable electrical stimulation and detection devices, and biomedical applications.

Ozhikandathil et al. [13], propose a novel method of synthesizing the electrically conducting nanocomposite using an in situ reduction of gold ions combined with simple mechanical stimulation of silver nanoparticles and Multiwall Carbon Nanotubes (MWCNTs). The method is simple and does not require any strong mixing apparatus such as the ultrasonic bath or shear mixer, and can be carried out in a general laboratory environment. The in situ reduction of gold ions from gold chloride aqueous solution by the curing agent in the PDMS hence forms the gold decorated and homogeneously dispersed PDMS matrix by simple hand mixing. The process resulted in an electrically conducting nanocomposite with lower electrical resistivity up to $3.5 \times 10^{-3} \Omega \cdot m$. Apart from the simplicity, a major benefit of the proposed method of synthesis is that the higher electrical conductivity can be achieved with a smaller amount of conducting filler, producing an ultra-flexible and electrically conducting PDMS nanocomposite. Moreover, the nanocomposite can be micro-patterned to manufacture flexible sheets with electrical signal routing lines.

Cavas et al. [14], tried to incorporate carbon nanoparticles like MWCNTs (pristine and carboxyl-functionalized) and graphene oxide (GO) to enhance the mechanical properties of PDMS coatings for marine applications. While optimal dispersion of nanofillers into polymer matrices is difficult, one of the primary goals of this research was to investigate the PDMS mechanical reinforcement by creating alternative dispersing ways of pristine MWCNTs into the PDMS matrix. To have a better dispersion of nanoparticles in the PDMS matrix, xylene was used as a solvent. Based on the findings, the mechanical properties of nanocomposites have been influenced by the presence of MWCNTs and the form of carbon nanoparticles. By adding 0.50 wt.% MWCNT-filled PDMS, the highest tensile strength (0.59 ± 0.07 MPa), and elongation values ($116.67 \pm 11.91\%$) were obtained, although there was a steady reduction as the MWCNTs content increased.

Misra et al. [15] created thin, multilayer materials with vertically aligned carbon nanotube (CNT) arrays and poly dimethyl siloxane (PDMS) polymer layers to characterize their mechanical performance under compression. It is possible to create multilayer structures with low density ($0.12\text{-}0.28\text{ g/cm}^3$) by using CNT arrays that were synthesized with graded mechanical properties along their thickness. The resulting materials have a fibrous, hierarchical structure and distinct mechanical characteristics [15]. Also, Zhang et al. [16] introduced a transparent stretchable conductor with well-aligned CNT ribbons integrated into a CNT/PDMS film made of PDMS. The CNT/PDMS film is capable of retaining stable conductivity under repeated stretching to strains of up to 100% because of the good inter-tube contact and stable CNT arrangement in the CNT ribbons [16].

In other work, Ozhikandathil et al. [17] also introduced a novel procedure of synthesizing the Au-MWCNT hybrid composite and deposition of a glass substrate by drop casting to a coffee ring pattern is explored to make MWCNT bundles become locally sensitive for LSPR (Localized surface plasmon) properties which shows advantageous of MWCNT for LSPR sensing such as chemical and bio species. Herren et al. [18] examined the impact of microwave irradiation on the electrical conductivity of PDMS nanocomposites with distributed MWCNTs. The characteristics of microwave-cured nanocomposites were compared to those produced using a regular oven by the thermal technique. Due to better nanoparticle dispersion and likely CNT alignment, the microwave-curing approach significantly increased the electrical conductivity of the nanocomposites. Nanocomposites with 1 wt.% CNTs treated with one-step microwave irradiation had a conductivity increase of 142.8% over thermally cured nanocomposites.

Wu et al. [19] present the fabrication and evaluation of a flexible temperature sensor based on a composite of flake graphite, carbon nanotubes, and polydimethylsiloxane. High-temperature

sensitivity and good linearity are displayed by the sensor. The screen printing procedure is used to create the FG (Flake Graphite)/CNT/PDMS temperature-sensitive films. The rheology of the FG/CNT/PDMS inks demonstrates their superior printability. Niu et al. [20] show a technique for fabricating conducting composites based on PDMS that can be used to pattern conductive structures. These composites are created by combining conductive nano- to micrometer-sized particles with a PDMS gel. According to the results of the experiments, it is possible to build and incorporate 2D and 3D conducting microstructures into the PDMS base material. These composite microstructures exhibit excellent conductivity as well as good mechanical and thermal characteristics. The benefit of using PDMS-based conducting composites is the simplicity with which these microstructures can be bonded to and embedded in PDMS-based microchips, greatly enhancing the functionalities that can be achieved.

In a study by Sepúlveda et al. [21], the underlying aligned-CNT morphology is how the elastic response of vertically aligned CNT/PDMS nanocomposites behaves. A flexible PDMS substrate is embedded with multiwalled carbon nanotubes (MWCNTs) at 1 vol.% to produce a flexible polymer nanocomposite (PNC). The findings imply that even after wetting and curing PDMS, the CNTs maintain their alignment. Wu et al. [22] looked into the mechanical characteristics of PDMS and a combination of PDMS and carbon nanotubes both statically and dynamically. To avoid agglomeration, an ultrasonic device was used to stir the PDMS/CNT nanocomposites. The thermoforming technique was used to create the test specimens of nanocomposites at 150°C for 15 min. The elastic modulus monitoring outcomes from a nanoindentation test follow a similar pattern to the outcomes from the tensile test method.

1.7.2. CNT/PDMS Applications

Wang et al [23], introduced a layer-by-layer fabrication of MWCNTs and nickel ferrite (NiFe_2O_4) nanoparticles, followed by a PDMS cover, which was used to create a flexible and robust EMI shielding cotton fabric. The cotton fabric was effectively produced with efficient electrical, magnetic, and thermal conductive pathways thanks to the strong interfacial contacts between MWCNTs and NiFe_2O_4 . The polymer blend fabrics have excellent electrical-magnetic characteristics, exceptional EMI shielding effectiveness, and significantly improved thermal conductivity.

Hong et al. [24] have devised and manufactured electrical routing and integrated packaging using bio-compatible flexible substrates. The achieved packaging technology may incorporate electrical circuits, stationary components, and moving components on flexible substrates. They employed polyimide as the electrical circuit's substrate material, and PDMS is used as the outer covering to seal the entire device. When flexibility is required, this adaptable package can be applied to communication or sensing goods. It will be beneficial in wearable health monitors as well as flexible electronic equipment.

Raju et al. [25] have introduced a new approach to sensing and detecting exosomes in body fluids and cell cultures. This is an optical technique, based on the LSPR of silver nanoparticles. They use a synthetic peptide to provide a straightforward label-free strategy for capturing and detecting cell-derived vesicles (EVs) based on the sensitivity of the silver plasmon band to the surroundings of the silver nanocomposite. An LSPR detection approach was employed to quantify EVs. The initial findings suggested that a label-free method based on the reactivity of the Ag-LSPR band to the local environment could be useful for detecting exosomes. Bali et al. [26] fabricated a temperature-sensing flexible Wheatstone bridge that was fully inkjet printed. The materials for the positive and

negative thermal coefficients are a mixture of poly(3,4-ethylene dioxythiophene): poly(4-styrene-sulfonate) (PEDOT:PSS) and dimethyl sulfoxide (DMSO) and a carbon nanoparticle ink. Printing the solitary substances onto PEN substrates is followed by encapsulation. The Wheatstone bridge sensors demonstrate a sensitivity of 4 mV/°C at a bias current of 1 mA and exhibit good linearity and little hysteresis over a temperature range of 20°C to 70°C.

In other work, by using the ninhydrin–PDMS composite, they introduced a novel method to identify ammonia. By incorporating ninhydrin into the PDMS polymer matrix, a composite polymer film is created. In addition, an optical lab-on-a-chip device for ammonia detection is designed by introducing the ninhydrin-polymer composite into a microfluidic device. Varying optical absorption characteristic is a result of the chemisorption of ammonia onto the composite [27]. Tsao et al. [28] demonstrated a brand-new technique for creating temperature sensor arrays by electro-resistively dispensing polymer onto stretchable polyimide films. The sensor array can be used as an artificial human skin for robots' sensory systems. The electro-resistive composites used PDMS as their matrix, and various conductive fillers, including carbon black, graphite powder, and carbon nano-fibrils, have been studied. The shapes and sizes of various heat sources are in good agreement with the detected temperature contours.

Ramalingame et al, [29] developed a Versatile tactile pressure sensor array based on multiwall carbon nanotubes (MWCNT) and PDMS in the field of robotics. A nanocomposite-based pressure sensor was introduced which has high sensitivity with minimum load range. Moreover, a 4×3 tactile sensor array design, which might be put into robot fingers, is presented. The pressure sensor's great sensitivity provides accurate grabbing, with the capacity to detect minuscule items as small as 5 mm and weighing 1 g. Lai et al. [30] demonstrated a brand-new resistive sensing array that can both store and removes tactile images. MWCNTs and silver nanoparticles were

dispersed through PDMS polymer with the aid of the dielectrophoresis (DEP) procedure to create the sensing material. Conductive CNT networks within the polymer are broken when the sensing element is pressed, raising the element's resistivity. After the external force is removed, the polymer still exhibits resistivity, and by reforming the conductive CNT networks with DEP, resistivity can be restored to its initial value. This study explores the characteristics of devices with various electrode gaps and shows the effectiveness and reliability of the suggested sensing elements.

As mentioned earlier this thesis significantly contributes to the development, characterization, and fabrication process of flexible conductive polymer materials. To the best of our knowledge, combining Nano-fillers with the base polymer in low wt.% has been investigated a lot in the literature and is mostly limited to one kind of filler. This research will go beyond the amount that literature reported mostly for CNT and PDMS, and also use the second filler to see the difference. Comparison of different mixing methods is also the other purpose of the research. The literature mostly used PDSM as the base polymer, which is a none conductive polymer, here also a conductive polymer will be replaced for PDSM to see the effect of the base polymer on the conductivity.

Chapter 2. PDMS/CNT Composites

PDMS/CNT composite is a type of composite material that is made up of a polymer matrix, polydimethylsiloxane (PDMS), and carbon nanotubes (CNTs) that are embedded within the matrix. PDMS is a widely used silicone-based polymer that is known for its excellent elasticity, biocompatibility, and optical transparency. CNTs, on the other hand, are cylindrical structures made up of carbon atoms that have a high aspect ratio and excellent mechanical, thermal, and electrical properties. The combination of these two materials leads to the formation of a composite material that exhibits unique properties such as high mechanical strength, electrical conductivity, and improved thermal stability. This has led to the widespread use of PDMS/CNT composites in various applications such as sensors, energy storage devices, and biomedical devices.

2.1. Polydimethylsiloxane

Polydimethylsiloxane which is a silicone-based elastomer has been widely used in the manufacture of microfluidic devices as a structural material [31]. Biocompatibility, optical transparency, mechanical and chemical stability, low electrical conductivity, low cost, and ease of micro patterning are only a few of the unique qualities of PDMS, which have made it appealing for the development of biological and chemical micro devices [32]. There are also two features that PDMS got benefits from them: it is a thermosetting polymer and also has uncommon rheological properties. The chemical formula for PDMS is $\text{CH}_3[\text{Si}(\text{CH}_3)_2\text{O}]_n\text{Si}(\text{CH}_3)_3$, where n is the number of repeating monomer units $[\text{SiO}(\text{CH}_3)_2]$. Figure 2.1 shows the chemical structure of the PDMS.

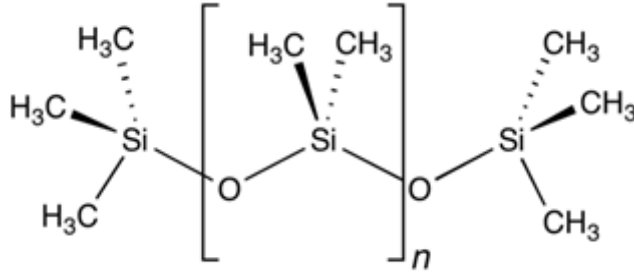


Figure 2.1: Chemical structure of PDMS [33].

Due to weak adhesion between PDMS and metals, integrating and patterning of conducting lines and magnetic particles on PDMS has been found complicated [1]. Finding a way to embed functionally electrically conductive and magnetic material in bulk PDMS is highly crucial for applications such as signal routing, EMI shielding, interfacing to signal processing electronics, and actuation purposes. When a metal/metal alloy integration, is flexed, bent, or twisted, micro-cracks will appear on the surface of the integrated conductive lines, leading to electrical discontinuity [34].

Electrical and thermal conductivity are two properties that conductive polymer nanocomposites can exhibit. Furthermore, heat dissipation applications for the management of excessive heat generated in integrated circuits have shown a lot of interest in polymer composites with high effective thermal conductivity. Electrically conductive polymer composites, on the other hand, have a wide range of applications in electronics and nanotechnology industries. They have unique features that allow them to be employed as smart materials in applications such as sensors, optoelectronics, and print electronics. Obtaining hybrid conductivities, on the other hand, is a difficult task to achieve in terms of balancing the composites' entire package of features. One or more fillers may be utilized, although preserving the mechanical qualities of the polymer matrix becomes increasingly challenging as the number of fillers grows [35].

As mentioned earlier, one of the features of PDMS is its low electrical conductivity. To modify the electrical properties of PDMS, conductive nanoparticles can be added to the polymer matrix [36]. These conductive polymers are attracting much attention recently in the applications such as MEMS, microelectronics, microsensors, microactuators, and microfluidic and lab-on-chip (LOC) [37]. And have the potential to be used in flexible systems. Therefore, developing a micro patternable nanocomposite polymer such as a conductive PDMS-based polymer is of great interest. Although micromachining and MEMS techniques have their roots in the silicon-based IC community and have been gaining popularity, there have been advancements in material and manufacturing methods. Polymer microfabrication techniques such as soft lithography, micro molding and microinjection molding have been created [38]. MEMS, in conjunction with microfluidics, can provide accurate control of fluids on micro and nanoscales, for instance, in drug delivery systems. To achieve such systems, all of the necessary components must be downsized and integrated into a fully functional system. To achieve complex operations such as the detection of disease markers or environmental toxins in small (e.g., nanoliter) specimens of fluid and tracking, these systems may include various facets for sample/drug storage, chemical reaction chambers, fluid control, analyte isolation and sensing, and measurement.

Several forms of filler have been utilized to incorporate into the polymer matrix from the initial discoveries in polymer composites. Particles can be categorized into two size ranges: micro and nanoparticles (NPs). Organic and inorganic NPs are two types of nanoparticles that have just lately been discovered and categorized based on their physical and chemical characteristics. The so-called "Nano-scale" effect is based on the fact that NPs have a large specific area due to their tiny size. When NPs are utilized as fillers in polymer matrixes, this effect can lead to improvements, and it increases the chance of constructing polymer nanocomposites with higher performance [35].

2.2. Carbon Nanotubes

Since the PDMS is an electrically non-conducting elastomer, integrating electrically conducting material such as Carbon Nanotubes (CNT), Graphene (G), Carbon Black (CB), gold (Au), and silver (Ag) will increase the conductivity of the composite. The other disadvantage of PDMS is its low mechanical performance. Among these fillers, CNTs have attracted more attention to be used as a nano-filler for polymer composites due to their unique properties such as excellent electrical and mechanical properties, low density, and high aspect ratio [39].

In 1991, Iijima et.al. [40] announced the finding of a novel allotropic carbon form with a unidirectional structure. This substance was given the name "Multi-Walled Carbon Nanotubes," shortened as "MWCNTs. The arc discharge approach was used to create "Single-Walled Carbon Nanotubes" (SWCNT) two years later. The graphene sheet is characterized by the hexagonal arrangement of carbon atoms. A SWCNT or MWCNNT is formed by wrapping single or several graphene sheets, respectively, (Figure 2.2). For SWCNTs, this wrapping results in a seamless cylinder, whereas for MWCNTs, it results in layered graphene cylinders organized around a central hollow core [35].

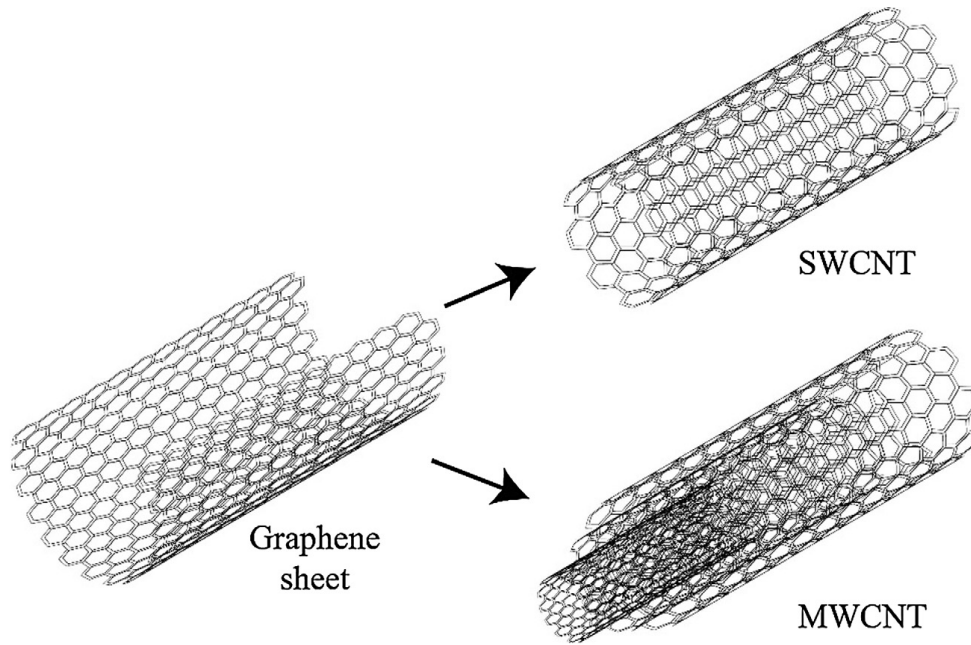


Figure 2.2: Structure of Graphene sheet, SWCNT and MWCNT [40].

CNTs have been the subject of much research from both a basic and practical standpoint since their invention. based on experiments and simulations, by adding CNTs into a polymer, even in a small amount, the electrical conductivity of the composite will rise dramatically, without significantly reducing the intrinsic properties of the polymers. Due to the high aspect ratio of CNTs, making an electrically conductive path inside the polymer would be more probable at a low concentration of filler which defines as electrical percolation, and will lead to a cost-effective product. Understanding and predicting the overall electrical conductivity of the composites with the incorporation of the conductivity mechanisms are essential for engineering applications. These extraordinary combinations of the unique qualities of PDMS and superb electrical conductivity and mechanical properties of CNTs, have made CNT-PDMS nanocomposite a favorable material candidate for many applications, such as wearable sensors, electrical routing, electromagnetic shielding, energy harvesting, etc. [41]. Even though the mechanical properties of all MWCNTs/PDMS nanocomposites were better than those of neat PDMS, there was a gradual

decrease in these values when MWCNTs content was further increased. Also, the Thermal conductivity of carbon nanotubes covers a wide range. Phonon-enhanced conduction methods result in thermal energy transfer. These processes are influenced by a variety of factors, including the number of active phonons, the length of the free route, and the distance for phonon diffusion, all of which are influenced by the length and diameter of the CNTs [35]. Choosing the suitable technique for the development of CNTs inside a polymer matrix should be done carefully depending on the kind of NPs and the needed attributes. The way the fillers are disseminated inside the polymer matrix is determined by the techniques and production methods, hence the final characteristics of the conductive polymer are heavily influenced by them [35].

CNTs content in the matrix is another factor that affects the dispersion of nanoparticles, since above a critical CNTs concentration, CNTs tend to form aggregates which can cause deterioration of the mechanical properties of nanocomposites [14]. Furthermore, Good dispersion and long-term stability of CNTs in various matrices are required to fully realize the entire potential of CNTs. Moreover, due to the increased contact at the interface between the polymer matrix and the fillers, improved filler dispersion improves the mechanical characteristics of carbon nanotube-polymer composites.

Chemical treatment and mechanical treatment are the two approaches that may be used to produce homogeneous and long-term stability of CNT inside the polymer matrix. Chemical treatments include the wet-mechanic-chemical reaction method that is using acid treatment, electrophilic addition of functional groups under microwave irradiation, and plasma treatment. While mechanical treatments are considered as physical mixing of the nanoparticle in the base matrix using ultra-sonication, shear mixing, and magnetic stirring. Among these, ultra-sonication with

increased power offers significant energy to de-agglomerate particle clusters with substantial impaction on nanoparticle clusters, allowing for homogenous mixtures to be obtained.

2.3. Methodology

2.3.1. Materials

CNT15 with an outer diameter of 8 to 15 nm and length of 10 to 15 μm with >95% purity was used and purchased from Cheap Tubes. PDMS was purchased from SYLGARD 184 Silicone Elastomer Kit (Dow Inc., USA). A PDMS mixture was prepared by mixing the base elastomer and curing agent at 10:1 by weight using an Ultrasonic Processor (750W, Vibra-Cell™). It was placed in a desiccator hooked up to a 2562B-01 vacuum pump (Welch, USA) to remove air bubbles within the mixture. The PDMS was placed in a furnace at 60°C for 20-30 minutes to cure.

2.3.2. PDMS/MWCNT fabrication

In this work, a composite of MWCNT and PDMS has been developed. To obtain a homogeneous distribution of MWCNTs inside the polymer and also make MWCNTs functionalize, an optimized dispersion technique using isopropyl alcohol (IPA) in combination with ultra-sonication was used. Because both MWCNTs and PDMS are quite soluble in isopropyl alcohol (IPA), IPA was used as a solvent. IPA has an amphiphilic structure (three hydrocarbon units and one hydroxyl group). The hydrophobic component of the carbonaceous nanotube complexes (CNT/IPA complexes), adheres to the highly hydrophobic MWCNT surface, generating IPA-coated MWCNTs with hydroxyl groups on the outer layer [12].

By mixing and sonicating MWCNTs and IPA and consequently exerting physical forces on the MWCNTs by the ultrasound source to overcome van der waals forces between attached nanotubes, powerfully aggregated MWCNT bundles will temporarily get detached, and space between

MWCNTs will be filled with IPA. After sonicating for around 10 minutes, a small amount of silicon oil (MEP) was added and blended into the solution for 10 minutes by sonication. MEP has $-(\text{CH}_3)_2\text{SiO}-$ structural unit and more important, it is a non-volatile polymeric organosilicon material [12]. MEP clings to the hydrophobic MWCNT surface via penetrating the IPA phase in individual MWCNT/IPA complexes. Then, PDMS will be added to the MWCNT/IPA/MEP sample and sonicated for 10 more minutes. By this method, PDMS will make direct contact with the MEP phase around MWCNT and consequently will have a stable and homogenized MWCNT/IPA/MEP/PDMS solution as you can see in Figure 2.3. Then the sample will be placed in the oven at 70 °C for 30 minutes until IPA is vaporized.

Figure 2.4 also shows the schematic preparation method of the whole mixture including the pouring and peeling off method. Based on the mold geometry, different shapes and sizes can be simply generated. By this method, the final sample will ensure high flexibility, elasticity, and electrical conductivity along with biocompatibility and mechanical stability. Figure 2.5 showed step by the step fabrication process.

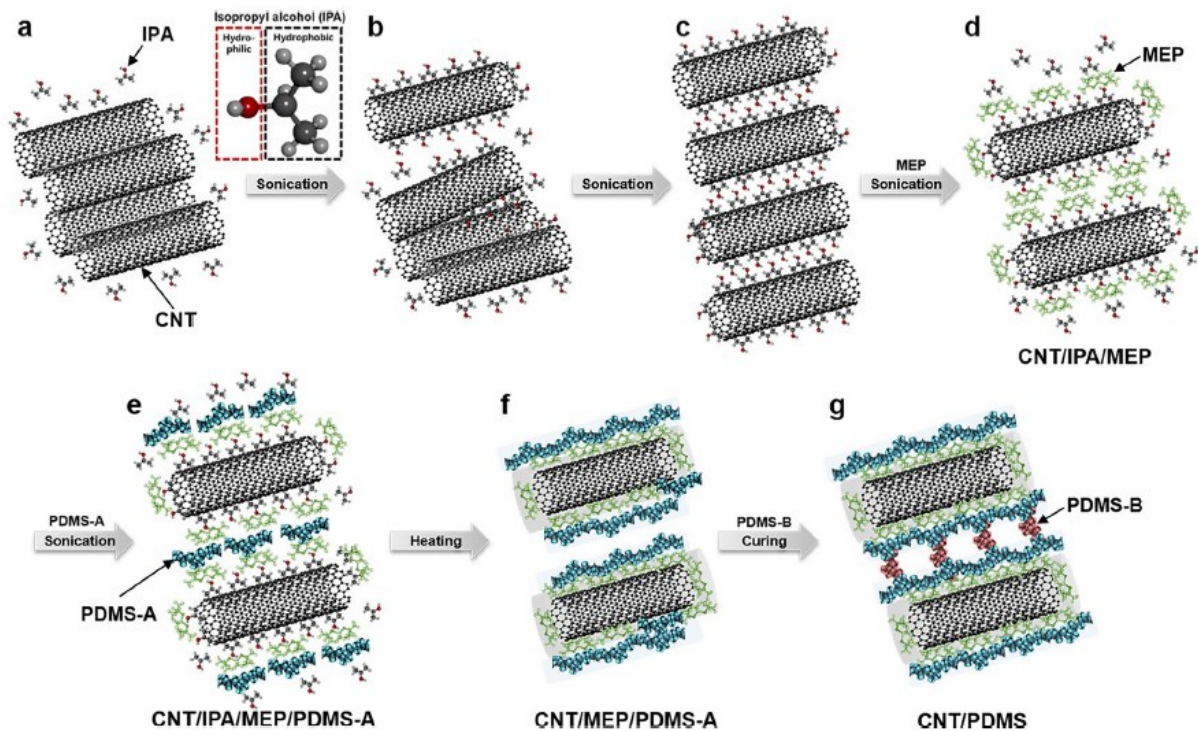


Figure 2.3: Schematics of CNT/PDMS composite fabrication. (a-c) dispersion of aggregated [12]. CNTs in IPA solution using ultra-sonication. (d) addition of MEP which wrapped the CNT/IPA. (e) PDMS-A was added and attached to MEP. (f) IPA is evaporated by heating. (g) fabrication of CNT/PDMS composite by adding a curing agent (PDMS-B) for cross-linking of PDMS [12].

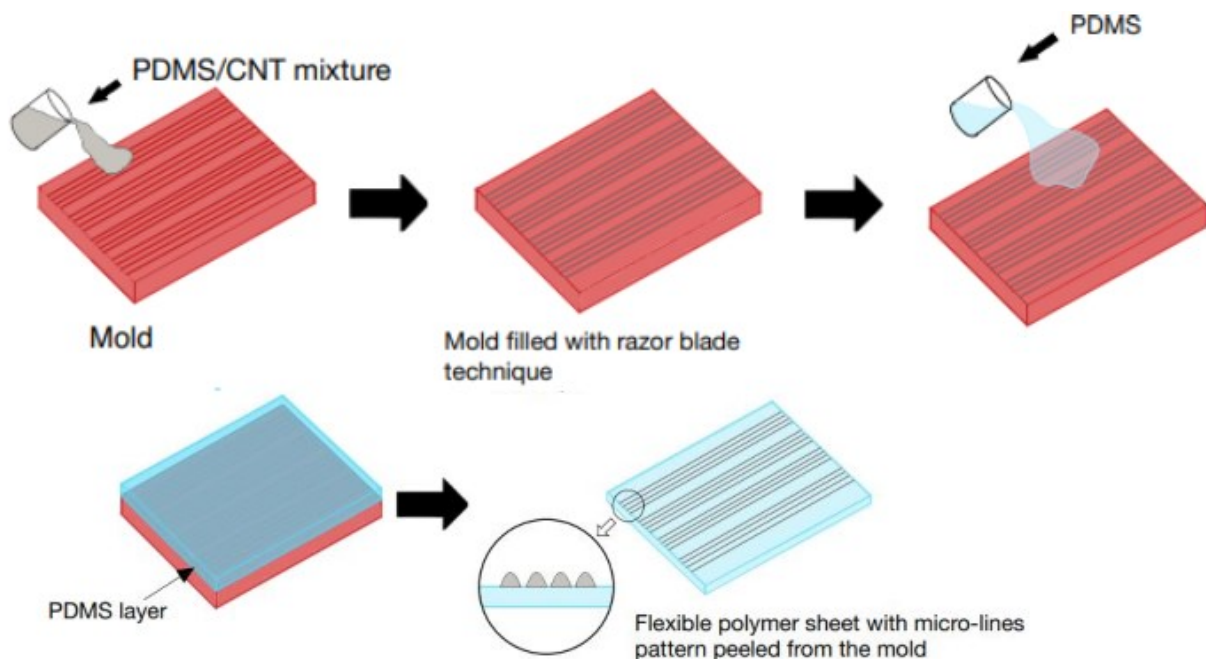


Figure 2.4: Mixture preparation following with pouring method

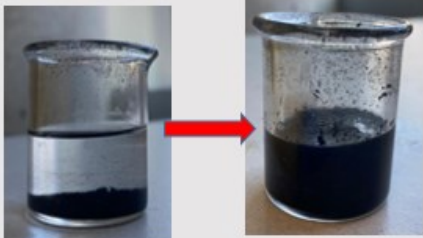
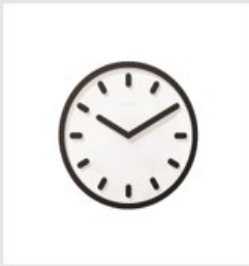
Step 1: Sonication (10 min per addition)	Step 2: Oven Drying (70°C for ≈30 min)	Step 3: Curing Agent + Mold and add PDMS upper layer
		
Step 4: Oven (65°C for ≈30 min)	Final Product	Quantities
		<ul style="list-style-type: none"> ▪ Chosen %wt CNTs and PDMS ▪ 100:1 IPA to CNTs ratio ▪ 20 wt% MEP Silicone oil ▪ 10:1 PDMS-curing agent ratio
		Sonication Order <ul style="list-style-type: none"> ➤ IPA and CNTs ➤ Add Silicone oil ➤ Add PDMS base

Figure 2.5: Step-by-step fabrication process

2.3.3. Electrical Measurements

To measure the resistance, a two-point probe multi-meter has been used. The probes were placed on top of the conductive lines with a known distance and then resistance (R_{10}) was read from the multi-meter (distance between measuring probe was 10 mm). The resistivity (ρ , measured in ohm meter, $\Omega \cdot m$), and conductivity (σ , measured in siemens per meter, S/m), can be calculated using Equations (2.1) and (2.2), respectively.

$$\rho = \frac{R_{10} \times A}{l} \quad (2.1)$$

$$\sigma = \frac{1}{\rho} \quad (2.2)$$

Where R is the resistance in ohms (Ω), A is the cross-section area in m^2 and l is the length between the probe tip in meters (m). Figure 2.9 displays the conductivity of the CNT30 and CNT15 in different wt.%.

2.3.4. Thermal Measurements

A constant 5V potential was applied to the conductive lines by the DC-regulated power supply and the temperature was measured by a thermocouple (Figure 2.6). DAQExpress software was used to record the temperature in real time. Figure 2.7 also shows schematic of setup configuration for temperature test.

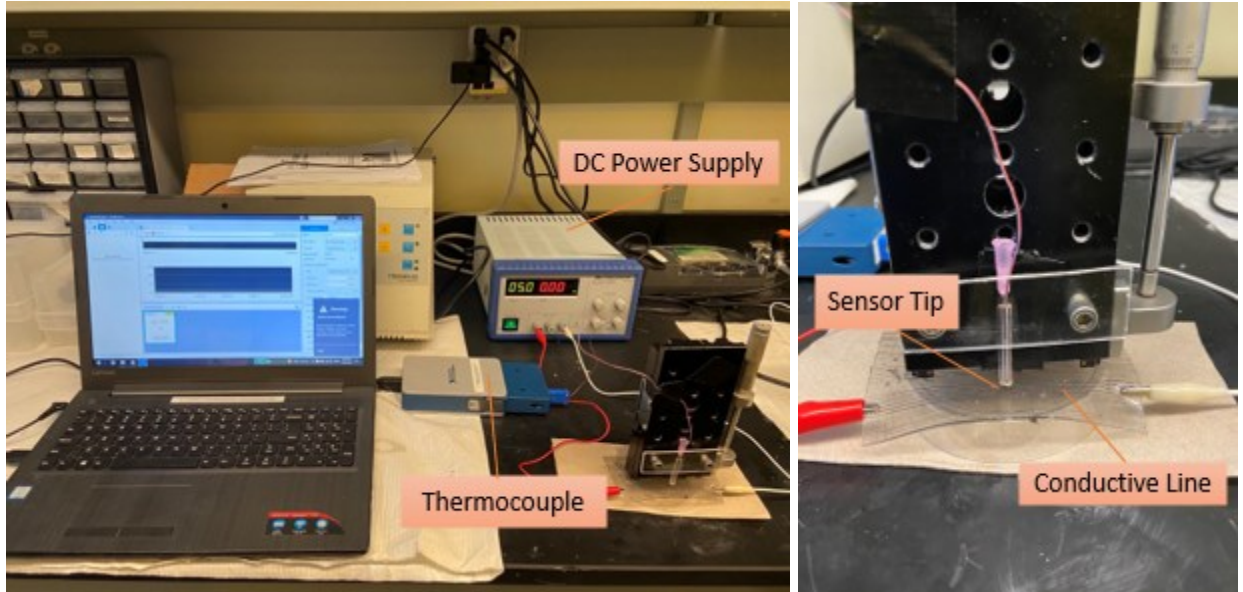


Figure 2.6: Setup configuration for temperature test.

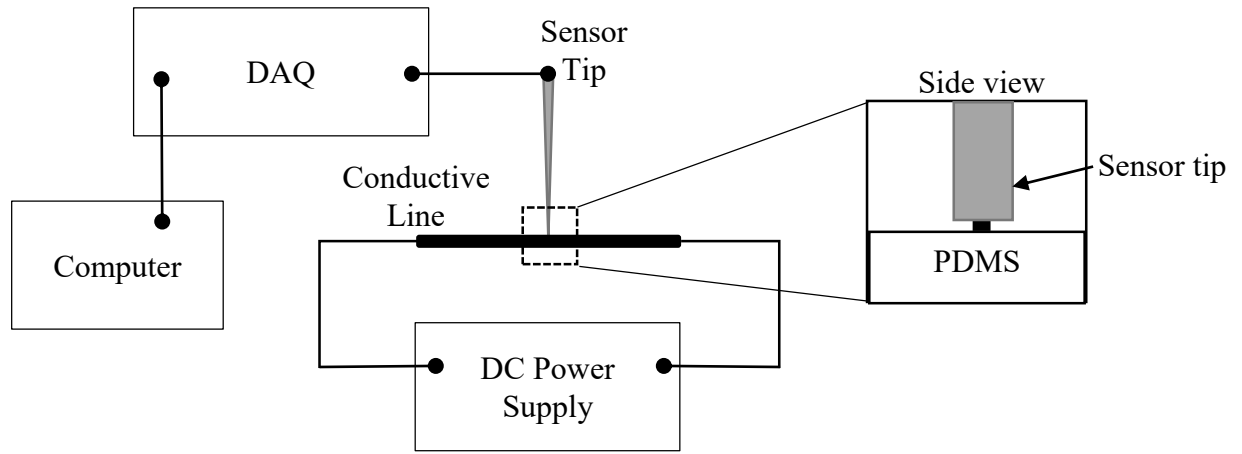


Figure 2.7: Schematic of setup configuration for temperature test.

2.4. Results and discussion

2.4.1. Electrical Properties of MWCNT/PDMS composites

Different ratios of MWCNT/PDMS composite have been tested to reach the best electrical conductivity. In our experiments two different MWCNTs have been examined, CNT30, which has an outer diameter of 10-30 nm and length of 10-30 μm , and CNT15, which has an outer diameter of 8-15 nm and length of 10-50 μm . CNT15 has a higher length-to-width aspect ratio that might affect the results. Different percentages from 18 to 50 wt% of MWCNTs have been analyzed. Figure 2.8 shows the resistance of the conductive lines by increasing the MWCNT (Table 2.1).

The measuring distance of the probe for resistance is 10 mm (R_{10}). The results indicated that by increasing the number of MWCNTs in the polymer matrix, resistance will decrease exponentially. However, while CNT30 and CNT15 decrease at different rates, both reach the same resistance at 35 wt.%.

It is pertinent to note that no prior literature has reported on the addition of carbon nanotubes (CNTs) in polydimethylsiloxane (PDMS) at a concentration exceeding 30 wt.%. However, in our study, we surpassed this concentration level by incorporating CNTs up to 50 wt.%. It is imperative to mention that as the concentration of CNTs was increased to 40 and 50 wt.%, the curing time of the composite material increased to six hours. This phenomenon represents a significant challenge that has not been addressed in previous studies that were limited to CNT concentrations of up to 30 wt.%.

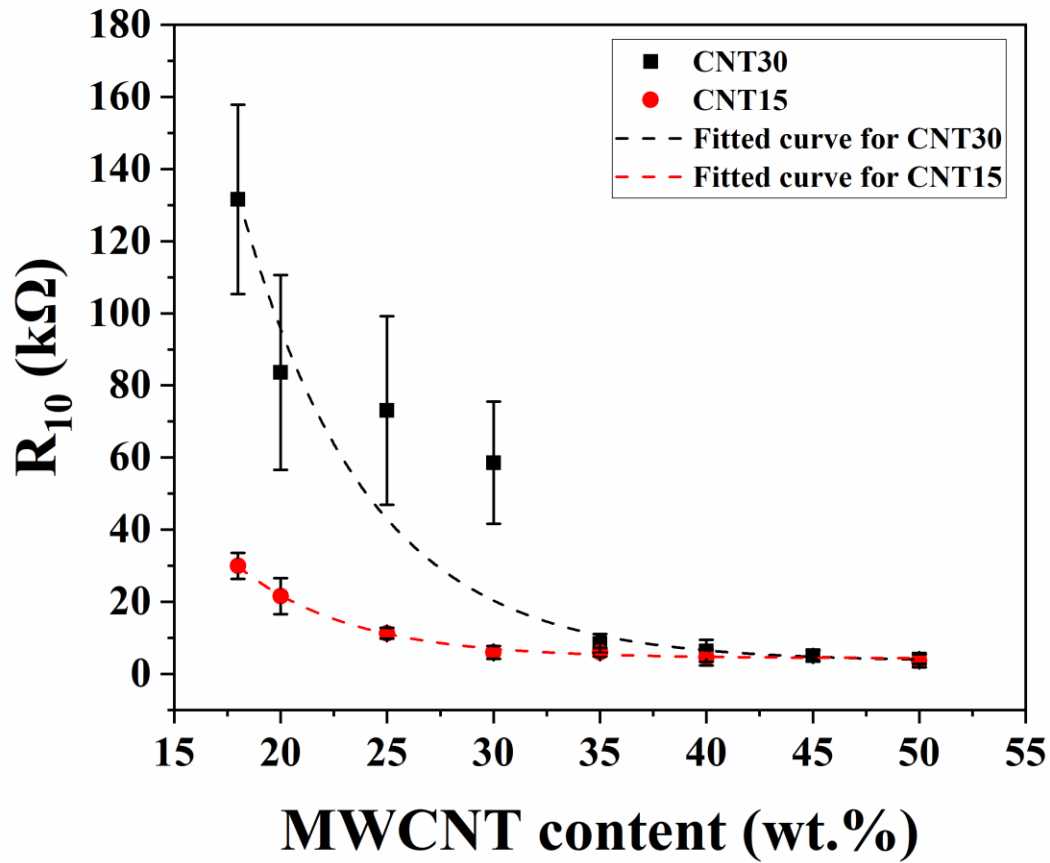


Figure 2.8: Resistance variation by MWCNTs percentage (CNT30 and CNT15) (error bar indicates range, n=10).

Table 2.1: Measured resistance for PDMS/MWCNT composite with varying wt.% of cnt30 and CNT15 .

Percentage (wt. %)	CNT30 Resistance, R_{10} (kΩ)	CNT15 Resistance, R_{10} (kΩ)
18	131.60 ± 26.22	30.00 ± 3.59
20	83.63 ± 26.99	21.60 ± 4.96
25	73.10 ± 26.13	11.30 ± 1.53
30	58.55 ± 16.94	6.02 ± 1.76
35	8.43 ± 2.64	6.05 ± 1.14
40	6.42 ± 3.04	4.63 ± 2.22
50	4.16 ± 1.32	3.78 ± 1.88

In Figure 2.9, a transversal cut of our micro-lines is shown in clarity, which is taken with a scanning ultrafast electron microscope (SUEM). Although there is no obvious separation between the PDMS and the conductive composition, it is still possible to distinguish the two materials, demonstrating how strongly they have bonded. This demonstrates that even though the electrical lines and PDMS are attached, neither material will disperse into the other during preparation.

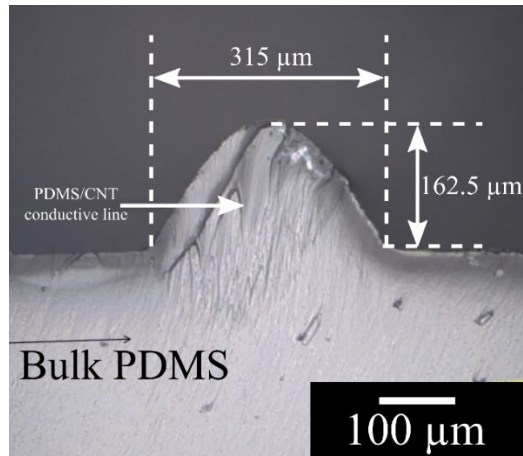


Figure 2.9: SUEM image of a cross-section of a micro conductive line.

The cross-sectional area of the line was also calculated to be $2.8 \times 10^{-8} \text{ m}^2$ and the distance between the probes was 10 mm. using both the cross-sectional area and length, it was possible to calculate the resistivity and conductivity using Equation (2.1) and (2.2) (Table 2.2).

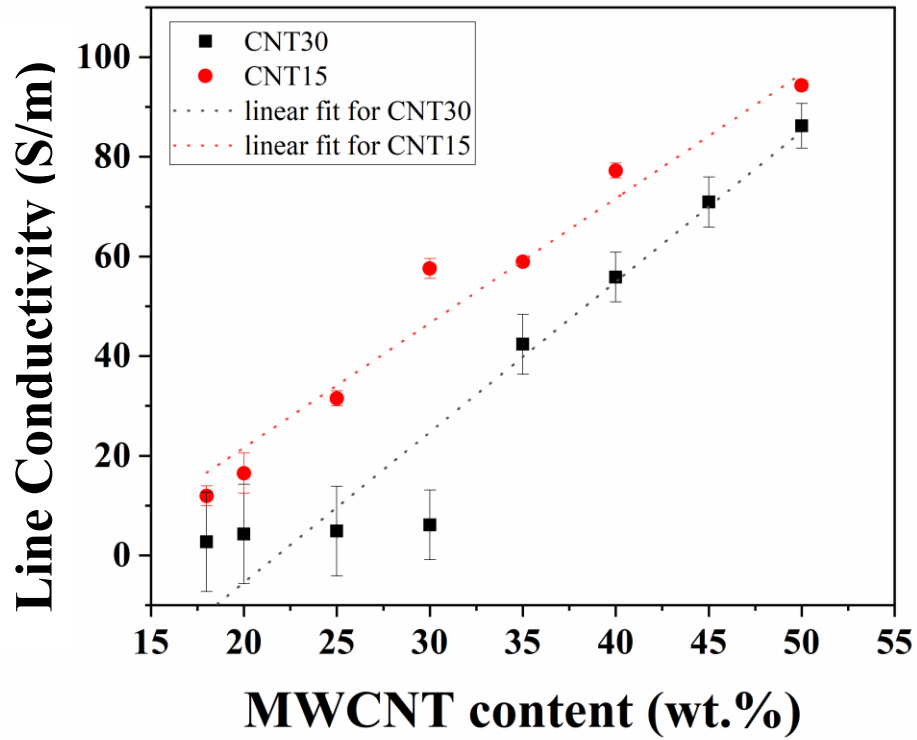


Figure 2.10: Conductivity of the CNT30 and CNT15 in different wt.% (error bar indicates range, n=10).

Table 2.2: Electrical properties of PDMS/MWCNT composites with CNT30 and CNT15.

Percentage (wt.%)	CNT30		CNT15	
	Resistivity, ρ ($\Omega\cdot\text{m}$)	Conductivity, σ (S/m)	Resistivity, ρ ($\Omega\cdot\text{m}$)	Conductivity, σ (S/m)
18	0.3686	2.71	0.0840	11.90
20	0.2341	4.27	0.0605	16.51
25	0.2046	4.88	0.0310	31.51
30	0.1639	6.10	0.0173	57.55
35	0.0236	42.37	0.0169	58.95
40	0.0179	55.86	0.0129	77.22
50	0.0116	86.20	0.0106	94.33

Figure 2.10 shows a linear increase of conductivity with MWCNT content for composites with both CNT30 and CNT15. The highest conductivity achieved was 94.44 S/m for CNT15, while the

second highest is 86.20 S/m for CNT30, both at 50 wt.%. This is attributed to the increasing aspect ratio of the fillers, which improves the conductive paths inside the polymer [41]. However, results reported in the literature achieved significantly higher conductivities. Ozhikandathil et al. [13] reported a conductivity of 285.7 S/m using the same mixing and preparation method, but with the addition of aqueous gold chloride and silver nanoparticle to their solutions.

A flexibility test was conducted on the composite material whereby the conductive line was subjected to bending, and the resultant resistance was measured to detect any possible alterations. The findings indicated that the resistance remained unaffected despite the bending, and no cracks were detected on the line. Thus, it can be deduced that the composite material under scrutiny exhibits considerable flexibility.

2.4.2. Thermal Characterization (Joule heating study)

Figure 2.11 shows the temperature profiles of micro-lines with 30 wt.% and 50 wt.% CNT 15. Both samples were measured at room temperature (23 °C). As soon as the current passed through the lines the temperature increased drastically and reached 106 °C and 65 °C for 30wt.% and 50wt.% MWCNTs, respectively. The test was carried out for 15 minutes, and after turning the current off, the temperature dropped immediately to 40°C before slowly cooling to room temperature. The temperature raise was due to the resistance of the line, and as Figure 2.11 indicates for higher resistance, the temperature increased more.

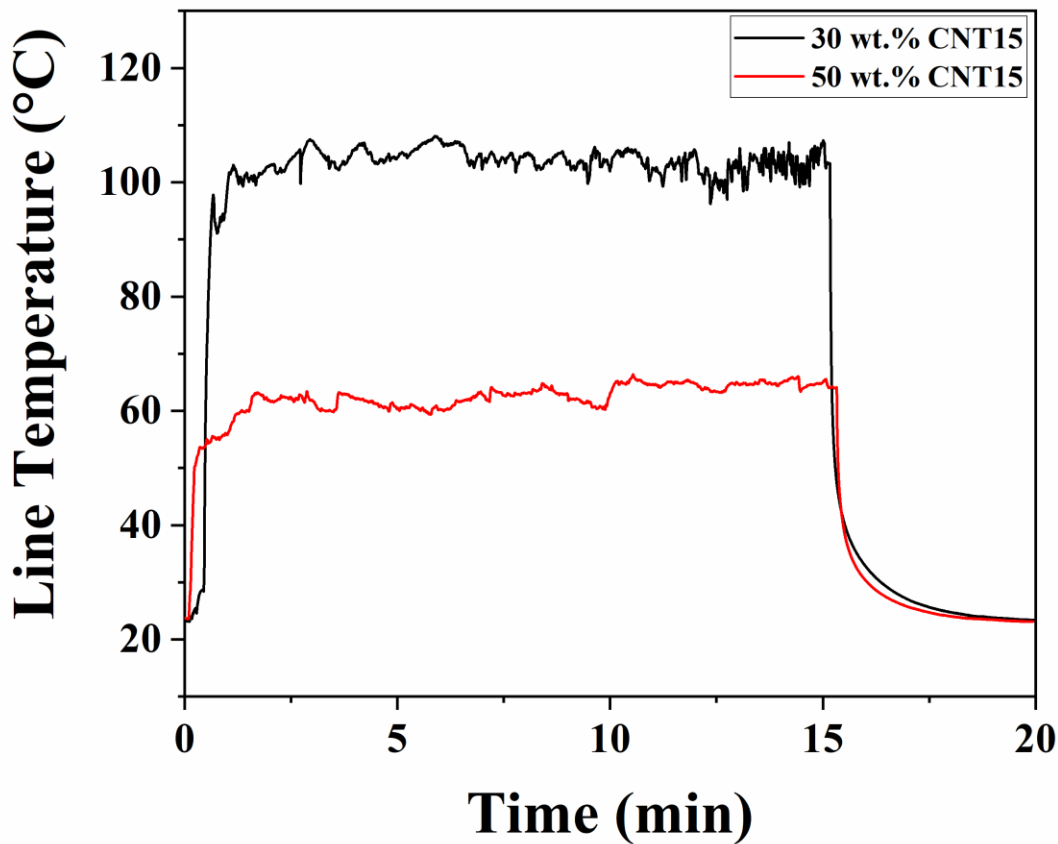


Figure 2.11: Temperature variation by time by applying voltage for PDMS + MWCNTs 30 wt.% and PDMS + MWCNTs 50 wt.%.

2.5. Conclusion and Future Research

In this chapter, MWCNTs were mixed with PDMS to fabricate conductive lines. Previous works have not investigated composites that contain more than 30 wt.% MWCNT. Two different MWCNTs of different sizes were evaluated to investigate the effect of the filler's aspect ratio on conductivity. The best conductivity that could reach by this method was 94.33 S/m for CNT15 at the 50 wt.%. However, other work by Ozhikandathil et al. [13] reached a resistivity of $0.0035 \Omega \cdot \text{m}$, (or conductivity of 285.7 S/m). Though their process was similar [13] they also used aqueous gold

chloride solution and silver nanoparticles in their solutions. While the results obtained show a novel fabrication method, there is still room for improvement.

Adding other fillers such as silver and gold might have a better impact on the conductivity and it needs to be investigated. Also, the base polymer which was PDMS in this study is an insulative polymer. Using a conductive polymer could also be an interesting subject to work on it.

Finally, the Joule heating study was conducted on lines of CNT15 at 30 and 50 wt.% of showed that by passing a current through the line, the temperature increased from room temperature to 100 °C in less than a minute. The results indicate that these PDMS/MWCNT mixtures are suitable for temperature-sensitive devices, such as temperature sensors, thermocouples, or thermal cut-offs.

Chapter 3. Integration of Silver Nanoparticles into MWCNT/PDMS

Composites for Improved Electrical Properties

Integrating silver nanoparticles into MWCNT/PDMS (multi-walled carbon nanotubes/polydimethylsiloxane) is a promising approach for developing new materials with improved properties. MWCNT/PDMS is a composite material that combines the strength and electrical conductivity of carbon nanotubes with the flexibility and durability of PDMS. The addition of silver nanoparticles can further enhance the electrical conductivity and antibacterial properties of the material. The integration of silver nanoparticles into MWCNT/PDMS can be achieved by several methods, such as in-situ synthesis, electrochemical deposition, and physical mixing. The resulting composite material can have a wide range of potential applications in fields such as electronics, biomedicine, and energy storage.

3.1. Introduction

Combining metallic conductive nanomaterials such as gold nanoparticles and silver nanoparticles with CNTs, the advantageous characteristics of two components in hybrid materials, and their applications are also mentioned in the literature [42-44]. Among all the metallic fillers, the Ag-CNT component has attracted much attention due to its potential application as an optical limiter [45], advanced material [46], and catalyst [47]. Silver nanoparticles (AgNP) are well known for having outstanding biological, mechanical and electrical properties [48]. In a work by Liang et al.[49] For the first time, fully stretchable white polymer light-emitting diodes (PLEDs) were successfully fabricated using a polyurethane acrylate (PUA) film coated with graphene oxide-soldered (GO) silver nanowire (AgNW) percolation network (GO-AgNW/PUA) as the transparent conductive electrode (TCE). In the GO-AgNW network, GO sheets were wrapped around the

AgNWs and their junctions, reducing inter-nanowire frictional resistance and preventing nanowire disjoining and sliding. According to the results, the GO-AgNW network stretchability was improved, while electrical conductivity did not decrease under high tensile strain [49].

Amjadi et al. [50] reported a strain sensor with high stretchability and sensitivity based on AgNW/PDMS elastomer nanocomposites. The maximum stretchability of the sensor is 70%, and it has a strong piezoresistivity with tunable gauge factors (GFs) ranging from 2 to 14 depending on the loading of Ag NW [50]. Choi et al. [51] could electrolyte Ag-plated MWCNTs, to examine the impact of plating time on the thermal conductivity of Ag-plated MWCNTs-reinforced epoxy matrix composites. According to the findings, the composites' thermal conductivity improved with longer plating times. Particularly, the Ag-10/EP sample demonstrated a greater than 150% increase in thermal conductivity when compared to the CNTs/EP sample that had been received [51]. In research by Xin et al. [52] silver could be successfully added to carbon nanotubes by using the N, N-dimethylformamide (DMF). The outcomes demonstrated that when compared to pristine CNTs, Ag-CNTs could significantly enhance the mechanical and electrical conductivity of the polymer. The highest electrical conductivity that they could reach was 100 S/m [52]. In other work done by Ma et al. [53], to improve the electrical conductivity of carbon nanotubes (CNT), a straightforward method for coating them with AgNPs was created. Silver-decorated CNTs were created by functionalizing CNTs using ball milling in the presence of ammonium bicarbonate and then reducing silver ions in N, N-dimethylformamide. 100 S/m was the highest conductivity that they could achieve [53].

3.2. Methodology

3.2.1. Materials

As discussed in Chapter 2, the highest conductivity that could reach was 94.33 S/m with CNT15. Here, AgNP has been combined with CNT15 to enhance the conductivity of the polymer. The AgNP was less than 100 nm, which contains PVP dispersant, 99.5% trace metals basis (Sigma-Aldrich, USA).

AgNP was incorporated at different ratios. Previous results showed that the highest conductivity for MWCNT/PDMS composites sample was achieved at 50 wt% filler (CNT15) and 50 wt% polymers (PDMS). Samples were prepared at the same ratio, with AgNP and MWCNT accounting for half composite by weight. By varying the MWCNT to AgNP ratio, four different compositions (Table 3.1), were achieved. The area of the line was $2.8 \times 10^{-8} \text{ m}^2$ and the distance between each measuring probe was 10 mm.

Table 3.1: Composition of different samples with varying MWCNT and silver content

Sample	Composition (wt%)		
	MWCNTs (CNT15)	AgNP	PDMS
C30S20	30	20	50
C35S15	35	15	50
C40S10	40	10	50
C45S05	45	5	50

3.2.2. Fabrication

To ensure a homogenous distribution of AgNP within the composite, two mixing methods have been employed. Method 1 is similar to the method of fabricating for MWCNT/PDMS composites described in Section 2.3. MWCNT was added to IPA at 1:100 by weight, then ultrasonicated for 10 minutes. MEP is added at 1:5 to PDMS and ultrasonicated for 10 minutes, then the PDMS is

added, and the solution is ultrasonicated for another 10 minutes. AgNP is added and the mixture is ultrasonicated a final time for 2 minutes. The solution is then placed in a furnace at 70°C for 30 minutes to evaporate the IPA. In method 2, there is one change, when AgNP is added, instead of ultrasonication to exert mechanical force on the particles shear mixing is used.

3.3. Results

Figure 3.1 demonstrates the variation of the resistance in different samples mixed by ultrasonication and shear force method. As it shows, in the ultra-sonication method by increasing the amount of the CNTs, the resistance will decrease constantly, and the lowest resistance was 3.66k Ω for C45S05. On the other hand, in the shear mixing method, resistance is descending until 35 wt.% (C35S15) and after that by adding more CNTs, resistance started to increase. the possible theory for this action is the lack of force exerted on the mixture to de-agglomerate the CNTs inside the polymer. Also, Figure 3.2 shows the conductivity change by each sample for both shear mixing and ultra-sonication. According to the results, the highest conductivity that could reach was 121.21 S/m which was achieved for the C45S05 sample by ultra sonication.

Detailed information regarding resistance, resistivity, conductivity and standard deviation can be find in Table 3.2 and Table 3.3.

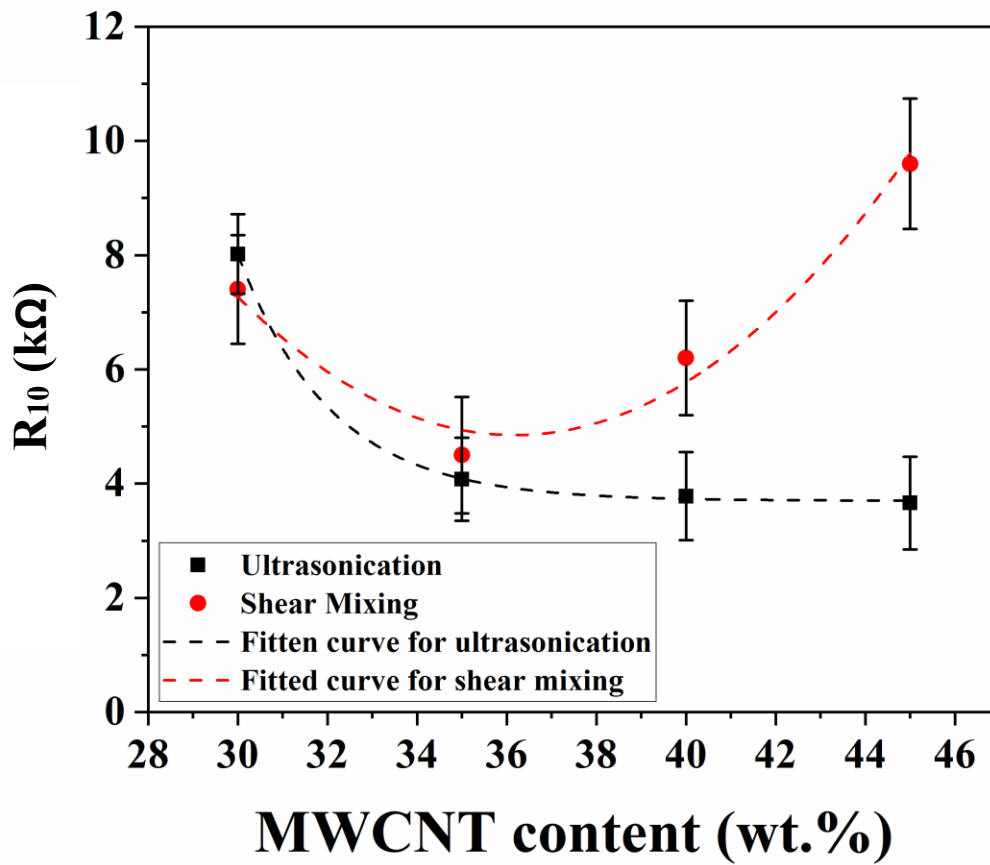


Figure 3.1: Resistance variation in different MWCNT/AgNP ratios, mixed with ultra-sonication and shear force (error bar indicates range, n=3).

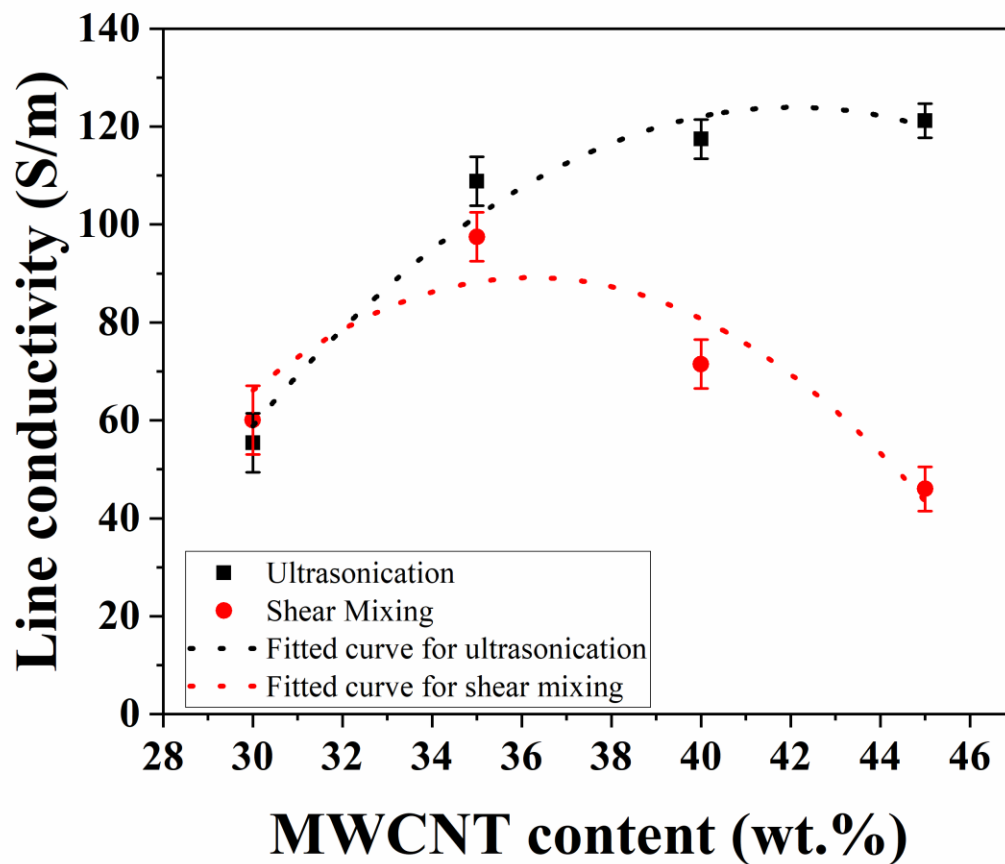


Figure 3.2: Conductivity variation in different MWCNT/AgNP ratios, mixed with ultra-sonication and shear mixing (error bar indicates range, n=3).

Table 3.2: Measured resistance for PDMS/MWCNT/AgNP composites, blended with ultra-sonication and shear mixing(n=3).

Sample	Ultra-sonication resistance (k Ω)	Shear mixing resistance (k Ω)
C30S20	8.02 \pm 0.70	7.4 \pm 0.9
C35S15	4.08 \pm 0.73	4.5 \pm 1.0
C40S10	3.78 \pm 0.77	6.2 \pm 1.0
C45S05	3.66 \pm 0.81	9.6 \pm 1.1

Table 3.3: Electrical properties for MWCNT/AgNP, blended with ultrasonication and shear mixing (n=3).

Sample	Ultra-sonication		Shear mixing	
	Average Resistivity, ρ ($\Omega\cdot\text{m}$)	Average Conductivity, σ (S/m)	Average Resistivity, ρ ($\Omega\cdot\text{m}$)	Average Conductivity, σ (S/m)
C30S20	0.01665	60.06	0.01804	55.41
C35S15	0.01025	97.50	0.00918	108.84
C40S10	0.01398	71.49	0.00851	117.47
C45S05	0.02174	45.99	0.00825	121.21

3.3.1. Scanning Electron Microscopy

To have a clear view of the whole mixture, SEM images have been taken. Figure 3.3 shows a top-down view of the conductive line. A mixture of PDMS, CNT15, and AgNP (C45S05) is shown. From the SEM images, larger silver nanoparticles (white dots) can be seen to have sunk to the bottom (area A) and smaller silver nanoparticles floated at the top (area B), area C is PDMS mold.

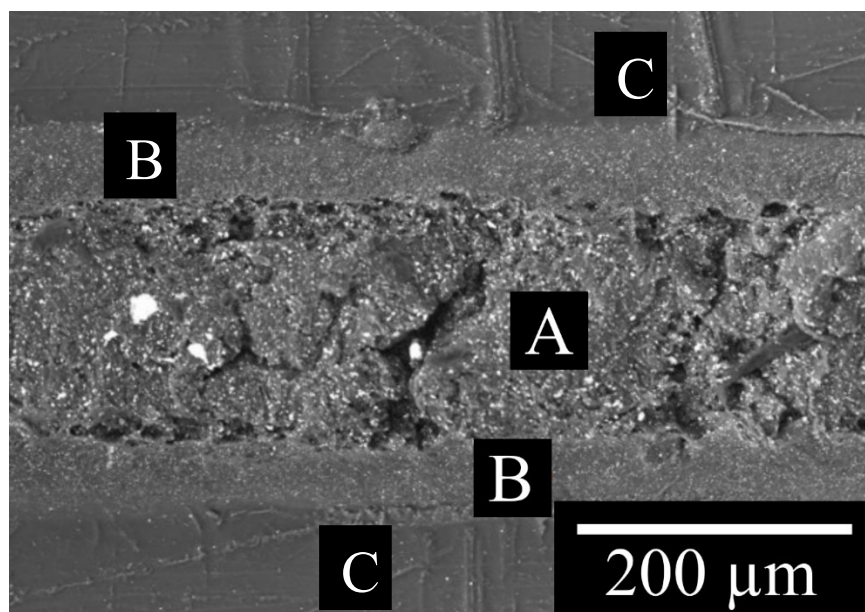


Figure 3.3: SEM image of C45S05. (Area A refers to zone of large AgNP, Area B refers to small AgNP, and Area C refers to PDMS mold.)

Figure 3.4 shows a close-up of a PDMS/CNT/AgNP line. Due to fabrication taking place in an ambient atmosphere, it is possible oxidation occurred, which has a considerably negative effect on the conductivity. To determine whether AgNP oxidized within the sample, chemical analysis has been carried out. Table 3.4 shows that the oxygen level at the silver particles is the same throughout the sample, as clarified by the analytical data. This indicates that there is no oxidation of the silver within the composite. Spectrum 1, 2, 3 and 6 is at A section which contains larger AgNP, spectrum 4 is at B section which mostly has smaller AgNP and spectrum 5 is pure PDMS.

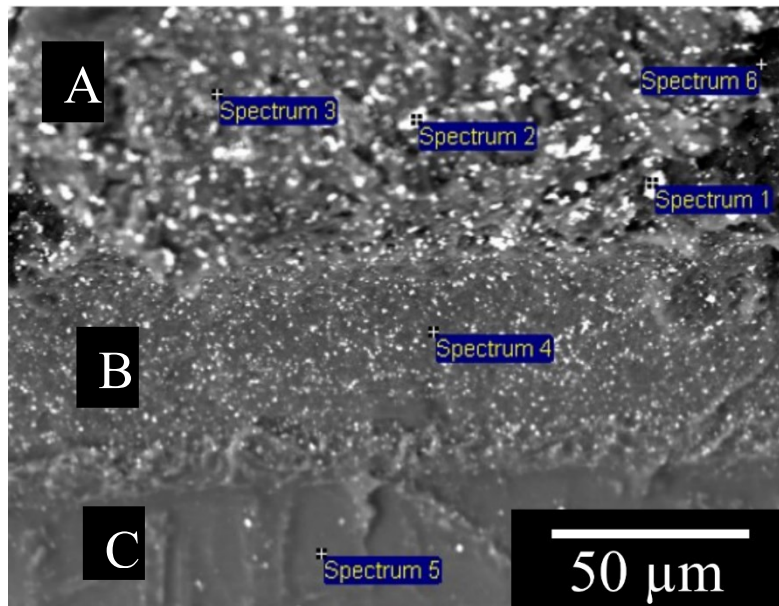


Figure 3.4: Chemical analysis of PDMS, MWCNT and AgNP

Table 3.4: Analytical data of the PDMS, MWCNT and AgNP.

Spectrum	Carbon in %	Oxygen in %	Silicon in %	Silver in %
Spectrum 1	13.82	27.20	15.19	43.79
Spectrum 2	13.01	20.52	15.42	51.05
Spectrum 3	56.45	28.99	13.10	1.45
Spectrum 4	58.11	30.08	11.43	0.38
Spectrum 5	52.91	27.81	18.59	0.69
Spectrum 6	40.40	29.36	19.43	10.81
Mean	39.12	27.33	15.53	18.03
Std. deviation	20.86	3.49	3.08	23.21

3.3.2. Thermal Characterization (Joule heating study)

Two samples with different MWCNT/silver content (C45S05 and C35S15) were tested. A 5V potential was applied to the conductive lines by the DC-regulated power supply and the temperature was measured by a thermocouple (Figure 2.6). DAQExpress software was used to record the temperature in real-time.

Figure 3.5 demonstrate the temperature profile for these two micro-lines. before applying the voltage, the temperature was 23 °C (room temperature). At the moment that voltage was applied, the temperature started to raise very fast. In less than a minute the temperature for C45S05 which had resistance and conductivity of 3.66 k Ω and 121 S/m, respectively, reached 66 °C. For the C35S15 line, the pattern is the same, due to higher resistance (4.1 Ω) and lower conductivity (108.8 S/m), the temperature increased more to around 78 °C. Temperatures remained constant for the next 15 minutes and as soon as the voltage cut off, the temperature decreased drastically and reached room temperature. The test has been done 3 times for the straight line.

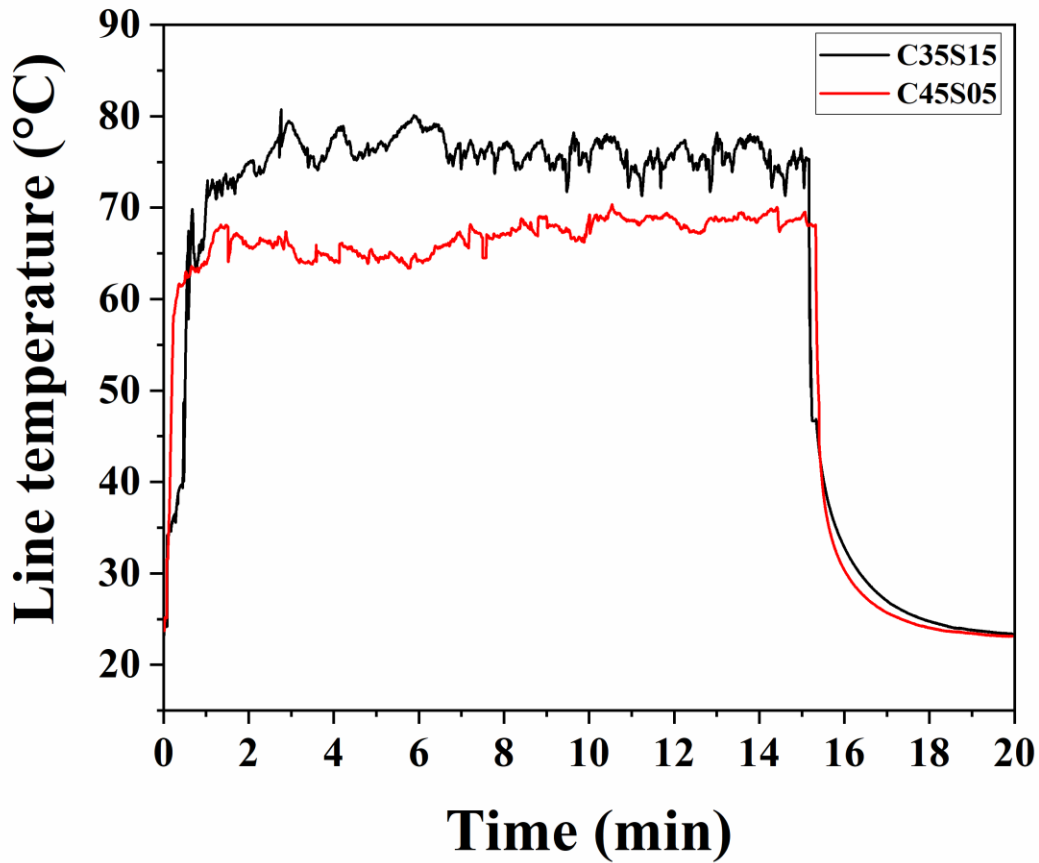


Figure 3.5: Temperature variation by time by applying voltage for C45S05 and C35S15.

3.4. Conclusion and Future Research

Comparing the results between the two mixing methods show us that by using ultra-sonication, the resistivity of the samples will reduce continuously by the addition of MWCNTs. Whilst, by using shear mixing in the last step, as it is clear in Figure 3.1, by increasing MWCNT by more than 35% resistivity will be increased. The main reason for this phenomenon is the aggregation of fillers inside the sample. By adding MWCNTs of more than 35%, shear forces exerted on the fillers are unable to disperse MWCNT/Silver NP and consequently, conductive paths will drop.

Moreover, a comparison of results with chapter 2, reveals that, by addition of AgNP to the CNT15/PDMS, the highest achieved conductivity will increase to 121.21 S/m, while this was 94.33 S/m for CNT15/PDMS sample at 50 wt.%. Therefore the addition of AgNP will be beneficial to enhance the conductivity.

However, by adding AgNP, it was expected to have far better conductivity than 121.21 S/m. SEM images revealed the reason for this failure. smaller and larger silver NP have been separated in the tapered shape line. Large AgNP stayed at the center which is deeper and smaller AgNP have been floated to the edge of the line. And because it is smaller NP that makes the connection, conductive paths have not been created effectively. Also, according to the Joule heating characterization, these lines have a fast response to the applied voltage. So they might be a good choice for thermal sensing applications.

Chapter 4. Development and Electrical Characterization of PEDOT:PSS

PEDOT:PSS is a conductive polymer blend that has gained widespread attention due to its unique electrical properties and potential applications in various fields, such as flexible electronics, sensors, and energy harvesting devices. The development of PEDOT:PSS involves the synthesis of two different polymers, namely, PEDOT and PSS, which are blended together in a specific ratio to achieve the desired electrical conductivity and film-forming properties. The electrical characterization of PEDOT:PSS involves several techniques, such as four-point probe measurement, impedance spectroscopy, and current-voltage curve analysis, to evaluate its conductivity, charge transport properties, and stability under different conditions. These studies have shown that PEDOT:PSS exhibits high electrical conductivity, good transparency, and excellent stability, making it a promising candidate for various applications in the emerging field of flexible electronics.

4.1. PEDOT:PSS

PEDOT is a highly conductive polymer that is popular for use in flexible-conductive materials. The electrical conductivity of thin films and single crystals can reach 6259 and 8797 S/cm, respectively [54-56]. Since the initial PEDOT patent was secured by Bayer AG in early 1988, the material has been used in a wide range of applications, such as energy harvesting devices [57]. Nevertheless, PEDOT is insoluble in water, which is a significant obstacle barring its widespread adoption in manufacturing processes. For simplicity of processing, the polymer is frequently ionically crosslinked with a water-soluble polymer, PSS, forming an organic semiconductor,

PEDOT:PSS [58] (Figure 4.1). PSS acts as a counter-ion by leveling the charge of PEDOT, increasing the stability of the polymer.

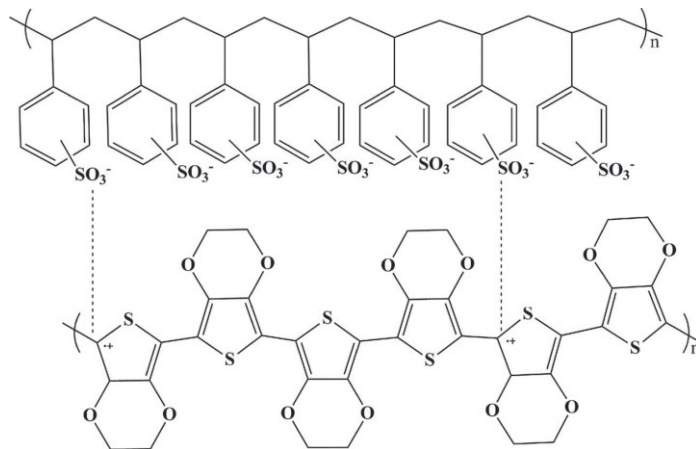


Figure 4.1: Chemical structure of PEDOT:PSS [59]

PEDOT:PSS is one of the most significant and effective conducting polymers. Both fundamental research and commercial applications have benefited greatly from it [60]. Films of PEDOT:PSS is well-known for their thermal stability, allowing them to be heated in air at 100°C for over 1000 hours with just minor changes in electrical conductivity [61]. Due to its excellent electrical conductivity, high transparency in the visible range ($>90\%$), great thermal stability, environmental stability, flexibility, and also ease of growth in thin film form, PEDOT:PSS is an organic conducting polymer that is actively utilized in flexible organic electronics [61, 62].

However, PEDOT:PSS, by itself, has a low conductivity of ~ 100 S/m due to its PSS^- chains [63]. The major drawback to the inclusion of PSS is the reduction of the electrical conductivity of the mixtures, which limits the utilization of the polymer for a wide range of applications [58]. This decrease in conductivity requires a second dopant. The inclusion of CNTs (Figure 4.2) to enhance the electrical conductivity of the PEDOT:PSS has attracted much attention in recent years [64, 65].

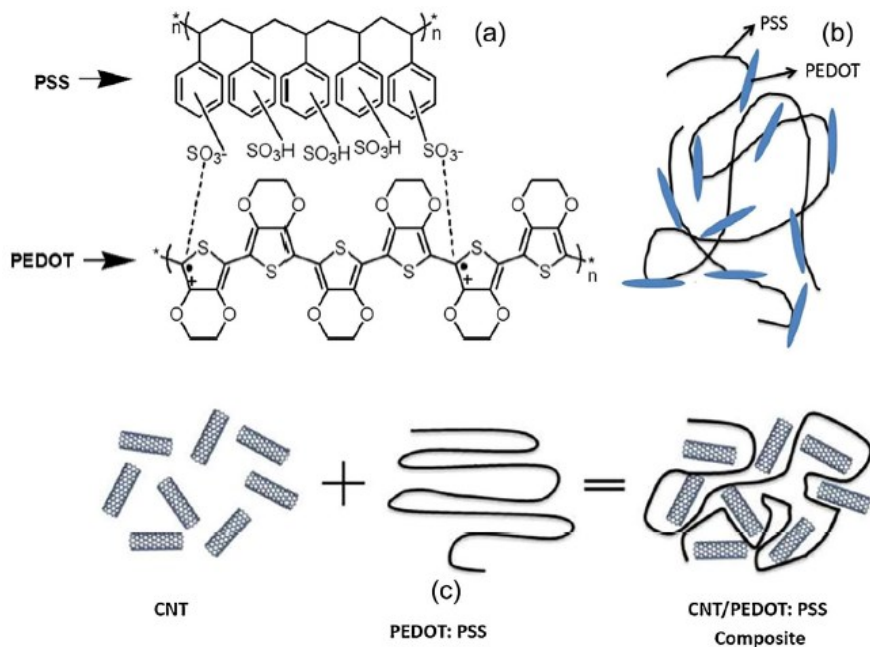


Figure 4.2: (a) Chemical structure of PEDOT:PSS, (b) Schematic structure of PEDOT:PSS, and (c) Schematic representation of MWCNT polymer composite [62]

To improve the conductivity of the polymer, many different approaches have been explored. Additional charges frequently result in higher conductivity due to increased electron mobility throughout the structural chain and ionic dispersion between the PEDOT and PSS components [58]. Tunable electrical properties are obtained by the structural engineering of PEDOT:PSS, using physical, chemical, and mechanical techniques [58].

Thermal treatment and the insertion of conductive nanofillers are foremost among the methods used in the physical approach [66-68]. Chemical alterations are accomplished by procedures such as solvent treatment and the insertion of salts and acids [69, 70]. The mechanical technique involves techniques such as ultrasonic vibration of the polymer substrate during casting for structural refining [71-73]. Besides improved electrical properties, the mechanical and structural properties of the polymer are highly favorable for applications like optoelectronics and electrochemical devices, and flexible and portable electronic applications such as energy harvesting and storage devices [58, 74]. As a result, due to a lack of intrinsic mechanical

properties, to perform as ideal engineering components, they are frequently strengthened with finer nanoparticles [75].

A growing number of studies on PEDOT:PSS composite films as flexible electrodes have been published in the last decade, and show that the electrical properties of PEDOT:PSS are extensively influenced by the film morphology, and chemical and physical structures, which can be altered using several post-processing techniques including treatment with thermal, light and solvent processes, as well as the use of additive fillers. Huang et al. [76] investigated the influence of heat treatment on the conductivity of spin-coated PEDOT:PSS in both air and N₂ atmospheres from 100 to 250 °C. Additionally, the effect of annealing temperature on the performance and conductivity of organic photodetectors and solar cells made by PEDOT:PSS layer has been studied and it shows that the optimum device performance, in particular, external quantum efficiency (EQE) and open-circuit voltage (V_{oc}) at 250 °C [76]. Multiple studies show that thermal treatment is a viable option for increasing the conductivity of PEDOT:PSS [77].

In organic electronic devices, PEDOT:PSS films are commonly used as a hole injection layer. To maintain a reasonable device performance, conductivity and work function improvements are required [59]. Ultraviolet (UV) irradiation as a light treatment is the most favorable technique that can be employed to increase the conductivity and work function of the PEDOT:PSS composite. Moujoud et al. [78] used X-ray Photoelectron Spectroscopy (XPS) and Ultraviolet Photoelectron Spectroscopy (UPS) to explore the electronic and structural changes in PEDOT:PSS films after UV treatment, and to determine the means of conductivity improvement. Moreover, the addition of organic solvents such as dimethyl sulfoxide (DMSO), tetrahydrofuran (THF), N,N-dimethyl formamide (DMF), glycerol, poly ethylene glycol (PEG), sorbitol and diethylene glycol to PEDOT:PSS leads to an increase in conductivity at room temperature [63]. Among these, glycerol

and EG have attracted significant interest, as numerous studies suggest that glycerol or EG doping dramatically enhances the conductivity of PEDOT:PSS [79, 80].

The conductivity of the PEDOT:PSS can also be enhanced by adding conducting fillers, such as silver nano particles, graphene oxide and CNTs [81]. The inclusion of carbon nanotubes to the polymer matrix has caught researchers' curiosity as a potential nano-filler for increasing the conductivity of PEDOT:PSS [82], and composite PEDOT:PSS/MWCNT flexible electrodes have recently been employed in high-performance super capacitors [83]. These MWCNTs have a high aspect ratio, making them a good filler for forming a continuous and homogeneous conducting network in a polymer matrix. The synthesis of MWCNT networks in the polymer matrix and the interaction between the thiophene ring of PSS and carbon nanotubes enhance the conductivity of the PEDOT:PSS/MWCNT composite, allowing for easier charge transport through the polymer matrix. Moreover, the presence of carbon nanotubes in the PEDOT:PSS polymer matrix improves the composite's mechanical strength [62].

Mannayil et al. [62] studied the effect of MWCNT inclusion in a PEDOT:PSS matrix with concentrations of 0-2 wt% MWCNT by spin coating PEDOT:PSS/MWCNT on glass substrates. According to their results, the addition of 2 wt% of MWCNT leads to conductivity increasing from 100 S/m to 200 S/m. In another study, Hasan et al. [84] investigated the effects of acid-based post-treatment and polyethylenimine (PEI) concentration on the thermoelectric characteristics of PEDOT:PSS and SWCNT films used to harvest energy from the human body and were able to design a unique wearable thermoelectric generator with vertically aligned p-type PEDOT:PSS and n-type single-wall carbon nanotube (SWCNT).

This chapter describes the invention of carbon nanotube-based conducting polymer composite films, which provide excellent opportunities for developing easy-to-manufacture, flexible, light-

weight, and low-cost electrodes for electrical routing. For the fabrication of conductive composite, the current work uses a simple synthesis procedure. The novelty lies in the fabrication of highly stable and flexible composite film and its application on electrical routing. Even though there are many reports on PEDOT:PSS / MWCNT composite films synthesized using various techniques, to the best of our knowledge, PEDOT:PSS / MWCNT as a flexible and stable composite synthesized by ultra-sonication technique is rarely reported.

4.1. Methodology

4.1.1. Materials

MWCNT with outer diameter of 8 to 15 nm and length of 10 to 15 μm with >95% purity were purchased (Cheap Tubes Inc., USA). PEDOT:PSS was purchased from Sigma-Aldrich, as a 1.3wt% dispersion in water (density of $\sim 1\text{g/mL}$). Polyethylene Glycol and Glycerol were also purchased from Sigma-Aldrich. The mixtures were mixed using a VCX 750 ultrasonicator (Sonics & Materials, Inc., USA).

4.1.2. Mold Patterns

SolidWorks was used to design three different molds (Figure 4.3), which were then made with a Form 2 Stereolithography (SLA) 3D Printer (Formlabs Co., USA). All channel, are 2 mm wide and have a depth of 300 μm .

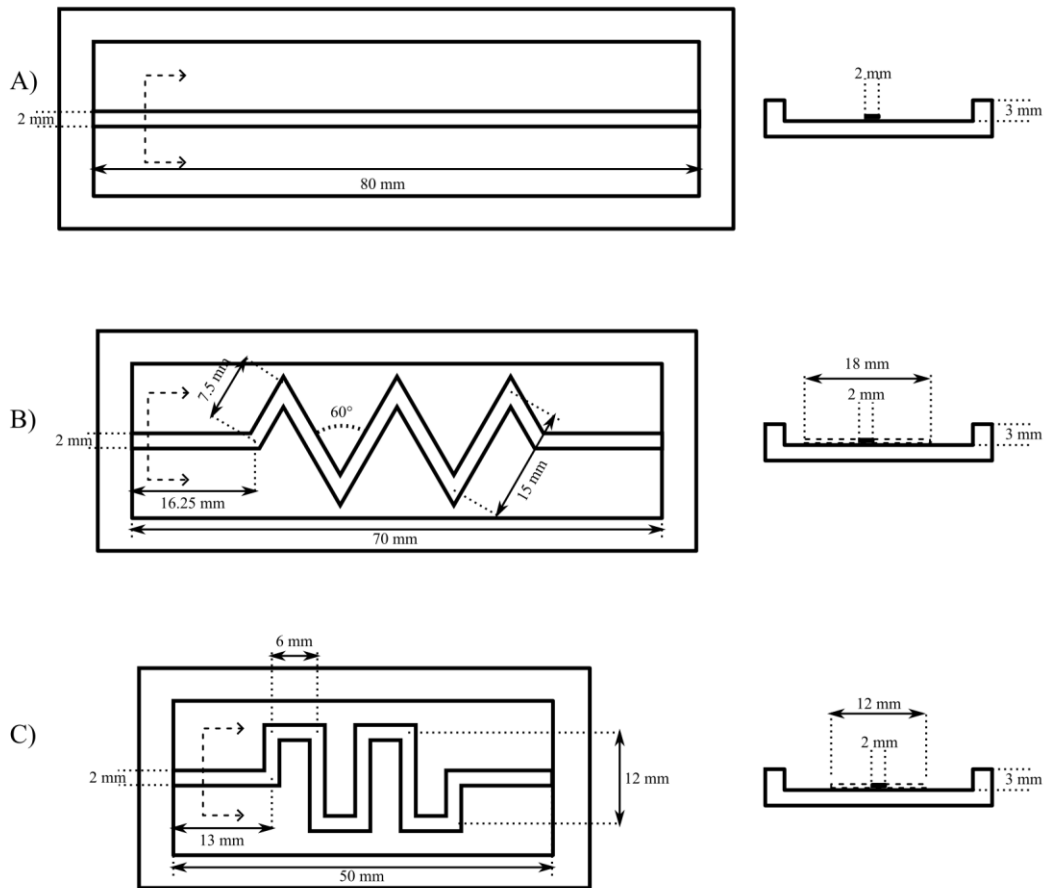


Figure 4.3: dimensions of the A) straight B) serpentine and C) zigzag channel (mm)

4.1.3. Fabrication of PEDOT:PSS/MWCNT Composites

MWCNTs are metallic in nature, and their integration in a polymer matrix can improve the composite's conductivity. MWCNT-based conductive film networks require good dispersion of MWCNTs in the polymer matrix, as well as homogeneity and stability of their dispersed solution [62].

An improved dispersion process combining isopropyl alcohol (IPA) and ultra-sonication was employed to achieve a homogenous distribution of MWCNTs inside the polymer matrix as follows:

CNT is added to IPA at 1:100 (by mass). First, 0.05g of CNT was measured in a glass beaker, and 5g of IPA is added to the CNT. The solution is ultrasonicated mechanically (750W, 40% power, pulse 10 seconds on, 15 seconds off) for 10 minutes. Next, 1:2 (by volume) PEDOT:PSS to CNT-IPA was achieved by adding 3.18 mL of PEDOT:PSS to the solution. The mixture was ultrasonicated for 5 minutes with the same settings. Finally, 0.2 mL PEG and 0.4 mL glycerol were added to the PEDOT:PSS-CNT-IPA solution. The mixture was ultrasonicated a final time for 3 minutes with the same settings.

The mixture was poured into the channel and placed in the oven for 20 minutes at 60 °C until it cured. The paste poured inside the PDMS channel was initially above the channel, but it shrunk to less than 300 (depth of the channel) μm in the oven due to the evaporation of water from the PEDOT:PSS solution.

4.1.4. Thermocouple calibration

Temperature tests were conducted using a thermocouple. To ensure that the thermocouple was working properly, it was compared to a thermometer inside a batch of water. Figure 4.4 shows the Schematic setup of the calibration test. The water was heated, and the temperature was read off the thermometer and compared with the thermocouple. Figure 4.5 shows the comparison between the bath temperature measured by the thermocouple, which produces a straight line with a slope of one.

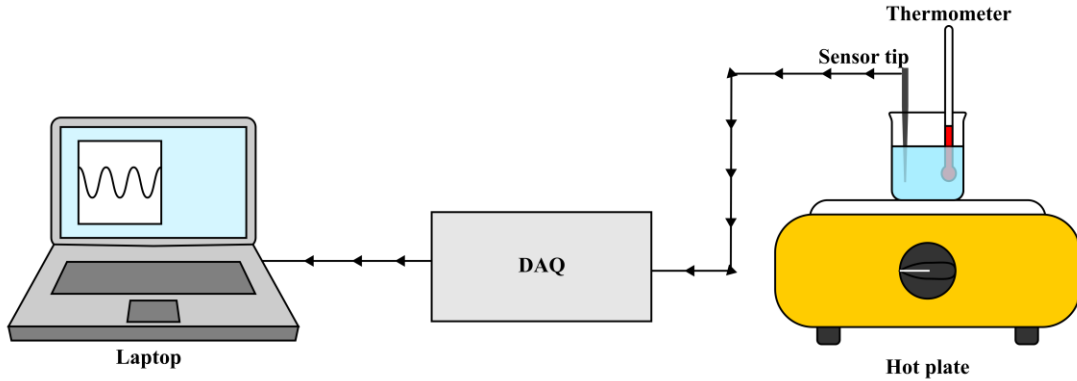


Figure 4.4: Schematic setup for the thermocouple calibration.

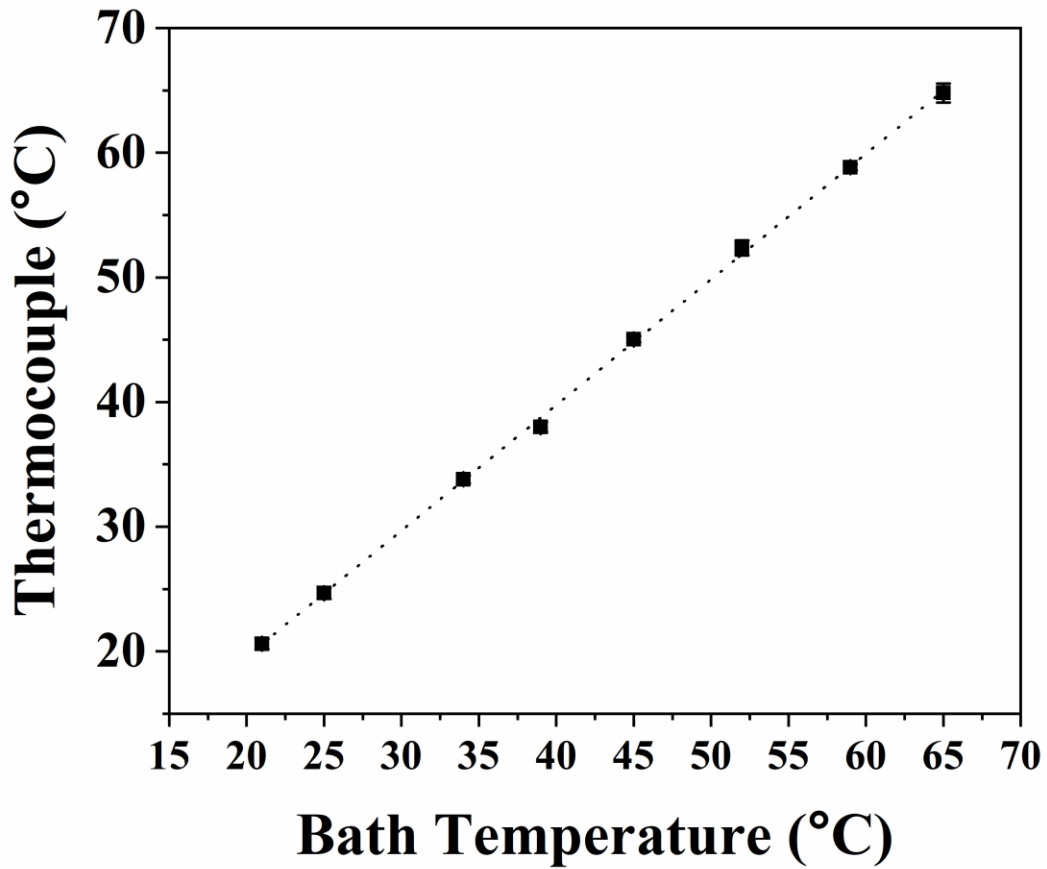


Figure 4.5: Comparison between Thermocouple and Thermometer (n=3)

4.1.5. Temperature tests

Two tests have been carried out. In the first test, conductive lines were heated up on the hot plate and the resistance in different temperatures was checked. the temperature was increased from 23 °C to 75 °C. To read the temperature, a thermocouple was used and the tip of the sensor was positioned in the conductive line (Figure 4.6).

At the second test the Joule heating was studied. the current was passed through the line by DC regulated power supply, and voltage was set to 5V, and the temperature of the line was measured for one hour, to study the response of the line concerning the current (Figure 4.7).

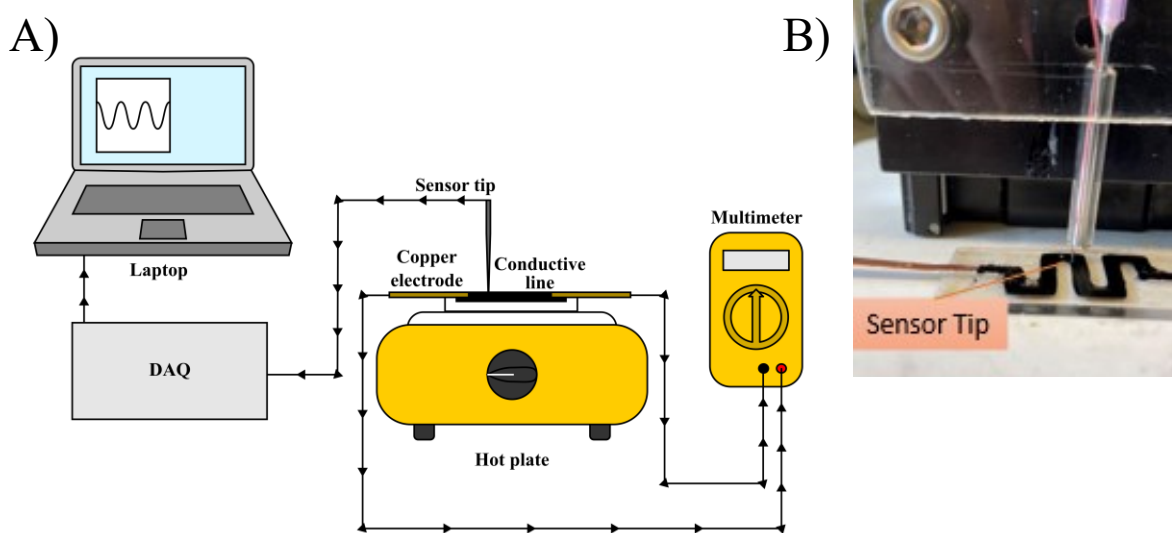


Figure 4.6: A) Schematic set-up for measuring resistance in different temperature on hot plate and B) Serpentine channel with sensor tip implanted.

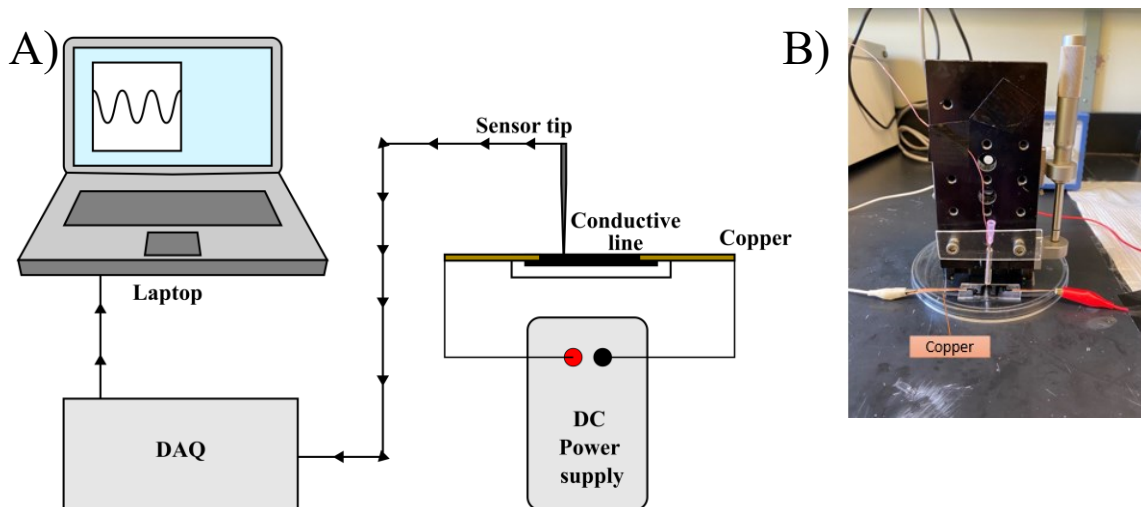


Figure 4.7: A) Schematic set-up for electro thermal test with DC power applied to line and B) Serpentine channel with sensor tip implanted.

4.2. Results and Discussion

Four different samples were analyzed to determine the effects of each additive on the properties of the composite: PEDOT:PSS, PEDOT:PSS+MWCNT, PEDOT:PSS+MWCNT+PEG and PEDOT:PSS+MWCNT+PEG+Glycerol. The main purpose of adding PEG and Glycerol to the mixture is to increase the flexibility of the cured composite. Table 4.1 shows the electrical properties of these four samples and as you can see, addition of MWCNT to the pure PEDOT:PSS resulted in reduction resistance. As mentioned earlier the main purpose of PEG and Glycerol is to increase flexibility. However, the addition of glycerol and PEG also decreases the resistance. The width of the channel was 2 mm and according to microscopic imaging height of the line is 0.24 mm, distance between measurement probes of the multi-meter was 10 mm (length).

Table 4.1: Electrical properties of PEDOT:PSS in addition to MWCNT, Glycerol, and PEG (n = 10)

Components	Average Resistance (Ω)	Average Resistivity ($\Omega\cdot\text{m}$)	Average Conductivity (S/m)
PEDOT:PSS	119.22 ± 14.66	0.0057	174.74
CNT/IPA + PEDOT:PSS	87.73 ± 9.08	0.0042	237.47
CNT/IPA + PEDOT:PSS + PEG	76.35 ± 10.64	0.0036	272.84
CNT/IPA + PEDOT:PSS + PEG + Glycerol	54.97 ± 10.44	0.0026	378.97

By using CNT/IPA + PEDOT:PSS + PEG + Glycerol, a conductivity of 378.97 (S/m) was attained, higher than what has previously been reported in the literature [13]. The findings are consistent with results seen in the literature, which shows a conductivity between 100 S/m and 300 S/m for 1 wt.% MWCNT in PEDOT:PSS [13].

4.2.1. Morphological Characterization

SEM images were taken of the PEDOT:PSS/MWCNT mixture to show its morphology. Figure 4.8 shows an SEM image of the PEDOT:PSS/MWCNT composite film. Morphological analysis indicated how MWCNT in PEDOT:PSS is randomly oriented. It is clear from the SEM pictures that the conducting route as a network structure forms by the long MWCNTs inside the PEDOT:PSS polymer.

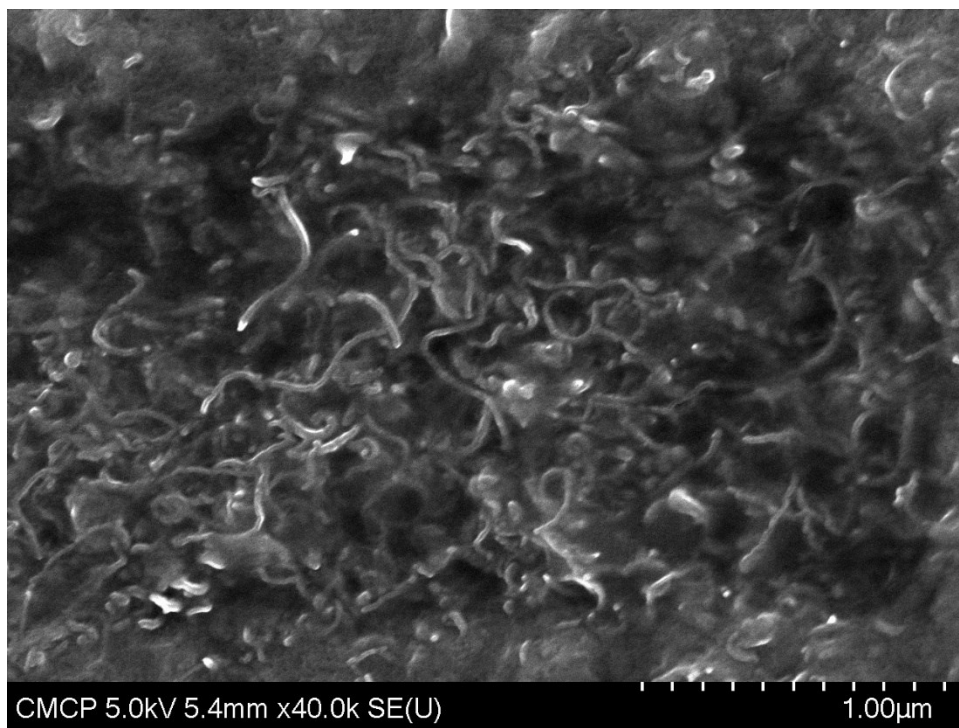


Figure 4.8: SEM image of the PEDOT:PSS and MWCNT composite

In Figure 4.9, the diameter of each MWCNT is indicated. The outer diameter (OD) of the MWCNTs as-received is 8 – 15 nm, whereas the OD within the PEDOT:PSS is larger. This increase in diameter can be attributed to PEDOT:PSS coating of the MWCNTs. It also reveals that PEDOT:PSS not only can be used as a conductive solvent but also as a conductive medium. Moreover, by coating PEDOT:PSS to the outer wall of MWCNTs, agglomeration of the filler has been reduced and it also helps to have a more homogenous mixture. In the mixture of PEDOT:PSS/MWCNT, since MWCNT is embedded in PEDOT:PSS medium, MWCNT and PEDOT:PSS function as guest and host components, respectively [62].

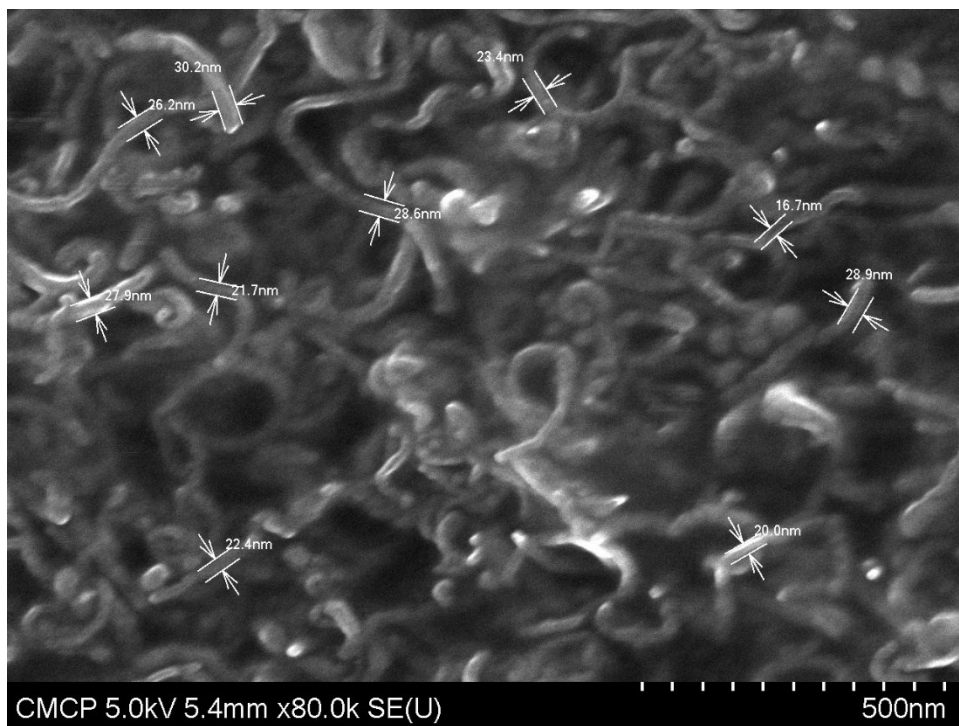


Figure 4.9: SEM image of the PEDOT:PSS and MWCNT composite along with the diameter of the MWCNTs
Once more, the CNTs are uniformly spread throughout this portion of the sample and no agglomerations are visible. Agglomerations would be a sign of poor CNT dispersion in the first step of our preparation, which involved sonicating CNTs in IPA to break the CNT bundles. These pictures imply that the CNTs were adequately coated as a result of the PEDOT:PSS and CNTs being sonicated and dispersed in IPA.

4.2.2. Impedance Analysis

To make sure that resistivity and conductivity do not change with varying channel dimensions, three lines of PEDOT:PSS/MWCNT with different lengths have been analyzed: 10 mm, 20 mm and 30 mm. The width of the lines was set to 2 mm, and the height (verified with microscopic imaging) was 0.24 mm. A 2-point probe was used to obtain the resistance of the lines (Table 4.2).

Table 4.2: Electrical properties of PEDOT:PSS/MWCNT mixture in different lengths (n = 3).

Length	Average Resistance (Ω)	Average Resistivity ($\Omega\cdot\text{m}$)	Average Conductivity (S/m)
L = 10 mm	70.4	0.00337	295.92
L = 20 mm	140.0	0.00336	297.61
L = 30 mm	207.5	0.00332	301.20

The results show that the length of the PEDOT:PSS/MWCNT mixture measured does not affect its resistivity. A new mold with a channel width of 1 mm was been fabricated to see if width affects the impedance of the PEDOT:PSS/MWCNT composite (Table 4.3). By comparing the results, it clarifies that resistivity and conductivity are independent of the dimensions of channels.

Table 4.3: Electrical properties of PEDOT:PSS/MWCNT mixture in different widths (n = 3)

Length and Width	Average Resistance (Ω)	Average Resistivity ($\Omega\cdot\text{m}$)	Average Conductivity (S/m)
L = 10 mm, W = 1 mm	135	0.00324	308.64
L = 10 mm, W = 2 mm	70.4	0.00337	295.92

4.3.3. Temperature Profiles

In the first temperature test, conductive lines were heated up on the hot plate and the resistance in different temperatures was checked. The setup for this test for the serpentine channel can be found in Figure 4.6. To read the temperature, a thermocouple was used and the tip of the sensor was placed into the conductive line. Figure 4.10 shows the channels filled with PEDOT:PSS/MWCNT mixture. The copper foil has been embedded into the PDMS substrate, and the probes were only in contact with the copper lines to measure the resistance.

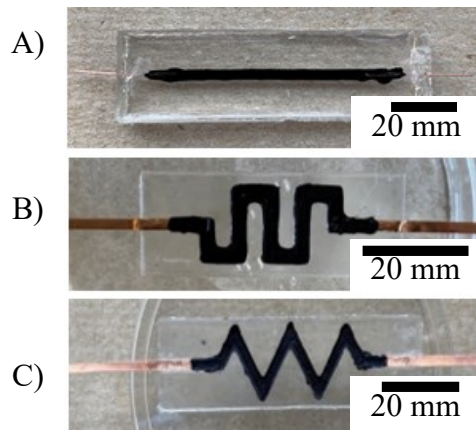


Figure 4.10: Top view of A) straight, B) serpentine and C) zigzag channels filled with PEDOT:PSS and MWCNT, with copper foils as electrodes.

It is noteworthy to mention that the effective length of the resistance line remained constant at 80 mm for all three channels, namely, straight, serpentine, and zigzag. Moreover, the measuring probes placed on top of the copper foil that attached to the conductive polymer.

Figure 4.11 shows the resistance of PEDOT:PSS/MWCNT composites (R_{80}) (R_{80} denoted that, distance between the measuring probes were 80 mm) as they are heated. Three different samples were analyzed as the temperature was increased from 23°C to 75°C. The results indicate that by increasing temperature, resistance will decrease. This test shows that we can use our conductive polymer composite as a temperature sensor, as it is sensitive to temperature.

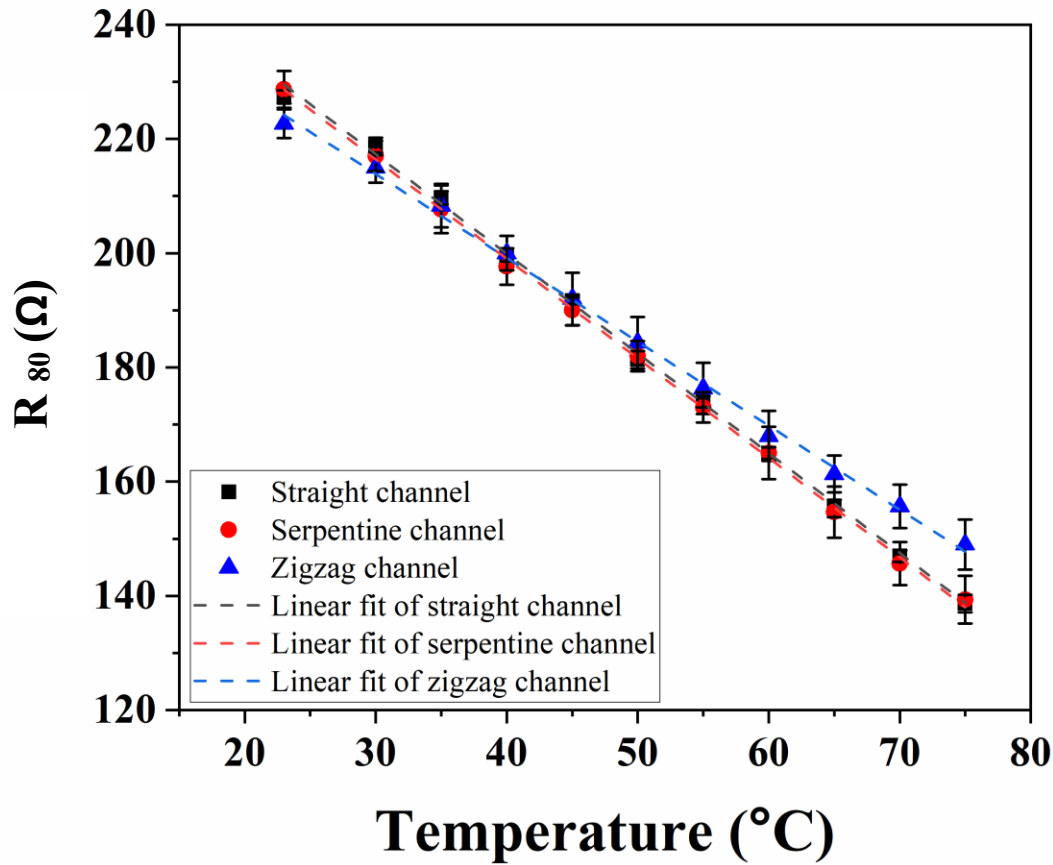


Figure 4.11: Change in resistance versus temperature of the straight, serpentine, and zigzag channels (error bar indicates range, n=3).

As it is clear, by increasing 53 °C, the resistance decreased by around 75 Ω for all the samples. It might be due to the movement of the free electrons by increasing the temperature which will result in making a better conductive path and reduction in the resistance.

In the second temperature test, the voltage was applied to the conductive line by a DC-regulated power supply and the temperature was measured by a thermocouple. According to Figure 4.12 Serpentine, zigzag and straight channels showed similar temperature profiles. When there was no current, the lines were at room temperature (22.5°C). As soon as the current was applied, the

temperature increased, and after 12 minutes reached 26°C. The current was held for 1 hour, during which time the temperature was stable at 26°C. After the current was shut down the temperature immediately began to drop until it reached room temperature.

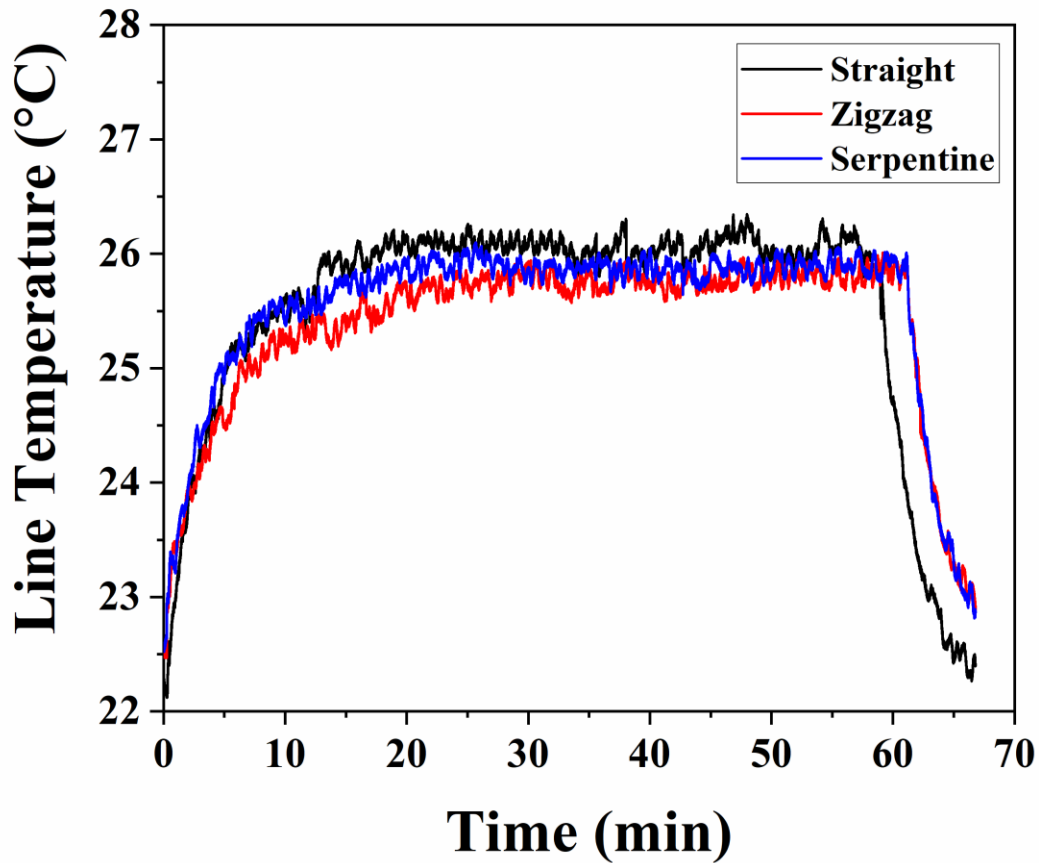


Figure 4.12: Temperature variation over time for straight, serpentine, and zigzag channels (n = 3)

As was shown in the previous test, resistance has an inverse relationship with temperature. According to Figure 4.12, the temperature increased by passing a 5V voltage, which means that resistance will be decreased in the conductive lines, and finally according to the ohm's law when voltage is constant and resistance decreased, current must increase. This temperature dependent piezo electric effect is seen in Figure 4.12.

4.3.4. Simulation of Temperature Profiles of Composite filament

To simulate our device, COMSOL Multiphysics has been used. Figure 4.13 shows the schematic model. The length of the channel was set to 80 mm, width was set to 2 mm and height was set to 300 μ m, which is equivalent to the experimental tests. The bottom substrate was assumed as PDMS and air properties were assigned to the top layer of the line. The electrical conductivity of the line was set to 370 S/m as we estimated it experimentally, and 5V has been applied to the conductive line. Other properties were assigned based on the literature as follows:

- Heat capacity at constant pressure, $C_p = 686 \text{ J/kg.K}$
- Relative permittivity = 217
- Density = 1.74 g/cm^3
- Thermal Conductivity = 300 W/m.K

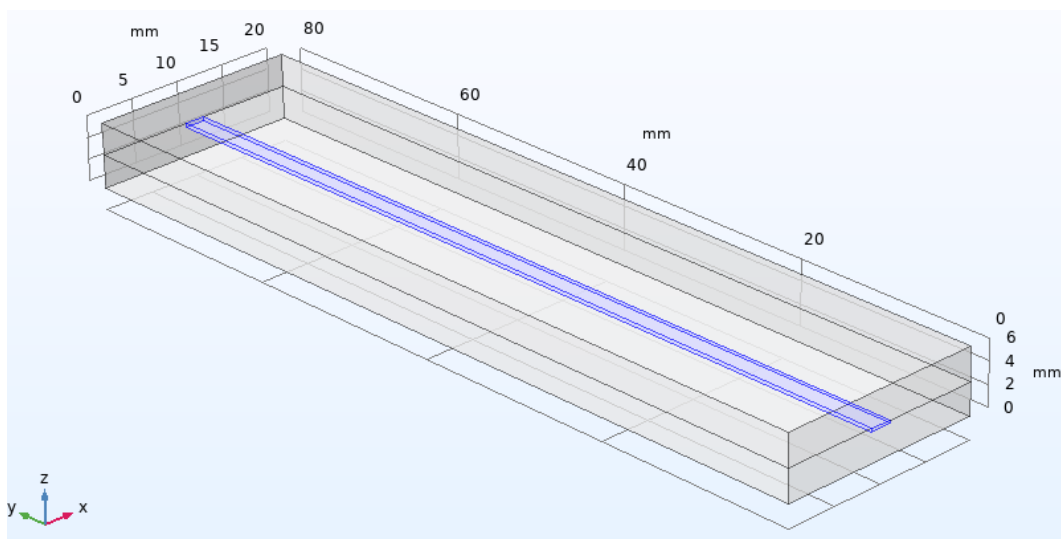


Figure 4.13: Schematic of the modeling in COMSOL Multiphysics.

Three different physics have been employed, first one was “electric current”, which refers to the modeling and simulation of the flow of charged particles, typically electrons, through a conductor. This process generates an electric field and can induce other physical phenomena such as magnetic fields, heat, and mechanical forces. The equation for electric current can be described by the continuity equation:

$$\nabla \cdot J + \frac{\partial \rho}{\partial t} = 0 \quad (4-1)$$

where J is the electric current density vector and ρ is the charge density.

The second physics used was “heat transfer in solids and fluids” to study the movement of thermal energy through a solid material due to temperature differences. This process can occur through three mechanisms: conduction, convection, and radiation. The equation for heat transfer in solids and fluids can be written as the heat transfer equation, which is a partial differential equation that describes the flow of heat through a material (conservation of energy):

$$\rho C_p \left(\frac{\partial T}{\partial t} \right) - \nabla \cdot (k \nabla T) = Q \quad (4-2)$$

Where ρ is the material density, C_p is the specific heat capacity of the material, T is the temperature, t is time, k is the thermal conductivity of the material, and Q is the heat source or sink term.

The third physics was “laminar flow” which is mainly used for modeling and simulation of fluid flow in which the fluid particles move in smooth layers or streams, without significant mixing or turbulence between them. The equation for laminar flow is the Navier-Stokes equation, which describes the motion of a fluid:

$$\rho^*(\partial v/\partial t) + \rho^*(v \cdot \nabla)v = -\nabla p + \mu \nabla^2 v + f \quad (4-3)$$

Where ρ is the fluid density, v is the fluid velocity vector, t is time, p is the fluid pressure, μ is the fluid dynamic viscosity, ∇ is the gradient operator and f is any external forces acting on the fluid.

To simulate the model, different mesh sizes of free tetrahedral shapes were studied: normal, fine, and finer. The normal mesh had a maximum element size of 756 μm and a minimum element size of 226 μm , the fine mesh had a maximum element size of 559 μm and a minimum element size of 113 μm , and the finer mesh had a maximum element size of 418 μm and a minimum element size of 45.2 μm . The final results were consistent across all three mesh sizes despite the differences in size. However, it was observed that decreasing the mesh size led to an increase in computation time. Though, I would like to highlight that the results presented in this chapter were obtained using the normal size mesh.

Figure 4.14 shows the temperature profile exerted from simulation results along with the experimental results (Figure 4.12). Three different voltages have been simulated (3V, 4V, and 5V). This is a clear agreement between prediction and experiments behavior under both steady and transient condition.

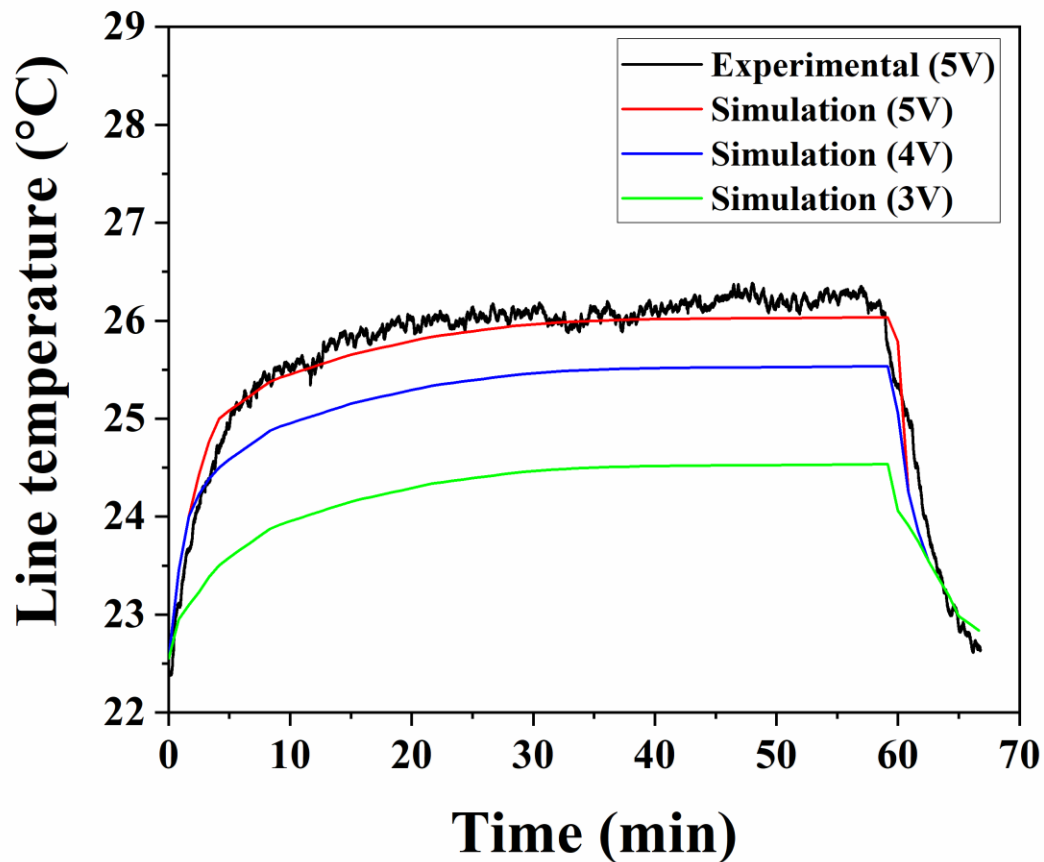


Figure 4.14: Experimental Vs Simulation of temperature change by applying voltage.

4.3. Conclusion and Future Research

In this chapter PEDOT:PSS has been used as the base polymer. According to the results, by using the PEDOT:PSS instead of the PDMS, resistivity, and conductivity have been influenced and reached $0.0026 \Omega\cdot\text{m}$ and 378.97 S/m , respectively, whilst Ozhikandathil et al. [13], reached resistivity of $0.0035 \Omega\cdot\text{m}$ which gives us conductivity equal to 285.7 S/m . PEG and Glycerol also add to the mixture to improve conductivity and flexibility and to have a better attachment to the

PDMS mold. Adding other nano-particles such as gold and silver is an interesting idea due to their potential electrical property and could be investigated in the future.

SEM images showed that the conducting route as a network structure forms by the long MWCNTs inside the PEDOT:PSS polymer and there is no agglomeration inside the polymer. According to the thermal characterization, the resistivity of the polymer is sensitive to the temperature and by increasing the temperature, resistivity will decrease. Also by applying an electrical voltage to the lines, the temperature of the lines increased by around 4 °C. Tests have been taken for three different line shapes: straight line, serpentine and zigzag and all of them showed the same pattern. Moreover, electro thermal simulation also shows a perfect match with experimental results.

Chapter 5. Routing for Energy Harvester

5.1. Introduction

The performance of modern wireless sensor networks and portable ultra low power electronic devices depends on an unbounded amount of battery life. To harvest energy from environmental sources and create a sustainable auxiliary power source, extensive research has been done as part of the effort [85, 86]. Energy harvesting is the process of gathering small amounts of energy from one or more nearby energy sources, storing them, and then using them when needed. Energy is all around us, and the energy transducer is the most crucial component in energy harvesting. Sustainable energy harvesting is crucial for a consistent supply of electricity to the electronics in addition to the harvester's output power.

Composing a hybrid type of harvester on a single device, which harvests energy from one or more ambient energy sources using a combination of different energy conversion mechanisms, is an efficient design strategy for increasing the harvesting energy. These mechanisms have included energy-transforming phenomena such as piezoelectric [87, 88], thermoelectric [89, 90], electrostatic [91], and triboelectric [92]. Piezoelectric materials can efficiently convert mechanical vibrational energy into electrical energy. Numerous studies have been done to create cheap and effective vibration-based energy harvesting devices using piezoelectric materials. Piezoceramics and piezopolymers are examples of representative piezoelectric materials.

Oh et al. [93] describe a versatile hybrid energy harvester for gathering energy from a single or multiple sources. Piezoelectric and thermoelectric conversions are combined to increase harvesting power. The piezoelectric component of the harvester uses frequency up-conversion to capture energy from low-frequency kinetic motion. Due to its flexibility, the thermoelectric component is appropriate for obtaining energy from a curved surface. The harvester enables sustainable energy

harvesting by capturing energy from two different energy sources (kinetic and thermal). The average power density produced by piezoelectric and thermoelectric conversion, respectively, was 28.57 and 0.64.

In research by Sodano et al. [94] for use in power harvesting devices, two different types of piezoelectric materials were experimentally examined. The two kinds are Macro Fiber Composites (MFC), which were recently developed at the NASA Langley Center, and the widely used monolithic piezoelectric (PZT). Their experimental findings determine the viability of using these devices in practical applications and estimate the devices' efficacy. The power generated by a piezoelectric device's vibration is typically in the range of a few milliwatts, which is far insufficient for the majority of applications.

Montero et al. [95] presented a straightforward printing-based fabrication method for a flexible piezoelectric energy-harvesting module with a built-in and improved full-wave diode bridge rectifier. They look into how the electrode configuration affects and how well piezoelectric elements harvest energy. According to the findings, the metal–insulator–metal (MIM) based energy harvester ($7.8 \mu\text{W}/\text{cm}^3$) can produce an output power density that is higher than the interdigitated electrode (IDE) based harvester ($20.8 \text{ nW}/\text{cm}^3$).

Ghosh et al. [96] introduced a method in which, one-dimensional aligned poly hybrid electroactive soft nanowires are used as a compatible overlay electrode with a biomimetic all-organic stretchable energy harvester which had PEDOT:PSS added to it. The harvester can function as an epidermal sensor that simultaneously detects and distinguishes both small pressure and thermal deviations exposed to an epidermis surface because of its excellent mechanical sensitivity ($\sim 100 \text{ mV}/\text{N}$), quick response time ($\sim 1 \text{ ms}$), outstanding mechanical and thermal stability, and good temperature resolution.

In this chapter, commercial energy harvesters are used in conjunction with PEDOT:PSS conductive composite to compare the energy loss.

5.2. Methodology

5.2.1. Materials

MWCNT (multiwall carbon nanotube) has been mixed with PEDOT:PSS. PDMS was prepared using a SYLGARD 184 Silicone Elastomer Kit (Dow Inc., USA) as the substrate. isopropyl alcohol (IPA) was added as the solvent. glycerol and Polyethylene glycol (PEG) were also added to the mixture to increase flexibility.

5.2.2. PDMS molds

A PDMS mold was prepared by mixing the base elastomer and curing agent at 10:1, which was then placed in a desiccator hooked up to a Wob-l Dry Pump 2562B-01 (Welch, USA) to remove air bubbles within the mixture. The PDMS mixture was poured into a mold and placed in a furnace at 60 °C (Fisher Scientific) for 3 hours to cure.

5.2.3. CNT-PEDOT:PSS Composites

In a glove box, CNT was added to a solution of IPA at 100:1, then ultrasonicated for 10 minutes using a VCX 500 ultrasonic processor (Sonics & Materials, Inc., USA). To this mixture, PEDOT:PSS was added at 1:2 by volume and ultrasonicated (750W, 40% power, pulses: 10 seconds on, 15 seconds off) for 2 minutes. 0.4 mL glycerol and 0.2 mL PEG were added to the PEDOT:PSS.

The mixture was poured into the PDMS mold and copper electrodes were placed so the tips were in contact with the mixture. The mixture was cured for 30 minutes at 70 °C.

5.3. Experimental set-up

A Lead-Zirconium-Titanate S118-J1SS-1808YB Piezoelectric Bending Transducer (Mide Technology, USA) was used to absorb mechanical energy and convert it to electricity (see Figure 5.1). The transducer was mounted to a Ling V203 Permanent Magnet Shaker (Ling Dynamic Systems Ltd., UK), and an Agilent 33220A 20 MHz Function/Arbitrary Waveform Generator (Agilent Technologies, Inc, USA) supplied the input voltage (V_{SUPPLY}). Voltages ranging from 1 V to 10 V at frequencies ranging from 10 to 150 Hz were used as inputs to the shaker to measure the resonant frequency of the transducer.

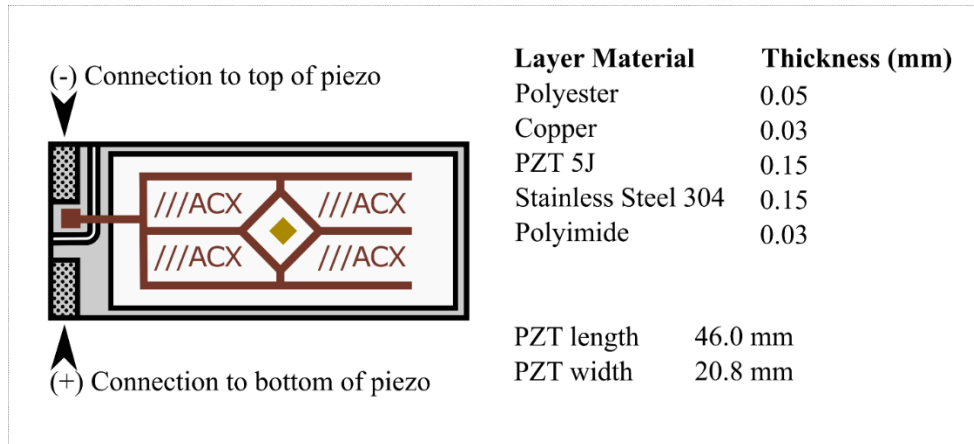


Figure 5.1: Lead-Zirconium-Titanate piezoelectric transducer

Figure 5.2 shows the schematic circuit of the setup. V_{PZT} is the voltage supplied by the piezoelectric actuator, C_1 is the 10 μ F smoothing capacitor, D_1 is a 1N4001 diode and R_2 is a 30k Ω resistor used for smoothing the voltage. The output voltage from the piezoelectric transducer was converted from AC to DC through a 2KBP02M, 200V 2A Single Phase Diode Bridge Rectifier.

The rectified voltage was smoothed using C_1 , and R_1 was added to the circuit to test the effect of PEDOT:PSS charging a 3.6V Li-ion rechargeable 2032 cell battery.

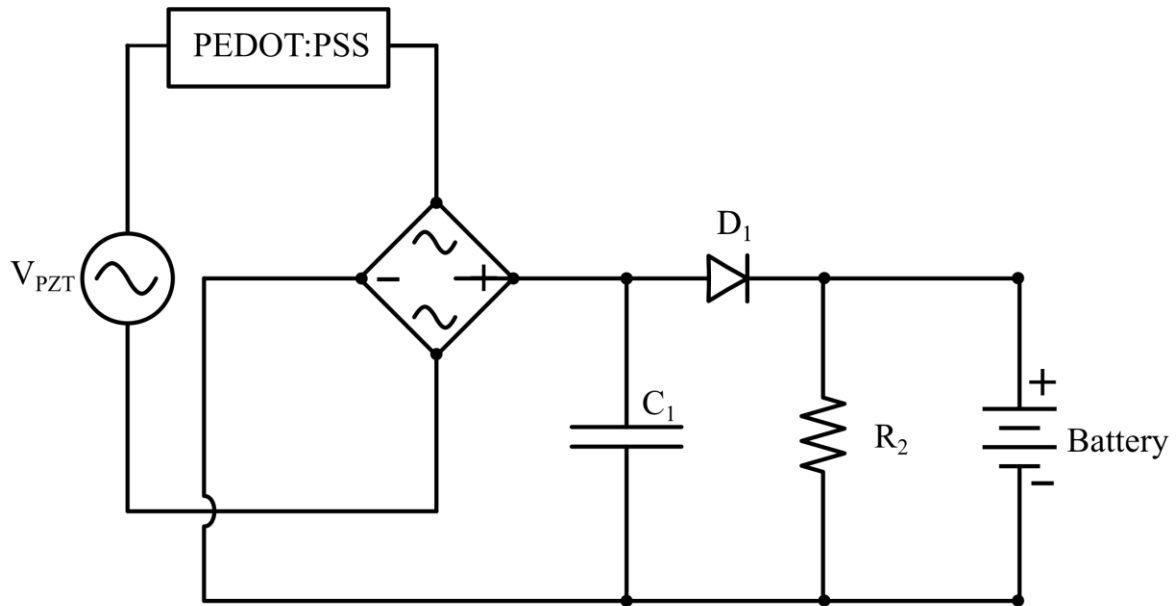


Figure 5.2: Equivalent circuit of energy harvesting set up from piezoelectric transducer

Figure 5.3 and Figure 5.4 show the schematic setup for this experiment. Figure 5.5 depicts a Diagram of a piezoelectric actuator in a cantilever beam set-up and Figure 5.6 demonstrates the Waveform of voltage from a piezoelectric actuator and a full-bridge rectifier and the smoothing action of a reservoir capacitor.

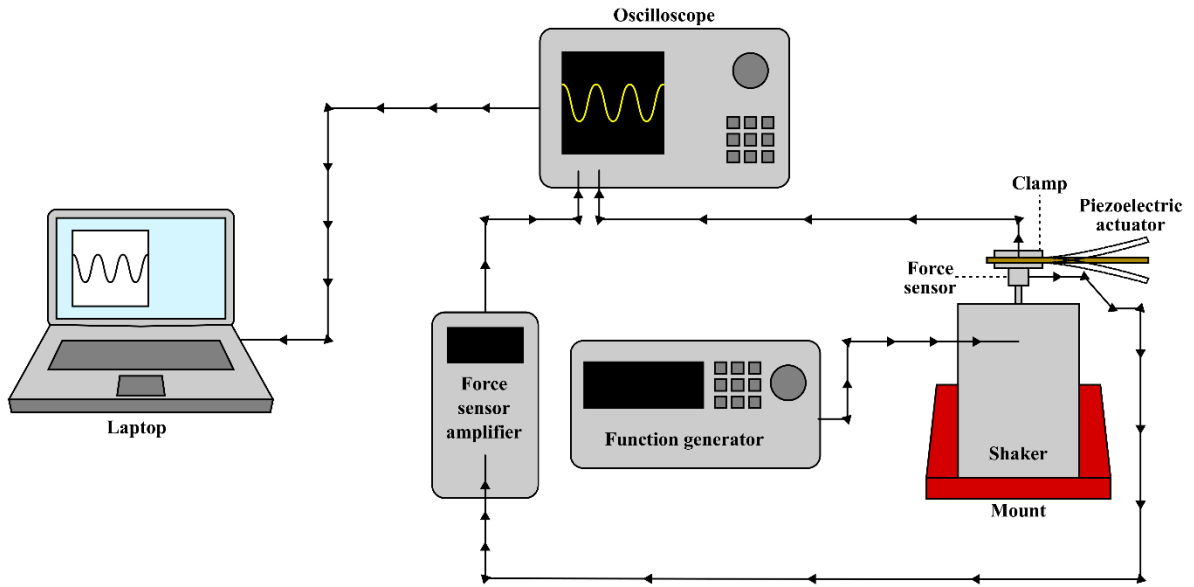


Figure 5.3: Schematic set-up for measuring force and voltage.

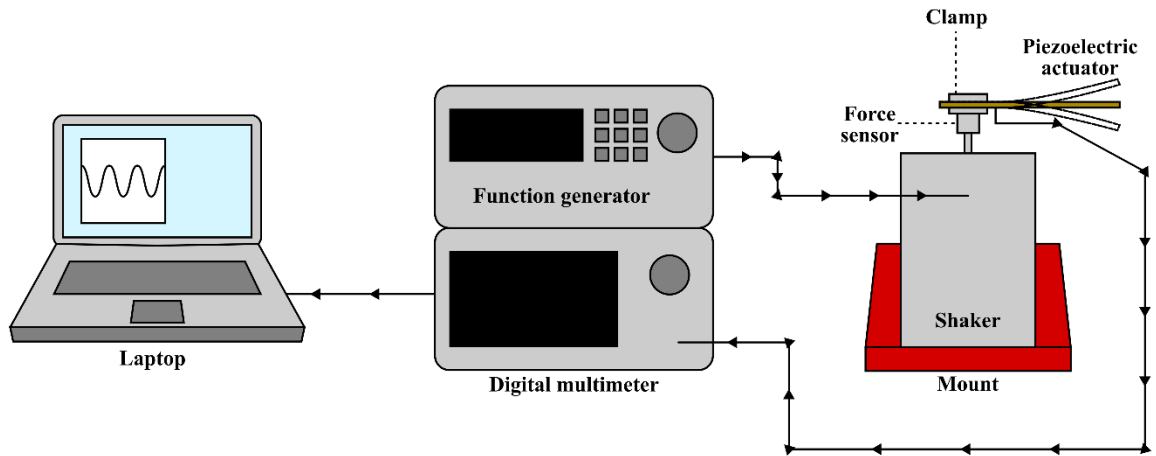


Figure 5.4: Schematic set-up for measuring current and voltage.

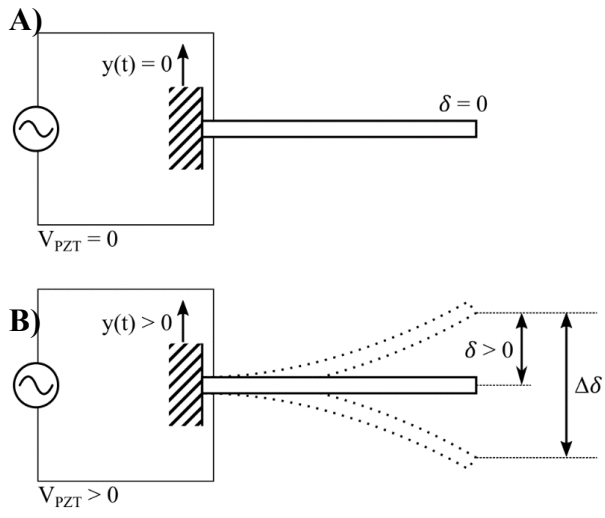


Figure 5.5: Diagram of a piezoelectric actuator in cantilever beam set-up. Actuator is A) at rest and B) in motion and producing an AC voltage

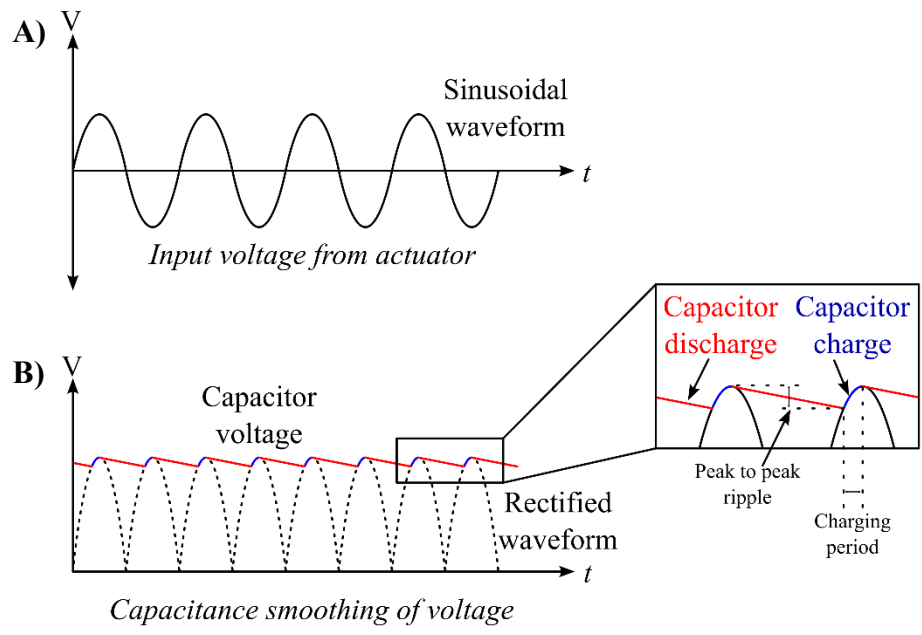


Figure 5.6: Waveform of voltage from A) a piezoelectric actuator and B) a full-bridge rectifier and smoothing action of a reservoir capacitor

5.4. Electrical measurements

A Tektronix DPO2024B Digital Phosphor Oscilloscope (Tektronix Inc., USA) was used to measure the voltage at different points in the circuit. The oscilloscope was connected to a computer using TekVISA v4.1.1, and the voltage waveform was recorded using Tektronix OpenChoice Desktop v2.6.

Further electrical measurements were taken using a Keysight B2902A Precision Source Measurement Unit (Keysight, USA), which was connected to a computer and controlled using Quick I/V Measurement Software v4.2.2045.2760 (Keysight, USA)

A 9712b50 force sensor (Kistler, Switzerland) connected to a Type 5010B charge amplifier (Kistler, Switzerland) was used to measure the force imparted by the shaker onto the piezoelectric actuator. The scale was set to 2 lbf/V, or 8.9 N/V.

5.4.1. Cascading Efficiency

Efficiency was calculated using the following equation (5.1), where η is the efficiency, P_{in} is the input power supplied (see Figure 5.7), calculated from the measured voltage and current; $P=IV$, and P_{out} is the output power provided by individual stages. It should be noted that the input and output powers of each cascaded block are interlinked via series of components. The components performance regarding any stray capacitance and internal resistance are encountered as lumped parameter by this modeling. The power produced by the piezoelectric actuator (P_{PZT}) was measured, consecutively the power flow in PEDOT:PSS component ($P_{P.P}$), the rectifier (P_{RC}) and the RC network (P_{out}) are measured.

$$\eta = \frac{P_{out}}{P_{in}} \quad (5.1)$$

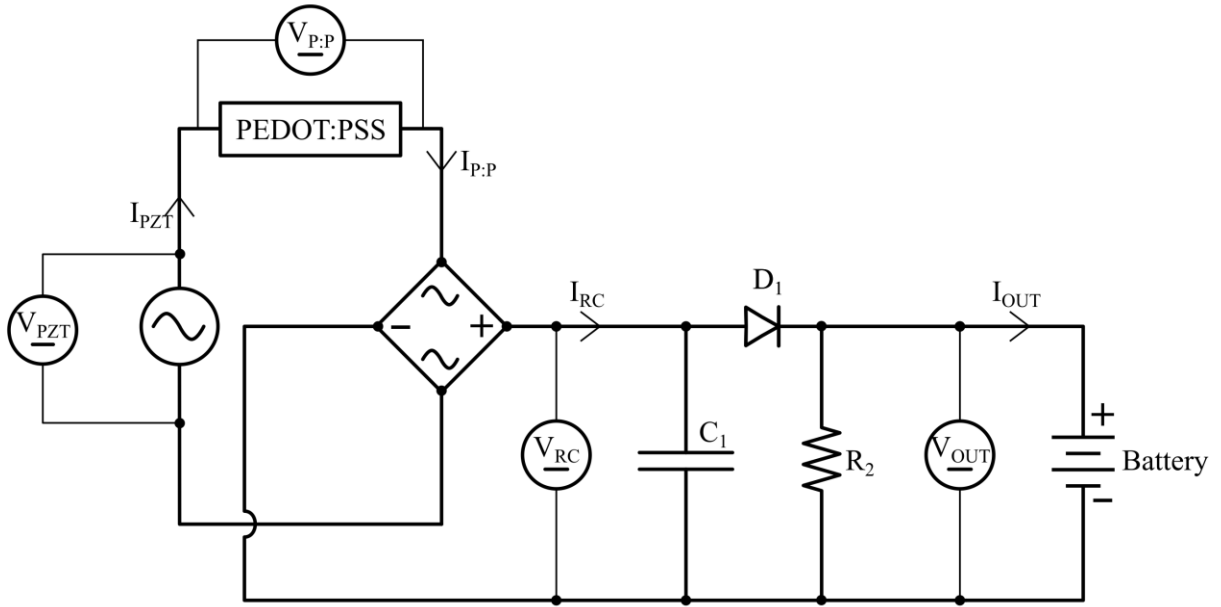


Figure 5.7: Schematic circuit showing where power between components was measured.

The cascading efficiency of the circuit (η_T) is the product of all the efficiencies for the various components (see Figure 5.8), calculated using equation(5.2).

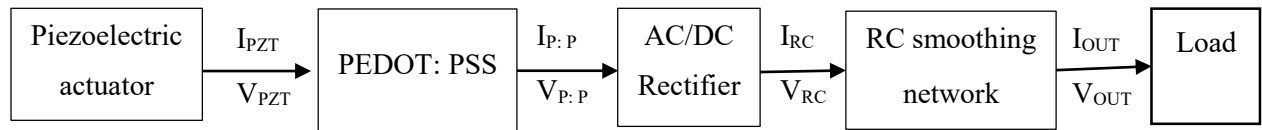


Figure 5.8: Measured electrical parameters between components.

Where $I_{P:ZT}$, $I_{P:P}$, I_{RC} and I_{OUT} are current from piezoelectric, PEDOT:PSS, rectifier and RC network, respectively and $V_{P:ZT}$, $V_{P:P}$, V_{RC} and V_{OUT} are voltage across piezoelectric, PEDOT:PSS, Rectifier and RC network respectively. The V_{OUT} is the readily available DC voltage for load connections. The power can now be calculated using $P = IV$ for each component (i.e. $P_{P:ZT}$, $P_{P:P}$, P_{RC} and P_{OUT}). Using equation (5.1), efficiency at each cascaded component can be calculated using equation (5.2)

to equation (5.4) (i.e, $\eta_{P:P}$, η_{RC} , η_{out}). The total efficiency (η_T) obtained by cascaded multiplying the efficiency of all component as show in equation (5.5).

$$\eta_{P:P} = \frac{P_{P:P}}{P_{PZT}} = \frac{V_{P:P} \times I_{P:P}}{V_{PZT} \times I_{PZT}} \quad (5.2)$$

$$\eta_{RC} = \frac{P_{RC}}{P_{P:P}} = \frac{V_{RC} \times I_{RC}}{V_{P:P} \times I_{P:P}} \quad (5.3)$$

$$\eta_{OUT} = \frac{P_{OUT}}{P_{RC}} = \frac{V_{OUT} \times I_{OUT}}{V_{RC} \times I_{RC}} \quad (5.4)$$

$$\eta_T = \eta_{P:P} \times \eta_{RC} \times \eta_{out} \quad (5.5)$$

Where, $\eta_{P:P}$ is defined the power transfer capabilities of PEDT:PSS. The encounter of the PEDOT:PSS's stray capacitance is lumped in this efficiency calculation via their output performances (voltage and current). η_{RC} is the performance metric of the rectifier circuit. The drop in the diode terminals during their forward conduction and the diode's internal thermal coefficients are lumped by their power metrics. At this stage, the ac input from the transducer is rectified to a pulsed DC signal. For the simplicity of the calculations and analysis, only RMS power is considered in the calculations. η_{OUT} determines the smoothing performance of the RC network. Here a smoothing capacitor converts the pulsed DC signal to low ripple pure DC values. The value of the capacitor is selected using the τ (RC times constant), guaranteeing the minimum ripple in the output at the transducer's resonance frequency.

As this cascaded efficiency calculation approach encounters all the necessary electrical performance metrics, it is suitable to evaluate the performance of this PEDOT: PSS in an eclectic charger, charging a simple commercially available Li-Ion battery. In this work, the performance

of the electric charging is modelled and analyzed using the lumped parameter. Detailed modelling work on individual blocks is avoided for a simpler approach.

5.5. Results and Discussion

The resonant frequency (f_{RES}) was determined experimentally by applying 10V to the shaker from 60 to 190 Hz. Figure 5.9 shows the peak to peak voltage at each frequency, and results indicate that f_{RES} can be found to be 135 Hz.

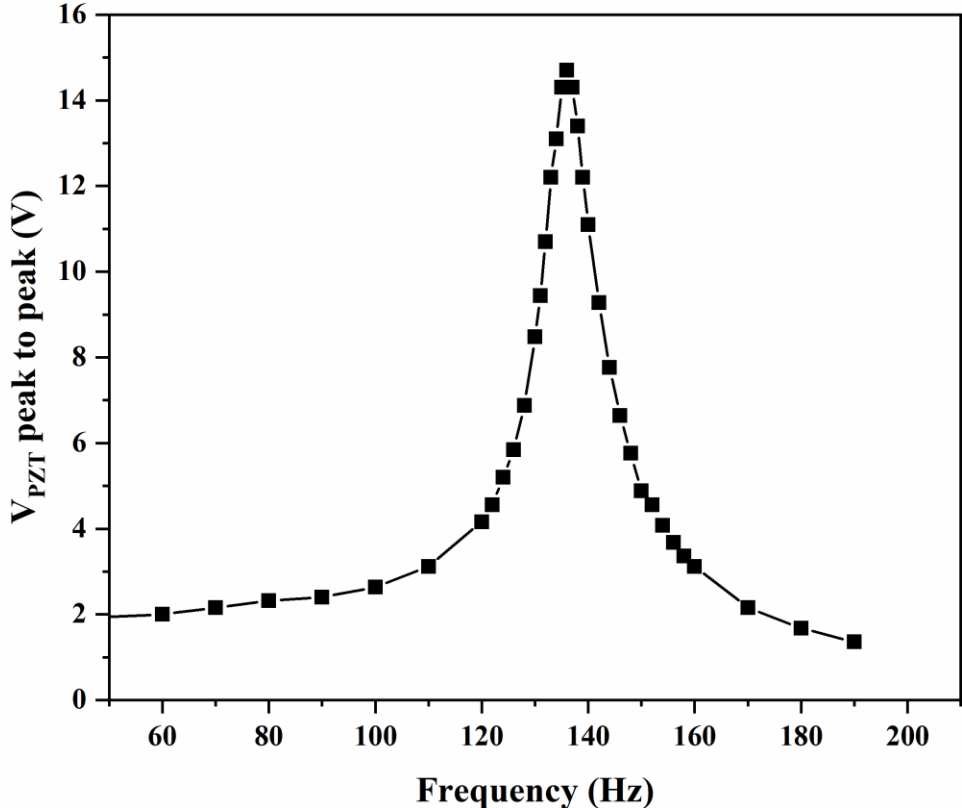


Figure 5.9: Peak to peak voltage of piezoelectric transducer, from 60 to 190 Hz

Applying a potential at 135 Hz through the shaker will thus produce the maximum voltage from the piezoelectric transducer.

A “flick test” was conducted where the piezoelectric actuator was physically flicked, and the peak to peak voltage produced was recorded. Figure 5.10 shows V_{PZT} , a typical dampened waveform pattern with a period, T , of 0.0073s. taking $f = 1/T$, the resonant frequency is 136 Hz.

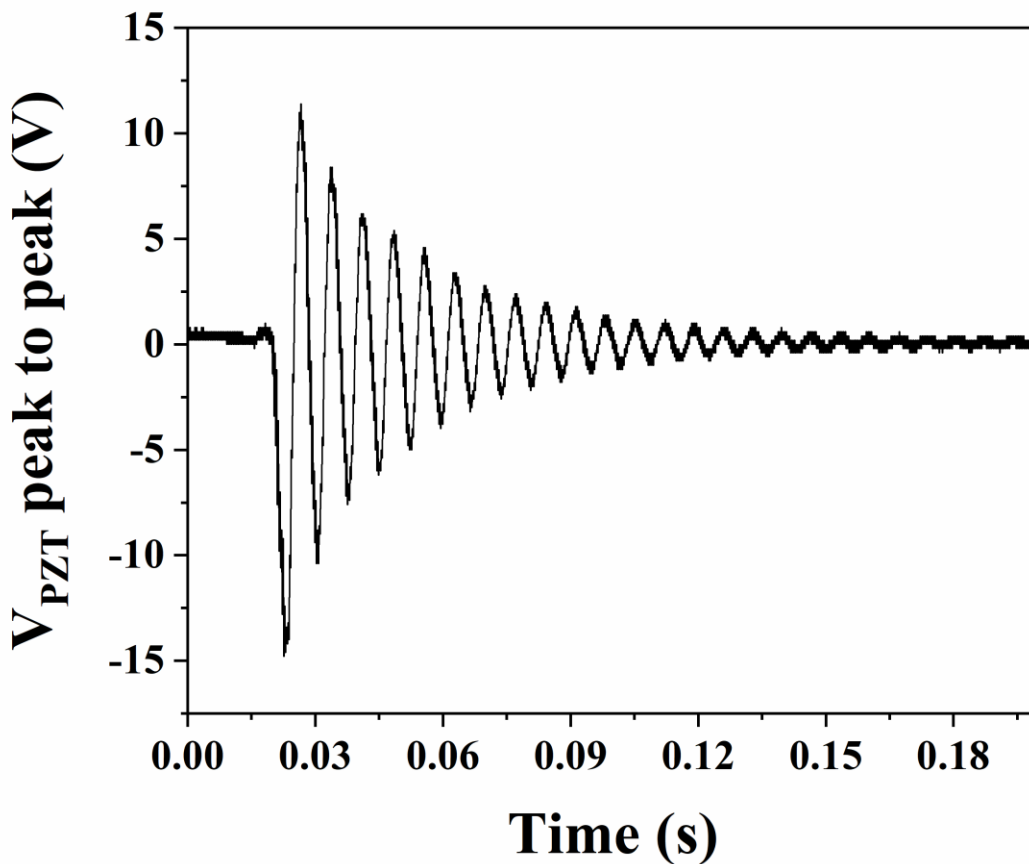


Figure 5.10: Peak to peak voltage produced from piezoelectric actuator during “flick test”

Figure 5.11 shows the effect of using PEDOT:PSS in the circuit on passing the voltage. PZT is when there was not any extra resistance in the circuit (i.e. PEDOT:PSS) and in that case the voltage

went up to 2.3V. while adding PEDOT:PSS will result in a voltage reduction to 1.7V. The maximum voltage has been measured after the capacitor.

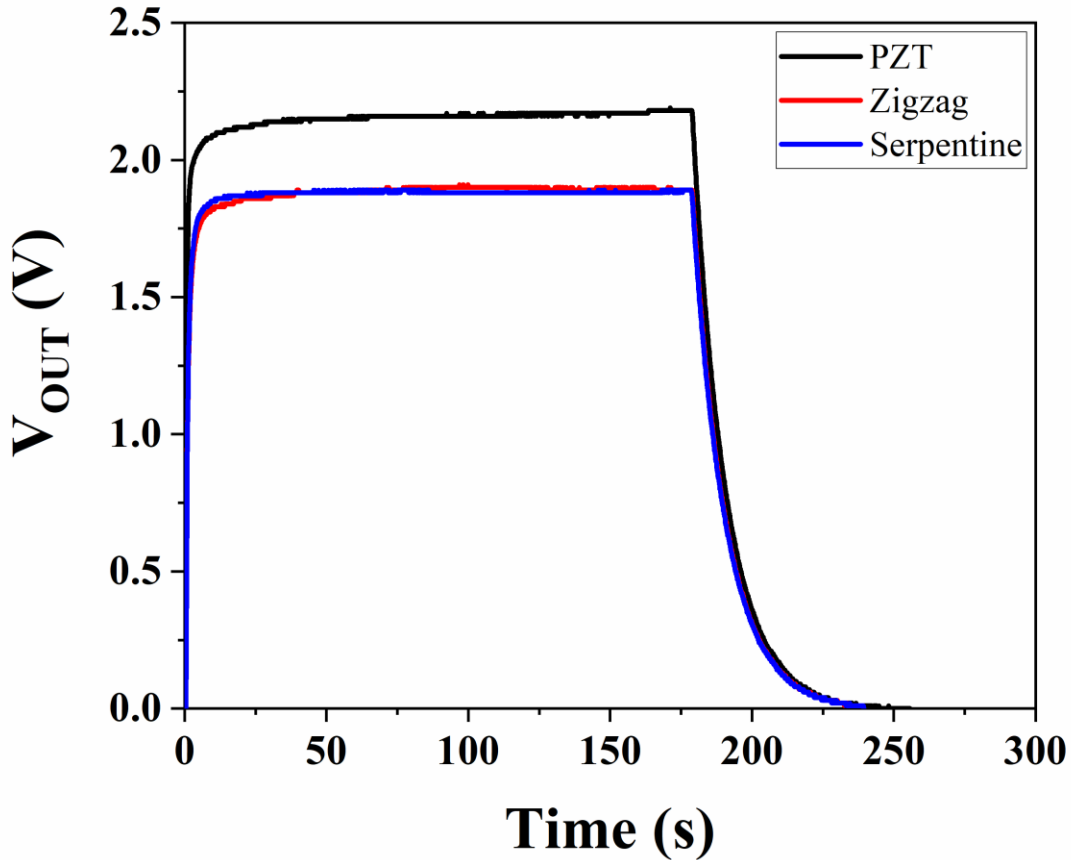
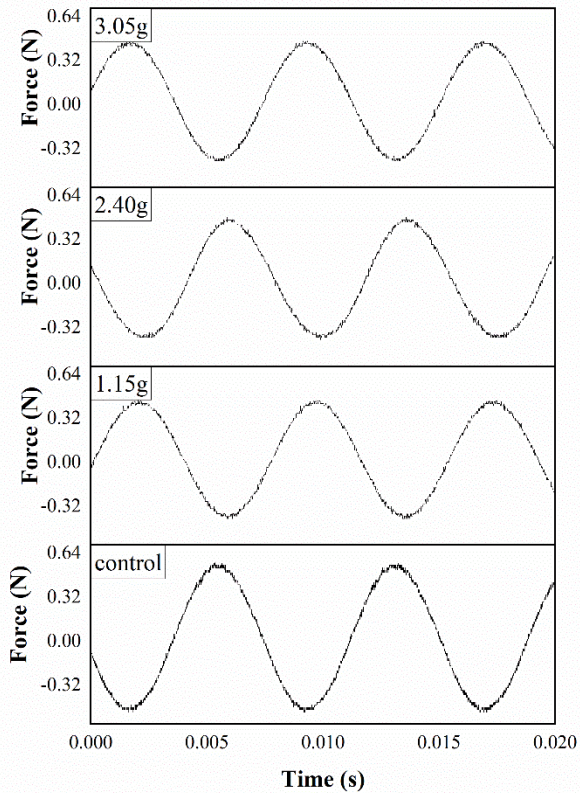


Figure 5.11: Maximum voltage after smoothing recorded from piezoelectric transducer and from PEDOT:PSS components.

In other tests, small weights were added to the tip of the piezo-electric energy harvester to see the effect of the output voltage as well as force. A load of 1.15 g, 2.40 g, and 3.05 g were added respectively.

A)



B)

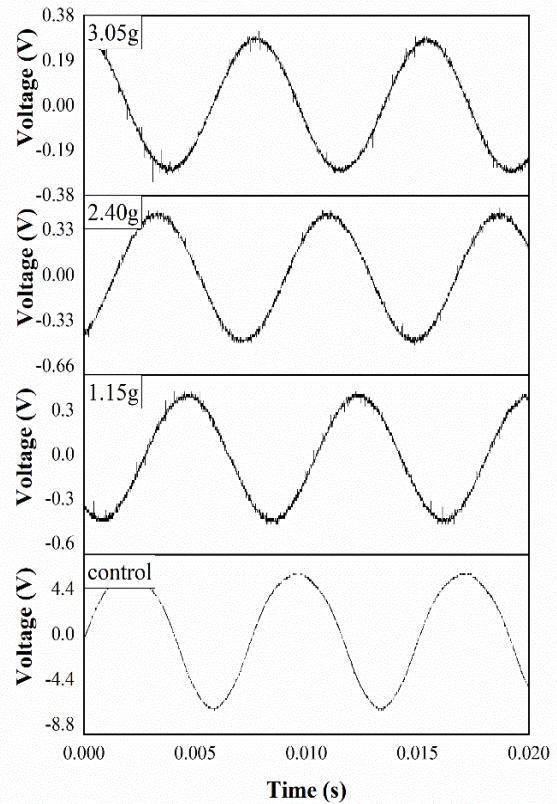


Figure 5.12: A) Force and B) voltage before and after adding weight of 1.15, 2.40 and 3.05 g.

Table 5.1: Maximum recorded force and voltage after weight added to piezoelectric actuator

	0 g	1.15 g	2.40 g	3.05 g
Force (N)	0.57	0.48	0.46	0.46
Voltage, V_{PZT} (V)	6.00	0.49	0.45	0.32

According to the results (see Table 5.1), the force imparted on the actuator drops pretty low from 0.57N to 0.48N when a load is added to the cantilever (The scale was set to 2 lbf/V or 8.9 N/V, i.e. the voltage showed by force sensor multiplied by 8.9 to get force on Newton (N)), but the

voltage decreases to around 300 mV from 6 V, showing that adding weight to the piezoelectric actuator will cause a decrease in voltage by 95% (see Figure 5.13). Table 5.1 shows the maximum force and voltage after adding a load to the tip of the energy harvester.

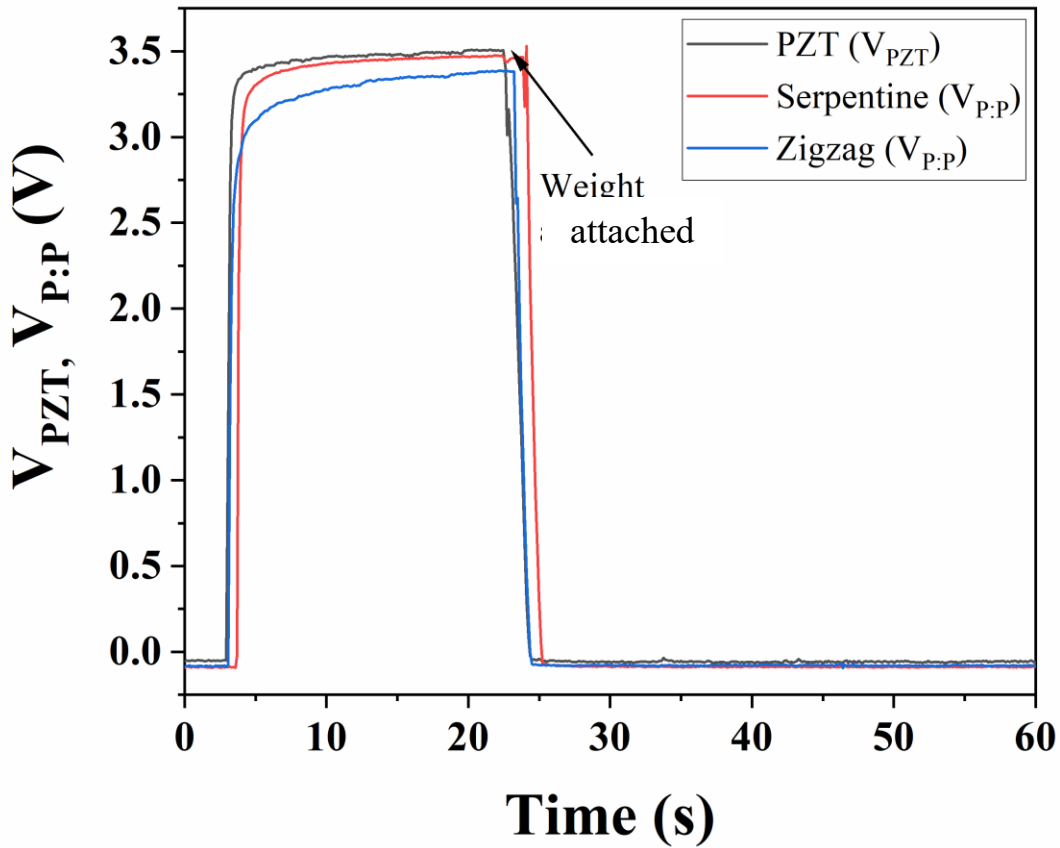


Figure 5.13: Voltage before and after adding a 1.15 g load, recorded from the piezoelectric transducer and from PEDOT:PSS components.

The efficiency, η , was calculated by recording the current and voltage at different junctions within the circuit, and calculating the power (see Figure 5.7). Efficiency was calculated in three different

circuits, with and without PEDOT:PSS components to see the effect of implementing conductive PEDOT:PSS in charging the battery (load).

Table 5.2 shows the measured rms voltage and current, and calculated power. Table 5.3 and Table 5.4 are showing measured rms voltage and current, and calculated power when PEDOT:PSS components have been inserted into the circuit.

Table 5.5 shows the cascading efficiency after each component. In all cases, the circuit loses about 50% of its power in the bridge rectifier, and another 50% in the RC time constant. The performances can be improved by incorporating low power diodes in bridge rectifier circuit besides the commercial available diodes used in the experiments. Based on the result, using PEDOT:PSS in the circuit does not have a significant effect on efficiency.

Table 5.2: Measure RMS voltage and current after components, without any PEDOT:PSS component.

	RMS Voltage (V)	RMS Current (A)	Power (W)
PZT	5.94, (V_{PZT})	5.44×10^{-4} , (I_{PZT})	3.23×10^{-3} , (P_{PZT})
Rectifier	5.52, (V_{RC})	2.78×10^{-4} , (I_{RC})	1.53×10^{-3} , (P_{RC})
RC network	3.89, (V_{OUT})	2.00×10^{-4} , (I_{OUT})	0.77×10^{-3} , (P_{OUT})

Table 5.3: Measure RMS voltage and current after components, with zigzag PEDOT:PSS component included.

	RMS Voltage (V)	RMS Current (A)	Power (W)
PZT	6.45, (V_{PZT})	5.44×10^{-4} , (I_{PZT})	3.51×10^{-3} , (P_{PZT})
PEDOT:PSS	6.35, ($V_{P:P}$)	5.10×10^{-4} , ($I_{P:P}$)	3.24×10^{-3} , ($P_{P:P}$)
Rectifier	5.86, (V_{RC})	2.77×10^{-4} , (I_{RC})	1.62×10^{-3} , (P_{RC})
RC network	4.12, (V_{OUT})	1.99×10^{-4} , (I_{OUT})	0.82×10^{-3} , (P_{OUT})

Table 5.4: Measure RMS voltage and current after components, with serpentine PEDOT:PSS component included.

	RMS Voltage (V)	RMS Current (A)	Power (W)
PZT	6.55, (V_{PZT})	5.66×10^{-4} , (I_{PZT})	3.71×10^{-3} , (P_{PZT})
PEDOT:PSS	6.53, ($V_{P:P}$)	5.44×10^{-4} , ($I_{P:P}$)	3.55×10^{-3} , ($P_{P:P}$)
Rectifier	5.91, (V_{RC})	2.77×10^{-4} , (I_{RC})	1.64×10^{-3} , (P_{RC})
RC network	4.20, (V_{OUT})	1.99×10^{-4} , (I_{OUT})	0.84×10^{-3} , (P_{OUT})

Table 5.5: Cascading efficiency between components

	Efficiency of control	Efficiency with zigzag line	Efficiency with serpentine line
PZT to PEDOT:PSS, ($\eta_{P:P}$)	n/a (1)	0.92	0.95
PEDOT:PSS to rectifier, (η_{RC})	0.47	0.50	0.46
Rectifier to RC network, (η_{OUT})	0.50	0.50	0.51
Total efficiency, (η_T)	0.24	0.23	0.22

In the last step, a 3.6V Li-ion rechargeable 2032 cell battery, was tested to find out the effect of the PEDOT:PSS on charging. Figure 5.14 shows the charging rate of the battery with and without PEDOT:PSS. The experiment for each sample took 1 hour while the output voltage from the piezoelectric was 3.8V. As it is clear, the battery charged from 0 to 3V when the battery was connected directly to the circuit. By integrating the PEDOT:PSS to the circuit, the charging rate will be reduced. Two different samples with two different patterns (zigzag and serpentine) have been tested. The result shows the battery will be charged from 0 to 2V after 1 hour. This reduction in charging speed is due to integrating extra impedance (i.e. PEDOT:PSS) into the circuit.

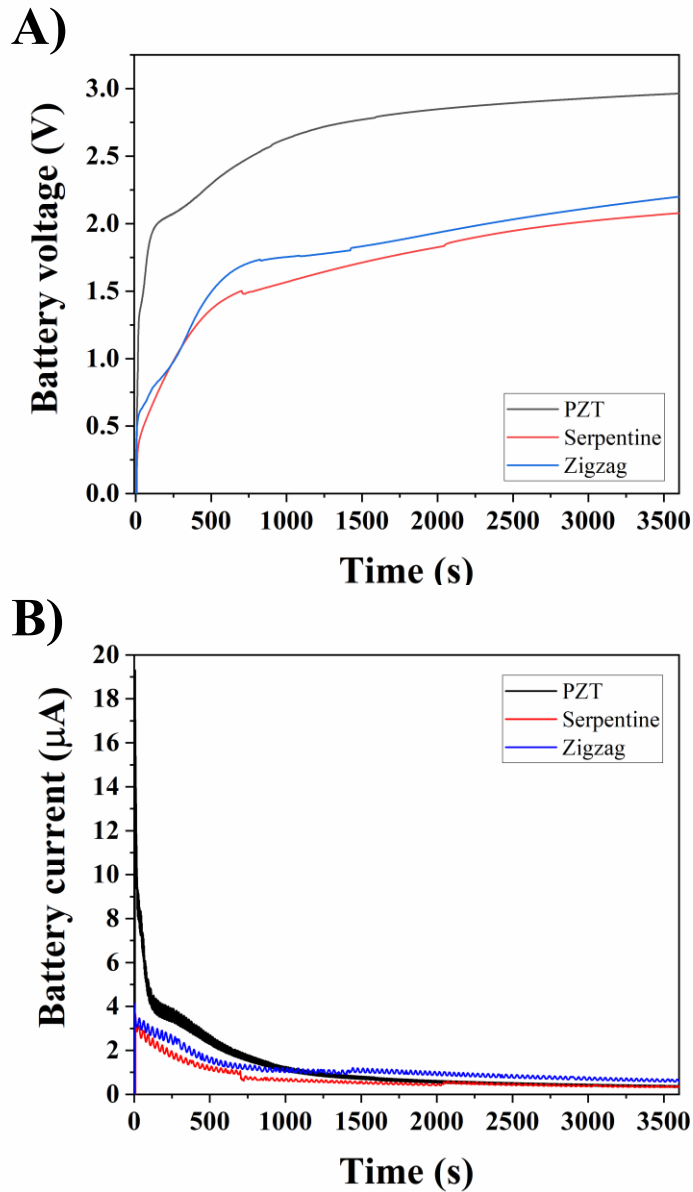


Figure 5.14: Real-time A) voltage and B) current recorded from the battery during charging from the piezoelectric transducer and from PEDOT:PSS components

5.6. Conclusion and Future Research

This chapter showed that it is possible to use a piezoelectric actuator to charge small components like a 3.6V Li-ion rechargeable 2032 cell battery. Integrating PEDOT:PSS composite routing into

charging a battery is feasible, however, it will reduce the charging by around 67% due to voltage drop from extra resistivity associated with polymer routing.

The efficiency test showed that using conductive PEDOT:PSS polymer in the circuit does not have a notable impact on total efficiency and it is a promising technology for future electrical routing research. Also, it is found that any weight added to the tip of piezo electric would prevent the charging as it massively decreases the voltage the actuator produces.

To the best of our knowledge, using a conductive polymer nano composite to charge the batteries was not given attention in the literature. As the next step and for future research, adding metal particles such as Gold could be an effective approach to increase the efficiency of the conductive polymer, however, it might reduce the flexibility of the sample which is another drawback.

Chapter 6. Conclusion and Future work

In this study, the fabrication of conductive lines using MWCNTs and PDMS was investigated. The effect of filler aspect ratio on conductivity was evaluated, and the best conductivity achieved was 94.33 S/m for CNT15 at 50 wt.%. However, adding other fillers such as silver and gold could further enhance the conductivity, and using a conductive polymer instead of an insulative polymer like PDMS could also be explored.

Comparing the results between ultra-sonication and shear mixing showed that the former method led to a continuous reduction in resistivity with increasing MWCNTs, while the latter resulted in an increase in resistivity above 35% MWCNTs due to filler aggregation. Additionally, the addition of AgNP to the CNT15/PDMS sample increased conductivity to 121.21 S/m, but the conductive paths were not effectively created due to the separation of smaller and larger silver nanoparticles.

PEDOT:PSS was used as the base polymer in another experiment, resulting in a resistivity of 0.0026 $\Omega\cdot\text{m}$ and conductivity of 378.97 S/m. PEG and glycerol were added to improve conductivity and flexibility. SEM images showed no agglomeration inside the polymer, and the conducting route formed a network structure by the long MWCNTs. Thermal characterization showed that resistivity decreased with increasing temperature, and the lines had a fast response to applied voltage, making them suitable for thermal sensing applications. Also, according to the modeling, there is a clear agreement between prediction and experiments behavior under both steady and transient condition.

Lastly, it was shown that a piezoelectric actuator could charge a 3.6V Li-ion rechargeable 2032 cell battery, but integrating the PEDOT:PSS composite routing reduced charging efficiency by around 67%. Conductive polymer nano composites have not been extensively studied in battery

charging, and adding metal particles such as gold could improve efficiency in future research, although it may reduce flexibility.

Overall, this study demonstrated several promising approaches for the development of conductive polymer composites for various applications such as electromagnetic shielding and electrical routing. Further investigation of different fillers, base polymers, and fabrication methods could lead to improved conductivity and efficiency.

References

1. Khosla, A. and B.L. Gray, *Micropatternable multifunctional nanocomposite polymers for flexible soft NEMS and MEMS applications*. ECS Transactions, 2012. **45**(3): p. 477.
2. Litic, D. and E. Popovici, *Guozhong CAO, Nanostructures and nanomaterials. Synthesis, properties and applications*. REVUE ROUMAINE DE CHIMIE, 2005. **50**(6): p. 497.
3. Feynman, R.P. *Plenty of Room at the Bottom*. in *APS annual meeting*. 1959.
4. Nieto, M., F. Lopéz, and F. Cruz, *Performance analysis of technology using the S curve model: the case of digital signal processing (DSP) technologies*. Technovation, 1998. **18**(6-7): p. 439-457.
5. Jordan, C.C., I. Kaiser, and V.C. Moore, *2013 nanotechnology patent literature review: Graphitic carbon-based nanotechnology and energy applications are on the rise*. Nanotech. L. & Bus., 2014. **11**: p. 111.
6. Perez, C., *Technological revolutions and financial capital*. 2003: Edward Elgar Publishing.
7. Gangopadhyay, R. and A. De, *Conducting polymer nanocomposites: a brief overview*. Chemistry of materials, 2000. **12**(3): p. 608-622.
8. Zaouk, R., B.Y. Park, and M.J. Madou, *Introduction to microfabrication techniques, in Microfluidic Techniques*. 2006, Springer. p. 5-15.
9. Al-Jumaili, A., et al., *Review on the antimicrobial properties of carbon nanostructures*. Materials, 2017. **10**(9): p. 1066.
10. Khosla, A. and B. Gray, *Preparation, characterization and micromolding of multi-walled carbon nanotube polydimethylsiloxane conducting nanocomposite polymer*. Materials Letters, 2009. **63**(13-14): p. 1203-1206.
11. Ueda, T., et al. *Flexible enclosure for fluidic sealing of microcomponents*. in *Microfluidics, BioMEMS, and Medical Microsystems VI*. 2008. International Society for Optics and Photonics.
12. Kim, J.H., et al., *Simple and cost-effective method of highly conductive and elastic carbon nanotube/polydimethylsiloxane composite for wearable electronics*. Scientific reports, 2018. **8**(1): p. 1-11.
13. Ozhikandathil, J., A. Khosla, and M. Packirisamy, *Electrically conducting PDMS nanocomposite using in situ reduction of gold nanostructures and mechanical stimulation of carbon nanotubes and silver nanoparticles*. ECS Journal of Solid State Science and Technology, 2015. **4**(10): p. S3048.
14. Cavas, L., et al., *Reinforcement effects of multiwall carbon nanotubes and graphene oxide on PDMS marine coatings*. Journal of Coatings Technology and Research, 2018. **15**(1): p. 105-120.
15. Misra, A., et al., *Synthesis and characterization of carbon nanotube-polymer multilayer structures*. ACS nano, 2011. **5**(10): p. 7713-7721.
16. Zhang, Y., et al., *Polymer-embedded carbon nanotube ribbons for stretchable conductors*. Advanced Materials, 2010. **22**(28): p. 3027-3031.
17. Ozhikandathil, J., S. Badilescu, and M. Packirisamy, *Plasmonic gold decorated MWCNT nanocomposite for localized plasmon resonance sensing*. Scientific reports, 2015. **5**: p. 13181.

18. Herren, B., et al., *Enhanced Electrical Conductivity of Carbon Nanotube-Based Elastomer Nanocomposites Prepared by Microwave Curing*. *Polymers*, 2019. **11**(7): p. 1212.
19. Wu, L., et al., *Screen-printed flexible temperature sensor based on FG/CNT/PDMS composite with constant TCR*. *Journal of Materials Science: Materials in Electronics*, 2019. **30**(10): p. 9593-9601.
20. Niu, X., et al., *Characterizing and patterning of PDMS-based conducting composites*. *Advanced Materials*, 2007. **19**(18): p. 2682-2686.
21. Sepúlveda, A., et al., *Full elastic constitutive relation of non-isotropic aligned-CNT/PDMS flexible nanocomposites*. *Nanoscale*, 2013. **5**(11): p. 4847-4854.
22. Wu, C.-L., et al., *Static and dynamic mechanical properties of polydimethylsiloxane/carbon nanotube nanocomposites*. *Thin Solid Films*, 2009. **517**(17): p. 4895-4901.
23. Wang, Y., et al., *Layer-by-layer assembly of PDMS-coated nickel ferrite/multiwalled carbon nanotubes/cotton fabrics for robust and durable electromagnetic interference shielding*. *Cellulose*, 2020. **27**(5): p. 2829-2845.
24. Hocheng, H., et al., *Study of novel electrical routing and integrated packaging on bio-compatible flexible substrates*. *Microsystem technologies*, 2010. **16**(3): p. 423-430.
25. Raju, D., et al., *LSPR detection of extracellular vesicles using a silver-PDMS nanocomposite platform suitable for sensor networks*. *Enterprise Information Systems*, 2020. **14**(4): p. 532-541.
26. Bali, C., et al., *Fully inkjet-printed flexible temperature sensors based on carbon and PEDOT: PSS*. *Materials Today: Proceedings*, 2016. **3**(3): p. 739-745.
27. Ozhikandathil, J., S. Badilescu, and M. Packirisamy, *Polymer composite optically integrated lab on chip for the detection of ammonia*. *Journal of The Electrochemical Society*, 2018. **165**(8): p. B3078.
28. Tsao, L.-C., et al. *Flexible Temperature Sensor Array Using Electro-Resistive Polymer Forhumanoid Artificial Skin*. in *TRANSDUCERS 2007-2007 International Solid-State Sensors, Actuators and Microsystems Conference*. 2007. IEEE.
29. Ramalingame, R., et al., *Highly sensitive capacitive pressure sensors for robotic applications based on carbon nanotubes and PDMS polymer nanocomposite*. *Journal of Sensors and Sensor Systems*, 2019. **8**(1): p. 87-94.
30. Lai, Y.-T., Y.-M. Chen, and Y.-J.J. Yang, *A novel CNT-PDMS-based tactile sensing array with resistivity retaining and recovering by using dielectrophoresis effect*. *Journal of microelectromechanical systems*, 2011. **21**(1): p. 217-223.
31. Friend, J. and L. Yeo, *Fabrication of microfluidic devices using polydimethylsiloxane*. *Biomicrofluidics*, 2010. **4**(2): p. 026502.
32. Schneider, F., et al., *Process and material properties of polydimethylsiloxane (PDMS) for Optical MEMS*. *Sensors and Actuators A: Physical*, 2009. **151**(2): p. 95-99.
33. Sun, K., et al., *Flexible polydimethylsiloxane/multi-walled carbon nanotubes membranous metacomposites with negative permittivity*. *Polymer*, 2017. **125**: p. 50-57.
34. Reich, S., C. Thomsen, and J. Maultzsch, *Carbon nanotubes: basic concepts and physical properties*. 2008: John Wiley & Sons.
35. Jouni, M., et al., *A representative and comprehensive review of the electrical and thermal properties of polymer composites with carbon nanotube and other nanoparticle fillers*. *Polymer International*, 2017. **66**(9): p. 1237-1251.

36. Liu, C., *Nanocomposite conductive elastomer: microfabrication processes and applications in soft-matter MEMS sensors*. MRS Online Proceedings Library (OPL), 2006. **947**.
37. Engel, J., et al. *Multi-walled carbon nanotube filled conductive elastomers: materials and application to micro transducers*. in *19th IEEE International Conference on Micro Electro Mechanical Systems*. 2006. IEEE.
38. Xu, B., et al., *Making negative Poisson's ratio microstructures by soft lithography*. *Advanced materials*, 1999. **11**(14): p. 1186-1189.
39. Bauhofer, W. and J.Z. Kovacs, *A review and analysis of electrical percolation in carbon nanotube polymer composites*. *Composites science and technology*, 2009. **69**(10): p. 1486-1498.
40. Iijima, S. and P. Ajayan, *Smallest carbon nanotube*. *Nature*, 1992. **358**: p. 23-23.
41. Feng, C., *Micromechanics Modeling of the Electrical Conductivity of Carbon Nanotube (CNT)-Polymer Nanocomposites*. 2014.
42. Thostenson, E.T., Z. Ren, and T.-W. Chou, *Advances in the science and technology of carbon nanotubes and their composites: a review*. *Composites science and technology*, 2001. **61**(13): p. 1899-1912.
43. Hu, Y., et al., *Carbon nanostructures for advanced composites*. *Reports on Progress in Physics*, 2006. **69**(6): p. 1847.
44. Lin, Y., et al., *Advances toward bioapplications of carbon nanotubes*. *Journal of Materials Chemistry*, 2004. **14**(4): p. 527-541.
45. Chin, K.C., et al., *Gold and silver coated carbon nanotubes: an improved broad-band optical limiter*. *Chemical Physics Letters*, 2005. **409**(1-3): p. 85-88.
46. Wu, H., et al., *Properties investigation on isotropical conductive adhesives filled with silver coated carbon nanotubes*. *Composites science and technology*, 2007. **67**(6): p. 1182-1186.
47. Guo, D.J. and H.L. Li, *Highly dispersed Ag nanoparticles on functional MWNT surfaces for methanol oxidation in alkaline solution*. *Carbon*, 2005. **43**(6): p. 1259-1264.
48. Zhan, C., et al., *Conductive polymer nanocomposites: a critical review of modern advanced devices*. *Journal of Materials Chemistry C*, 2017. **5**(7): p. 1569-1585.
49. Liang, J., et al., *Silver nanowire percolation network soldered with graphene oxide at room temperature and its application for fully stretchable polymer light-emitting diodes*. *ACS nano*, 2014. **8**(2): p. 1590-1600.
50. Amjadi, M., et al., *Highly stretchable and sensitive strain sensor based on silver nanowire-elastomer nanocomposite*. *ACS nano*, 2014. **8**(5): p. 5154-5163.
51. Choi, J.-R., K.-Y. Rhee, and S.-J. Park, *Influence of electrolessly silver-plated multi-walled carbon nanotubes on thermal conductivity of epoxy matrix nanocomposites*. *Composites Part B: Engineering*, 2015. **80**: p. 379-384.
52. Xin, F. and L. Li, *Decoration of carbon nanotubes with silver nanoparticles for advanced CNT/polymer nanocomposites*. *Composites Part A: Applied Science and Manufacturing*, 2011. **42**(8): p. 961-967.
53. Ma, P.C., B.Z. Tang, and J.-K. Kim, *Effect of CNT decoration with silver nanoparticles on electrical conductivity of CNT-polymer composites*. *Carbon*, 2008. **46**(11): p. 1497-1505.
54. Wang, X., et al., *High electrical conductivity and carrier mobility in oCVD PEDOT thin films by engineered crystallization and acid treatment*. *Science Advances*, 2018. **4**(9): p. eaat5780.

55. Cho, B., et al., *Single-crystal poly (3, 4-ethylenedioxythiophene) nanowires with ultrahigh conductivity*. Nano letters, 2014. **14**(6): p. 3321-3327.
56. Gueye, M.N., et al., *Structure and dopant engineering in PEDOT thin films: Practical tools for a dramatic conductivity enhancement*. Chemistry of Materials, 2016. **28**(10): p. 3462-3468.
57. Chen, H.-W. and C. Li, *PEDOT: fundamentals and its nanocomposites for energy storage*. Chinese Journal of Polymer Science, 2020. **38**(5): p. 435-448.
58. Adekoya, G.J., R.E. Sadiku, and S.S. Ray, *Nanocomposites of PEDOT: PSS with graphene and its derivatives for flexible electronic applications: A review*. Macromolecular Materials and Engineering, 2021. **306**(3): p. 2000716.
59. Shi, H., et al., *Effective approaches to improve the electrical conductivity of PEDOT: PSS: a review*. Advanced Electronic Materials, 2015. **1**(4): p. 1500017.
60. Yue, R. and J. Xu, *Poly (3, 4-ethylenedioxythiophene) as promising organic thermoelectric materials: A mini-review*. Synthetic metals, 2012. **162**(11-12): p. 912-917.
61. Groenendaal, L., et al., *Poly (3, 4-ethylenedioxythiophene) and its derivatives: past, present, and future*. Advanced materials, 2000. **12**(7): p. 481-494.
62. Mannayil, J., et al., *Solution processable PEDOT: PSS/multiwalled carbon nanotube composite films for flexible electrode applications*. physica status solidi (a), 2018. **215**(18): p. 1701003.
63. Ouyang, J., et al., *On the mechanism of conductivity enhancement in poly (3, 4-ethylenedioxythiophene): poly (styrene sulfonate) film through solvent treatment*. Polymer, 2004. **45**(25): p. 8443-8450.
64. Kim, G.H., D.H. Hwang, and S.I. Woo, *Thermoelectric properties of nanocomposite thin films prepared with poly (3, 4-ethylenedioxythiophene) poly (styrenesulfonate) and graphene*. Physical Chemistry Chemical Physics, 2012. **14**(10): p. 3530-3536.
65. Kević, D.P., et al., *Preparation of PEDOT: PSS thin films doped with graphene and graphene quantum dots*. Synthetic metals, 2014. **198**: p. 150-154.
66. Yeo, J.-S., et al., *Significant vertical phase separation in solvent-vapor-annealed poly (3, 4-ethylenedioxythiophene): poly (styrene sulfonate) composite films leading to better conductivity and work function for high-performance indium tin oxide-free optoelectronics*. ACS applied materials & interfaces, 2012. **4**(5): p. 2551-2560.
67. Yoo, D., J. Kim, and J.H. Kim, *Direct synthesis of highly conductive poly (3, 4-ethylenedioxythiophene): poly (4-styrenesulfonate)(PEDOT: PSS)/graphene composites and their applications in energy harvesting systems*. Nano Research, 2014. **7**(5): p. 717-730.
68. Samal, M., et al., *Graphene quantum rings doped PEDOT: PSS based composite layer for efficient performance of optoelectronic devices*. The Journal of Physical Chemistry C, 2015. **119**(34): p. 19619-19627.
69. Wang, Q., M.-R. Ahmadian-Yazdi, and M. Eslamian, *Investigation of morphology and physical properties of modified PEDOT: PSS films made via in-situ grafting method*. Synthetic Metals, 2015. **209**: p. 521-527.
70. Zhao, Z., et al., *Improving the conductivity of PEDOT: PSS hole transport layer in polymer solar cells via copper (II) bromide salt doping*. ACS applied materials & interfaces, 2015. **7**(3): p. 1439-1448.

71. Zabihi, F. and M. Eslamian, *Characteristics of thin films fabricated by spray coating on rough and permeable paper substrates*. Journal of Coatings Technology and Research, 2015. **12**(3): p. 489-503.
72. Soltani-kordshuli, F., F. Zabihi, and M. Eslamian, *Graphene-doped PEDOT: PSS nanocomposite thin films fabricated by conventional and substrate vibration-assisted spray coating (SVASC)*. Engineering Science and Technology, an International Journal, 2016. **19**(3): p. 1216-1223.
73. Habibi, M., et al., *Controlled wetting/dewetting through substrate vibration-assisted spray coating (SVASC)*. Journal of Coatings Technology and Research, 2016. **13**(2): p. 211-225.
74. Su, Y., et al., *PEDOT: PSS-exfoliated graphene to improve the corrosion resistance of waterborne epoxy coating*. Int. J. Electrochem. Sci, 2019. **14**: p. 4595-4610.
75. Yang, W., et al., *Flexible conducting polymer/reduced graphene oxide films: synthesis, characterization, and electrochemical performance*. Nanoscale Research Letters, 2015. **10**(1): p. 1-7.
76. Huang, J., et al., *Influence of thermal treatment on the conductivity and morphology of PEDOT/PSS films*. Synthetic Metals, 2003. **139**(3): p. 569-572.
77. Friedel, B., et al., *Effects of layer thickness and annealing of PEDOT: PSS layers in organic photodetectors*. Macromolecules, 2009. **42**(17): p. 6741-6747.
78. Moujoud, A., et al., *On the mechanism of conductivity enhancement and work function control in PEDOT: PSS film through UV-light treatment*. physica status solidi (a), 2010. **207**(7): p. 1704-1707.
79. Ouyang, J. and Y. Yang, *Conducting polymer as transparent electric glue*. Advanced Materials, 2006. **18**(16): p. 2141-2144.
80. Thomas, J.P. and K.T. Leung, *Defect-minimized PEDOT: PSS/planar-Si solar cell with very high efficiency*. Advanced functional materials, 2014. **24**(31): p. 4978-4985.
81. Mahakul, P.C., et al., *Preparation and characterization of PEDOT: PSS/reduced graphene oxide-carbon nanotubes hybrid composites for transparent electrode applications*. Journal of materials science, 2017. **52**(10): p. 5696-5707.
82. Sun, D.M., et al., *A review of carbon nanotube-and graphene-based flexible thin-film transistors*. Small, 2013. **9**(8): p. 1188-1205.
83. Zhao, D., et al., *Highly flexible and conductive cellulose-mediated PEDOT: PSS/MWCNT composite films for supercapacitor electrodes*. ACS applied materials & interfaces, 2017. **9**(15): p. 13213-13222.
84. Hasan, M.N., et al., *Wearable thermoelectric generator with vertically aligned PEDOT: PSS and carbon nanotubes thermoelements for energy harvesting*. International Journal of Energy Research, 2022. **46**(11): p. 15824-15836.
85. Wang, X., et al., *Harvesting ambient vibration energy over a wide frequency range for self-powered electronics*. ACS nano, 2017. **11**(2): p. 1728-1735.
86. Zhou, S., et al., *Modeling and experimental verification of doubly nonlinear magnet-coupled piezoelectric energy harvesting from ambient vibration*. Smart Materials and Structures, 2015. **24**(5): p. 055008.
87. Wang, W., et al., *Optimum resistance analysis and experimental verification of nonlinear piezoelectric energy harvesting from human motions*. Energy, 2017. **118**: p. 221-230.
88. Sun, X., F. Wang, and J. Xu, *Nonlinear piezoelectric structure for ultralow-frequency band vibration energy harvesting with magnetic interaction*. International Journal of Precision Engineering and Manufacturing-Green Technology, 2019. **6**(4): p. 671-679.

89. Atalay, T., et al., *Evaluation of energy efficiency of thermoelectric generator with two-phase thermo-syphon heat pipes and nano-particle fluids*. International Journal of Precision Engineering and Manufacturing-Green Technology, 2018. **5**(1): p. 5-12.
90. Kirihara, K., et al., *Thermoelectric power generation using nonwoven fabric module impregnated with conducting polymer PEDOT: PSS*. Synthetic Metals, 2017. **225**: p. 41-48.
91. Wang, F. and O. Hansen, *Electrostatic energy harvesting device with out-of-the-plane gap closing scheme*. Sensors and Actuators A: Physical, 2014. **211**: p. 131-137.
92. Fan, F.-R., Z.-Q. Tian, and Z.L. Wang, *Flexible triboelectric generator*. Nano energy, 2012. **1**(2): p. 328-334.
93. Oh, Y., et al., *Flexible energy harvester with piezoelectric and thermoelectric hybrid mechanisms for sustainable harvesting*. International Journal of Precision Engineering and Manufacturing-Green Technology, 2019. **6**(4): p. 691-698.
94. Sodano, H.A., et al. *Use of piezoelectric energy harvesting devices for charging batteries*. in *Smart Structures and Materials 2003: Smart Sensor Technology and Measurement Systems*. 2003. SPIE.
95. Montero, K.L., M.-M. Laurila, and M. Mäntysalo, *Effect of Electrode Structure on the Performance of Fully Printed Piezoelectric Energy Harvesters*. IEEE Journal on Flexible Electronics, 2022. **1**(1): p. 24-31.
96. Ghosh, S.K., et al., *Temperature–pressure hybrid sensing all-organic stretchable energy harvester*. ACS Applied Electronic Materials, 2020. **3**(1): p. 248-259.

